Analysis Of Computational Modeling Techniques For Complete Rotorcraft Configurations

A Dissertation
Presented to
The Academic Faculty

by

David M. O'Brien, Jr.

In Partial Fulfillment
of the Requirements for the Degree
Doctor of Philosophy in the School of Aerospace Engineering

Georgia Institute of Technology
May 2006

Analysis Of Computational Modeling Techniques
For Complete Rotorcraft Configurations

Approved by:

Dr. Marilyn J. Smith, Advisor
School of Aerospace Engineering
Georgia Institute of Technology

Dr. J. V. R. Prasad
School of Aerospace Engineering
Georgia Institute of Technology

Dr. Lakshmi Sankar
School of Aerospace Engineering
Georgia Institute of Technology

Dr. Eric J. Nielsen
Computational Aerosciences Branch
NASA Langley Research Center

Dr. Stephen M. Ruffin
School of Aerospace Engineering
Georgia Institute of Technology

Date Approved: March 29, 2006

Dedicated to

my mother

for encouraging me to follow my dreams

and

my fiancée

for the joy she brings to my life.

ACKNOWLEDGEMENTS

I am especially grateful to Dr. Marilyn Smith for the countless hours of guidance and support she provided during my graduate career. She suggested this topic and offered invaluable wisdom and insight to help see it through to completion. To my thesis committee members, Dr. Lakshmi Sankar, Dr. Stephen Ruffin, Dr. JVR Prasad, and Dr. Eric Nielsen, I wish to express a sincere appreciation for numerous suggestions to improve this manuscript.

The Georgia Tech Rotorcraft Center of Excellence and the US Army provided the funding for this project. Computer resources were provided through the DoD High Performance Computing Modernization Program centers at the Naval Oceanographic Office (NAVO), US Army Engineer Research and Development Center (ERDC), and Maui High Performance Computing Center (MHPCC). Both funding and computer resources are gratefully acknowledged because without either one this research would not have been successful.

Due to the computational nature of this investigation, preexisting software programs were utilized in conjunction with this research. I wish to praise the developers of the FUN3D flow solver, VGrid & GridTool grid generation software, and DiRTlib & SUGGAR overset utilities for the exceptional programs they have developed. In particular, I would like to express my gratitude to Dr. Eric Nielsen, Mr. Mike Park, Mr. Dana Hammond, Dr. Bil Kleb, and Dr. Robert Biedron for their assistance running FUN3D and understanding the source code; Dr. Shahyar Pirzadeh for assistance learning to use VGrid effectively; and Dr. Ralph Noack for his aid integrating DiRTlib into FUN3D and learning to use SUGGAR.

I would like to thank the Office National d'Études et de Recherches Aérospatiales (ONERA), U. S. Army Aeroflightdynamics Directorate (AFDD), and Georgia Institute of Technology for the opportunity to participate in an international collaboration studying the Dauphin configuration. Eurocopter provided the Dauphin 365N model and ONERA the corresponding experimental data for which I am particularly grateful.

Many individuals have offered fruitful suggestions and insights over the course of this investigation which I gratefully acknowledge. Mr. Mark Potsdam and Mr. Thomas Renaud collaborated with me on the Dauphin investigation. Dr. Raymond Mineck provided the ROBIN experimental data and offered insight regarding the testing procedure. Dr. Albert Brand provided the detailed report of the Georgia Institute of Technology experimental data and his thesis was one of the primary sources referred to during this investigation. My fellow graduate students, Mr. Matt Laurita, Mr. Andrew Shelton, Ms. Jennifer Abras, and Mr. Jae-Doo Lee offered their insights into this effort and helped to make my time in the research lab more enjoyable. Mr. Kavanaugh Eldredge deserves a special thank you for helping me to create some of the computational grids after I started working full time.

Last, but certainly not least, I am thankful for my family and friends. They provided encouragement and support during the ups and downs of my graduate career. I'd especially like to thank my younger brother, Mr. Charles O'Brien, for always challenging me to try harder and my fiancée, Ms. Jill Brew, whose patience allowed me to complete this thesis.

TABLE OF CONTENTS

DEDICATION . . . . . **iii**

ACKNOWLEDGEMENTS . . . . . **iv**

LIST OF TABLES . . . . . **ix**

LIST OF FIGURES . . . . . **x**

LIST OF SYMBOLS AND ABBREVIATIONS . . . . . **xiv**

SUMMARY . . . . . **xvi**

I INTRODUCTION **1**

1.1 Background 1

1.2 Literature Review 3

1.2.1 Experimental Investigations 3

1.2.2 Potential Methods 6

1.2.3 Structured Euler/Navier-Stokes Methods 7

1.2.4 Unstructured Euler/Navier-Stokes Methods 9

1.2.5 Other Techniques 11

1.2.6 CFD / CSD Coupling 12

1.3 Research Objectives 13

II COMPUTATIONAL METHOD **15**

2.1 Overview 15

2.2 Flow Solver 16

2.3 Overset Grid Library 23

2.4 Overset Grid Assembly 25

2.5 Unstructured Grid Generator 27

2.6 Flow Visualization 28

III ROTOR MODELING **30**

3.1 Overview 30

3.2 Actuator Disk Model 31

3.2.1 Pressure Jump Boundary Condition Implementation 32

3.2.2 Source Implementation . . . 35
3.3 Actuator Blade Model . . . 39
3.4 Aerodynamic Loading Models . . . 40
3.4.1 User Specified Model . . . 41
3.4.2 Algebraic Models . . . 41
3.4.3 Blade Element Theory Model . . . 43
3.5 Overset Rotor Blades . . . 48
IV TEST CASES AND CFD MODELING . . . 51
4.1 Unstructured Modeling Process . . . 51
4.2 Theoretical Rotor . . . 54
4.3 Supersonic Ramp . . . 54
4.4 Georgia Institute of Technology (GIT) Model . . . 55
4.5 NASA Langley ROBIN Model . . . 58
4.6 ONERA Dauphin Model . . . 63
V METHOD VERIFICATION . . . 66
5.1 Flow Assumptions . . . 66
5.2 Flow Solver Verification . . . 66
5.2.1 GIT Configuration Without Rotor . . . 67
5.2.2 Robin Configuration Without Rotor . . . 69
5.3 Actuator Disk Verification . . . 71
5.3.1 Isolated Rotor In Hover . . . 73
5.3.2 Isolated Rotor In Forward Flight . . . 76
5.4 Simple Actuator Disk Loading Models . . . 78
5.4.1 GIT with a Uniform and Linear Disk Loading . . . 78
5.4.2 ROBIN with a Uniform and Linear Disk Loading . . . 84
5.5 Blade Element Loading Model . . . 87
5.5.1 GIT with a Blade Element Disk Loading . . . 87
5.6 Actuator Blade Model . . . 96
5.7 Overset Verification . . . 98
5.7.1 Static Overset . . . 98

5.7.2 Dynamic Overset 101

VI RESULTS 107

6.1 Dauphin Investigation 107

6.2 ROBIN Investigation 113

6.2.1 Steady-State Computations 115

6.2.2 Unsteady Computations 121

6.2.3 Model Comparison 125

VII CONCLUSIONS & RECOMMENDATIONS 141

7.1 Conclusions 141

7.2 Recommendations 142

REFERENCES 145

VITA 154

LIST OF TABLES

1 Coefficients for the Backwards Differentiation Formula 22
2 Boundary Condition Enforcement 35
3 Geometry for the GIT Configuration 57
4 ROBIN Body Shape Coefficients 62
5 ROBIN Pylon Shape Coefficients 62
6 Geometry for the ROBIN Configuration 63
7 ROBIN Test Data 64
8 ROBIN Reference Values 64
9 GIT Rotor Off Grid Information 68
10 ROBIN Control Angles 115
11 ROBIN Force & Moment Comparison 139
12 ROBIN Timing Comparison 140

LIST OF FIGURES

1 Vortex wake structure over a simple model in forward flight. 3

2 Aerodynamic interactions for a typical helicopter. Adapted from Sheridan and Smith [10] 4

3 Node based dual mesh with original triangular mesh. 17

4 Effect of the far field boundary condition on the wake solution of a hovering rotor. 24

5 Overset mesh example, depicting in, out, and fringe nodes. 26

6 Flux calculation comparison for a one-dimensional duct flow problem. . . . 33

7 Comparison of exact intersections versus a discretized approximation. . . . 36

8 Source elements on an actuator disk. 37

9 Non-physical vorticity contours generated in a plane normal to a coarse actuator disk source grid. 37

10 Source elements on the actuator blades. 40

11 Blade loading with the uniform pressure distribution. 41

12 Blade loading with the linearly varying pressure distribution. 42

13 Velocity orientation in the blade element model. 45

14 Algebraic force coefficient example for the blade element model. 47

15 The five overset grids for modeling the ROBIN configuration. 49

16 GridTool source distribution for a baseline configuration. 52

17 GridTool source distribution for general rotor wake refinement. 53

18 GridTool source distribution for precise rotor wake refinement. 53

19 Geometry for the supersonic ramp test case. 55

20 CFD model of the GIT configuration with an actuator disk. 56

21 GIT hub comparison: Simplified vs. Approximate. 58

22 ROBIN experimental setup. From Reference [9]. 59

23 ROBIN experimental setup. From Reference [31]. 60

24 Dauphin experimental setup. From Reference [111]. 65

25 GIT rotor off centerline C_p distribution. 69

26 ROBIN surface C_p comparison for the isolated fuselage, experiment, and fuselage with strut. 70

27 ROBIN cross-section C_p in the vicinity of the strut. 72
28 Vorticity contours for a uniform source disk on a coarse grid. 74
29 Vorticity contours for a uniform source disk in hover on a fine grid. 75
30 Induced velocity through the centerline of the actuator disk in near hover conditions. 76
31 Velocity contours for a uniform source disk in hover on a fine grid. 77
32 Vorticity contours for a uniform source disk in forward flight on a fine grid. 79
33 Normal velocity contours for a uniform source disk in forward flight on a fine grid. 80
34 C_p distribution for the GIT configuration with a pressure jump actuator disk. 81
35 Streamline comparison for the GIT configuration with a pressure jump actuator disk. 81
36 C_p distribution for the GIT configuration with a uniform and linear source based actuator disk. 83
37 C_p contours for GIT configuration with a uniform and linear source based actuator disk. 83
38 GIT vorticity iso-surfaces with a linear actuator disk. 84
39 GIT vorticity contours at $X/R = 2.0$ with a linear actuator disk. 85
40 C_p contours for ROBIN configuration with a pressure jump actuator disk boundary condition. 86
41 ROBIN front cross-section C_p due to the uniform and linear actuator disk. . 88
42 ROBIN rear cross-section C_p due to the uniform and linear actuator disk. . . 89
43 ROBIN downwash measurements through the rotor disk 90
44 Streamlines for the ROBIN configuration (μ=0.15). 90
45 GIT vorticity iso-surfaces with the blade element model. 91
46 GIT vorticity contours at x=2.0 with the blade element model. 92
47 GIT flap contribution comparison for the blade element model. 93
48 GIT effect of the drag force on the blade element model. 94
49 GIT effect of the drag force on v velocity in the y=0 plane. 94
50 Two dimensional blade downwash resulting from a point and line vortex. . 96
51 GIT fuselage force history with actuator blade model. 97
52 GIT fuselage moment history with actuator blade model. 97
53 GIT upper centerline unsteady Cp variation with the actuator blade model. 99

54 GIT vorticity iso-surfaces with actuator blade model. 100
55 Mach contours for a supersonic ramp. 100
56 Mach contours for a supersonic ramp. 101
57 C_p in the overlap region for the GIT configuration. 102
58 U velocity in the overlap region for the GIT configuration. 103
59 GIT overset time averaged upper centerline C_p distribution. 103
60 GIT overset time averaged right centerline C_p distribution. 104
61 GIT overset time averaged left centerline C_p distribution. 105
62 GIT overset vorticity iso-surface at $\psi = 1080°$ viewed from above. 106
63 Dauphin rotor off centerline C_p distribution. From Reference [111]. 108
64 Dauphin rotor off lower centerline C_p distribution with strut. From Reference [111]. 110
65 Dauphin upper centerline C_p distribution with an actuator disk. From Reference [111]. 111
66 Dauphin ω_x contours at $X = 1.1375m$. From Reference [111]. 112
67 ROBIN C_p contours at $Y = 0$ with various actuator disk loadings. 118
68 ROBIN ω_x contours at $X = 1.35$ with various actuator disk loadings. 119
69 ROBIN w velocity contours at the tail center plane ($Z = 0.04$) with various actuator disk loadings. 120
70 ROBIN rotor wake visualization with overset rotor blades ($Q = 0.001$). . . . 122
71 ROBIN rotor wake visualization with overset rotor blades, top view ($Q = 0.001$). 123
72 ROBIN unsteady surface C_p for $\psi = 6°$ to $30°$. 126
73 ROBIN unsteady surface C_p for $\psi = 36°$ to $60°$. 127
74 ROBIN unsteady surface C_p for $\psi = 66°$ to $90°$. 128
75 ROBIN unsteady surface C_p at $X = 0.052$ and $X = 0.096$. 129
76 ROBIN unsteady surface C_p at $X = 0.201$ and $X = 0.256$. 130
77 ROBIN unsteady surface C_p at $X = 0.467$ and $X = 0.600$. 131
78 ROBIN unsteady surface C_p at $X = 0.896$ and $X = 1.001$. 132
79 ROBIN unsteady surface C_p at $X = 1.180$ and $X = 1.368$. 133
80 ROBIN unsteady surface C_p at $X = 1.556$. 134
81 ROBIN centerline C_p comparison with various rotor models. 135

82 ROBIN rotor wake visualization with various rotor models ($|\omega| = 0.50$). . . . 136

83 ROBIN rotor wake visualization with various rotor models, top view ($|\omega| = 0.50$). 137

LIST OF SYMBOLS AND ABBREVIATIONS

a	Speed of sound, $\sqrt{\gamma RT}$.
A	Rotor disk area, πR^2.
c	Chord length.
$\vec{F}$	Flux vector.
L_{ref}	Reference length.
$\vec{q}$	State vector of conserved variables.
$\vec{Q}$	Volume average of the conserved variables, $\frac{\int_V \vec{q} dV}{V}$.
Q	Q criteria for vortex visualization.
r	Blade section radius.
R	Blade tip radius.
$\vec{S}$	Source vector.
T	Rotor thrust.
V	Velocity.
V_{climb}	Vertical climb velocity.
v_i	Induced velocity.
C_D	Drag coefficient, $\frac{D}{\frac{1}{2}\rho V^2 S}$.
C_L	Lift coefficient, $\frac{L}{\frac{1}{2}\rho V^2 S}$.
C_p	Pressure coefficient, $\frac{p-p_\infty}{\frac{1}{2}\rho V^2}$.
C_p^*	Modified pressure coefficient, $\frac{p-p_\infty}{\rho(\Omega R)^2}$.
C_T	Thrust coefficient, $\frac{T}{\rho \pi R^2 (\Omega R)^2}$.
α	Angle of attack ($\alpha > 0$: nose up).
β	Yaw angle ($\beta > 0$: nose left).
μ	Advance ratio, $\frac{V_\infty}{\Omega R}$.
ρ	Density.
σ	Rotor Solidity, $\frac{N_{blade} c}{\pi R}$.
ω	Vorticity.

Ω	Rotor angular velocity ($\Omega > 0$: counter-clockwise viewed from above).
$C_\bullet$	Cosine Function.
$\overline{\bullet}$	Dimensional quantity.
$\bullet_\infty$	Freestream quantity.
$S_\bullet$	Sine Function.
$\hat{\bullet}$	Unit vector.
$\vec{\bullet}$	Vector quantity.
6DOF	Six Degree Of Freedom.
AFDD	Aeroflightdynamics Directorate.
CFD	Computational Fluid Dynamics.
CSD	Computational Structural Dynamics.
DCI	Domain Connectivity Information.
DiRTlib	Donor Interpolation Receptor Transaction Library.
FUN3D	Fully Unstructured Navier-Stokes 3D.
GIT	Georgia Institute of Technology.
MoA	Memorandum of Agreement.
NACA	National Advisory Committee for Aeronautics.
NASA	National Aeronautics and Space Administration.
ONERA	Office National d'Études et de Recherches Aérospatiales.
RANS	Reynolds Averaged Navier-Stokes.
ROBIN	Rotor Body Interaction.
SUGGAR	Structured Unstructured Generalized Grid Assembler.
w.r.t.	With Respect To.

SUMMARY

Helicopters and tilt-rotor aircraft exhibit complex aerodynamic phenomena resulting from an unsteady, vortical wake generated by the rotating blades. The complex nature of the rotor wake makes it difficult to obtain accurate predictions of the flow with the traditional forms of analysis. Since the vehicle aerodynamics have a direct influence on performance, handling, and the loads on the structure, the inability to obtain accurate airloads can potentially affect the design of the entire system. This ultimately leads to increased life-cycle costs to own and operate the vehicle.

Computational fluid dynamics (CFD) provides the helicopter designer with a powerful tool for identifying problematic aerodynamics. Through the use of CFD, design concepts can be analyzed in a virtual wind tunnel long before a physical model is ever created. Traditional CFD analysis tends to be a time consuming process, where much of the effort is spent generating a high quality computational grid. Recent increases in computing power and memory have created renewed interest in alternative grid schemes such as unstructured grids, which facilitate rapid grid generation by relaxing restrictions on grid structure.

Three rotor models have been incorporated into a popular fixed-wing unstructured CFD solver to increase its capability and facilitate availability to the rotorcraft community. The benefit of unstructured grid methods is demonstrated through rapid generation of high fidelity configuration models. The simplest rotor model is the steady state actuator disk approximation. By transforming the unsteady rotor problem into a steady state one, the actuator disk can provide rapid predictions of performance parameters such as lift and drag.

The actuator blade and overset blade models provide a depiction of the unsteady rotor wake, but incur a larger computational cost than the actuator disk. The actuator blade model is convenient when the unsteady aerodynamic behavior needs to be investigated,

but the computational cost of the overset approach is too large. The overset or chimera method allows the blades loads to be computed from first principles and therefore provides the most accurate prediction of the rotor wake for the models investigated. The physics of the flow fields generated by these models for rotor / fuselage interactions are explored, along with efficiencies and limitations of each methodology.

CHAPTER I

INTRODUCTION

1.1 Background

Helicopters have come a long way since the first ones flew in the early twentieth century. Modern designs are capable of flying significantly higher and faster than their predecessors. Much of this progress can be directly attributed to better analysis techniques, which allow designers to make more informed decisions. In light of the advances made thus far, next generation helicopters and tilt-rotors will be expected to have even greater demands for improved performance and reduced operational costs. To satisfy this demand, improved analysis techniques will need to be available to the designer.

The difficulty with traditional analysis techniques is that the complex nature of the rotor wake typically violates at least one of the aerodynamic assumptions governing the use of such tools. Kunz [1] concludes that the weakest aspect of the current analysis capability is in the aerodynamic predictions. Therefore, the probability of failing to predict some type of critical aerodynamic behavior is high for traditional analysis models. Unexpected aerodynamic behavior is typically detrimental and can affect the aircraft in a variety of ways, including:

- Performance: Poor aerodynamics reduces the aircraft's ability to accomplish its mission.
- Handling: Poor aerodynamics can also lead to reduced control system effectiveness, degrading the stability characteristics of the aircraft.
- Vibration: The periodic aerodynamic loading can lead to structural vibrations and can be a source of annoyance to the pilot. reducing his/her endurance.
- Maintenance: Unexpected aerodynamic loading can lead to increased fatigue on components forcing them to require more frequent repair.

- Noise: A variety of aerodynamic interactions can increase the noise generated by the aircraft during operation.

All of these items lead to an increase in the cost to own and operate the vehicle. Occasionally, a problem becomes significant enough that the engineers are forced to redesign components, which also has significant associated costs.

The airloads prediction problem stems from the fact that the rotating blades generate a complex, unsteady wake dominated by vortical structures. Figure 1 shows a typical wake structure generated over a simple fuselage in forward flight. The rotating blades shed a vortex sheet over the length of the blade and a strong tip vortex at the blade tip. These vortex elements propagate downstream and interact with the rotating blades, the fuselage, and previously shed vorticity. The interactions between the blade and vortex have a significant impact on the airloads and noise generated by a rotor. The predominant vortex to vortex interaction is the rolling up of the blade tip vortices into a concentrated vortex on both sides of the configuration. The natural asymmetry of the flow is apparent when comparing the advancing and retreating tip vortex roll up. All of these interactions need to be adequately modeled in an aerodynamic analysis to obtain useful engineering information for design.

Computational fluid dynamics (CFD) has the potential to provide the helicopter designer with an analysis tool capable of evaluating complex rotary wing aerodynamics. In a recent review of CFD techniques, Strawn, Cardonna, and Duque [2] concluded that the ability to perform routine computations on full helicopter configurations is rapidly approaching. Despite the advances in CFD modeling, the industry has been slow to adopt the use of such models for vehicle design. One of the primary difficulties encountered with current CFD techniques is the large amount of time it takes to set up the computational grid for a configuration. If multiple designs need to be evaluated the use of these CFD techniques can become prohibitively expensive. However, recent increases in computing power and memory have created renewed interest in alternative grid schemes such as unstructured grids, which facilitate rapid grid generation by relaxing restrictions on grid structure. The advancement of an unstructured method for use in rotary wing analysis is

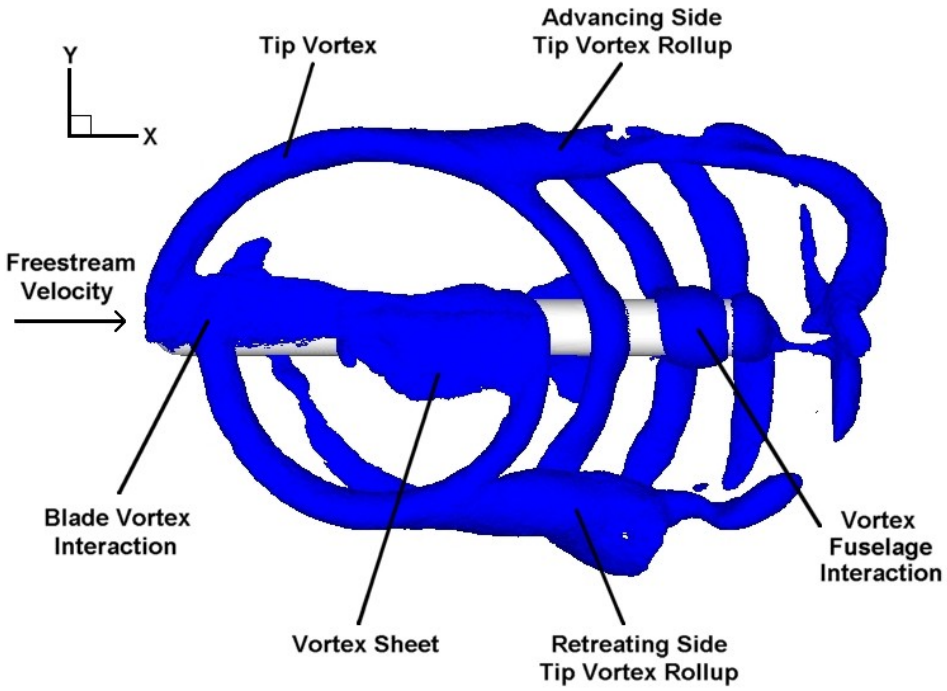

Figure 1: Vortex wake structure over a simple model in forward flight.

described in the present work.

1.2 Literature Review

Much of the literature pertaining to helicopter aerodynamics is concerned with the prediction of the main rotor forces and induced velocities. A thorough overview of the early research and analysis techniques can be found in books by Johnson [3], Prouty [4], Leishman [5], and Stepniewski & Keys [6]. The current review focuses primarily on rotor / airframe interactions. However, some of the more novel techniques for predicting main rotor aerodynamics will also be examined, since these methods hold promise for application to complete configurations.

1.2.1 Experimental Investigations

Initial investigations into the nature of rotor airframe interactions were conducted primarily by experimentation. At NASA Langley Research Center, Wilson and Mineck [7, 8] conducted a study of three helicopter fuselage models representative of attack, utility, and scout models. This study observed that the rotor wake increases the fuselage yawing

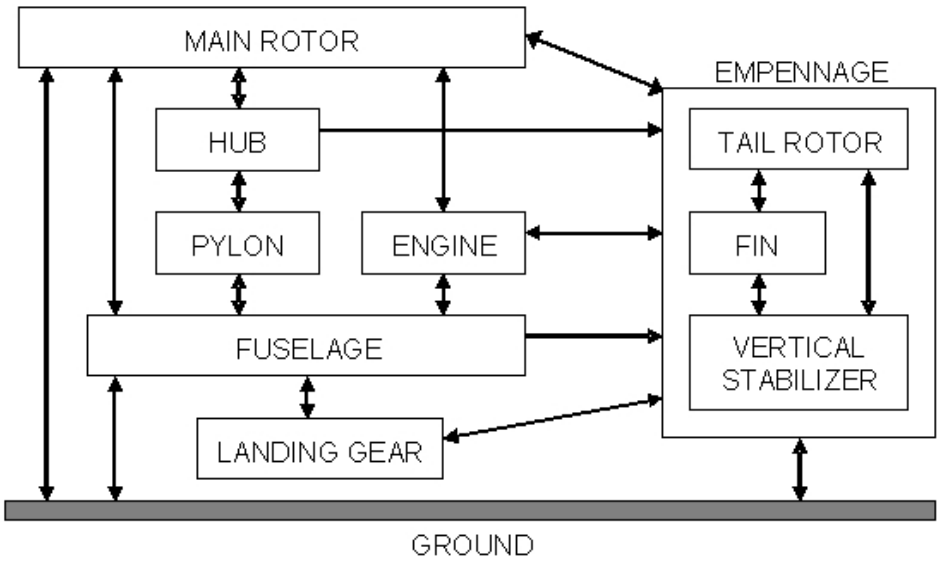

Figure 2: Aerodynamic interactions for a typical helicopter. Adapted from Sheridan and Smith [10]

moment for large sideslip angles, causing increased tail rotor anti-torque requirements. In another series of tests Freeman and Mineck [9] measured the fuselage surface pressures on a generic helicopter configuration for a variety of flight conditions. This latter study was presented without analysis and served primarily as a database for validating analysis methods.

One of the first detailed investigations into the nature of helicopter interactions was conducted by Sheridan and Smith [10] during the Boeing Vertol UTTAS development program. The authors coined the phrase "Interactional Aerodynamics" to describe the complex aerodynamic interactions that occur when various components of the design are placed in close proximity. Figure 2 shows a depiction of many of the interactions identified during this study. It is important to solve the aerodynamics accurately for each of the components in 2 if an analysis of the entire vehicle is needed. Thus, to solve the interactional aerodynamics problem Sheridan and Smith stressed a need for improved analysis techniques that includes all of these components.

To achieve the goal of understanding and quantifying these interactional aerodynamics, a number of experiments have been performed. A series of rotor / airframe interaction experiments were conducted at the Georgia Institute of Technology (GIT) [11]-[18]

to enhance the understanding of interactional aerodynamic phenomena and provide an extensive database for code validation. Previous experimental studies focused on testing realistic helicopter shapes, but the GIT researchers reasoned that this only adds complexity to an already difficult problem. To simplify the fuselage geometry a simple cylindrical body with a hemispherical nose was analyzed. The work conducted by Brand focused primarily on the fuselage surface pressures while Liou's research concentrated on the rotor wake visualization.

Researchers at NASA Langley returned to the rotor airframe interaction problem by studying the rotor wake in the vicinity of the ROtor Body INteraction (ROBIN) model used by Freeman and Mineck [9]. This led to a series of reports detailing the inflow at various advance ratios for a set of rectangular [19]-[27] and tapered [28, 29] blades. Ghee and Elliott [30] used the ROBIN model to study the tip vortex trajectory. They noted an increased downwash and observed a tighter vortex rollup on the advancing side. More recently, another experiment was conducted by Mineck and Althoff-Gorton [31] using the ROBIN model to obtain unsteady surface pressures. They observed that the influence of the rotor wake on the steady surface pressures is greater at lower advance ratios and that the blade passage effect is greatest over the nose and tail boom of the model.

The aerodynamic interaction between the main rotor and the fuselage has also been investigated at the University of Maryland [32]-[34]. They identified four mechanisms for the unsteady surface pressures.

- Blade passage
- Close wake interactions with the body
- Wake impingement on the body
- Post wake impingement

The first two items were identified as inviscid flow phenomena and the latter two were identified as viscous phenomena.

ONERA has also performed a variety of rotor / airframe interaction studies [35]-[37] on a 1/7.7 scale model of the Eurocopter Dauphin helicopter. These tests focus on studying

the rotor wake effects on a real helicopter and providing a database for code validation on a complex configuration. This model allows analysis methods to be validated on a configuration more relevant to the rotary wing community.

1.2.2 Potential Methods

One of the first attempts to account for the interaction between the main rotor and fuselage is given in Landgrebe [38]. In this approach a comprehensive rotor code was coupled with a fuselage panel method to study the interaction between the two components. This study showed that the fuselage upwash alters the rotor inflow, causing an increase in the effective angle of attack of the blades.

Clark and Maskew [39, 40] developed a method for coupling a traditional fuselage panel method with a blade element representation for the rotor. In this method the rotor and fuselage singularity strengths were computed simultaneously. The rotor wake was then allowed to deform in response to the fuselage presence and changes in the rotor wake loading.

A source panel fuselage method was coupled with a lifting line, prescribed wake rotor analysis by Lorber and Egolf [41] to predict unsteady fuselage loads. In this approach the vortex elements wrapped around the fuselage to prevent intersecting with the body. Initially the prescribed vortex wrapped around the upper portion of the fuselage. Once a wake displacement criteria was achieved, the vortex would flip to the bottom of the fuselage.

Mavris [42, 43] developed a source/doublet panel fuselage method coupled with a lifting line, free wake rotor analysis to predict unsteady fuselage loads. He observed that predictions over the top of the configuration were satisfactory, but that the trends over the sides were poor. He attributed this to the fact that vortex surface interactions are complex and can exceed the capabilities of the model.

Berry and Bettschart [36] compared the capabilities of three potential-based codes for predicting the rotor / fuselage interactions on the Dauphin model. They found that unexpected periodic velocity predictions were obtained when the vortex elements passed in

close proximity to the measurement location. Differences between the singularity methods and experiment were also noted in the region of the hub, where large separation effects were assumed to exist.

One of the difficulties encountered with potential methods is that there is a lot of empiricism built into the models (e.g. vortex core size, vortex core velocity, fuselage displacement model, etc.). Another difficulty is that these models are based on the unsteady potential equation, which does not include viscous effects. If viscous effects are not accounted for, the method will be incapable of predicting separation and the vehicle drag unless some type of empirical model or boundary layer code coupling is applied.

1.2.3 Structured Euler/Navier-Stokes Methods

Rajagopalan, et. al. [44, 45] developed a source based actuator disk method, in which the influence of the rotor is modeled as a set of forces that are applied to the flow field in cells intersecting the rotor disk. Rotor fuselage interactions were investigated using this method by Zori, et. al. [46]. Good agreement was obtained with the steady pressure coefficients measured on the GIT configuration. A variety of other cases, such as a V-22 and CH-47, have also been examined and are discussed in a review by Rajagopalan [47].

Fejtek and Roberts [48] computed steady-state solutions of a tilt rotor configuration in hover using an actuator disk model. The actuator disk was modeled using a pressure jump boundary condition with swirl effects. A thin layer Navier-Stokes solver using a structured grid was utilized in the study. Chaffin and Berry [49, 50] computed steady state solutions over the ROBIN configuration using an actuator disk rotor model. This model was incorporated into a structured overset RANS solver. The actuator disk model was implemented as a pressure jump boundary condition and had the ability to model swirl. However, they noted that the use of the swirl condition could lead to nonphysical solutions.

Bettschart [51] also used a structured RANS method to study rotor fuselage interactions with an actuator disk method. In this approach he used a source-based actuator disk with uniform and nonuniform loading options. The nonuniform loading was obtained by time averaging the loading generated by a lifting line method with a prescribed wake. He shows

good correlation with momentum theory and obtains good results comparing with ROBIN steady pressure measurements. Le Chuiton [52] utilized a main rotor and tail rotor actuator disk to study the effect of the rotor downwash on engine exhaust. In this approach a source based actuator disk boundary condition along with engine inflow / outflow boundary conditions were utilized in a structured code to model the EC-145 Helicopter. The rotor wash was found to significantly alter the path of the hot engine exhaust.

Boyd et al. [53, 54] coupled a generalized dynamic wake theory (GDWT) with a thin layer Navier-Stokes code to develop an unsteady actuator disk model. A pressure jump actuator disk boundary is utilized, but rather than using the time averaged rotor forces an instantaneous loading is applied. The generalized dynamic wake theory is loosely coupled to the structured solver to provide the loading via the actuator disk boundary condition. The NS solver then provides the GDWT with an inflow correction and the process continues until a satisfactory convergence is achieved. Tadghighi [55] also developed an unsteady actuator disk model, but utilized a source-based actuator disk.

The development of overset grids simplified the grid generation process for structured grids. It also allows the relative motion between the rotor blades and fuselage. Hariharan [56] used a structured overset RANS solver to study the rotor fuselage interactions on the GIT rotor airframe interaction model. In this work a fifth-order spatially accurate ENO scheme was applied to improve the ability to capture the tip vortex. Noack [57, 58] has developed a generalized library for adding overset capabilities to any type of flow solver. Recent efforts at ONERA [59, 60] and DLR [61, 62] have also added overset capability to their flow solvers.

One of the most detailed solutions performed to date is attributed to Strawn and Djomehri [63]. They used a structured overset RANS solver to study the UH-60A rotor in hover. For this study sources were added to the solver to mimic the rotational flow of the blades. Their results showed good correlation with experiment for the rotor torque and figure of merit, but they consistently noted an over prediction in the blade loading near the tip. They attempted to minimize grid dependence by running a 64 million node grid, but found that the vortex diffusion still exceed the observed experimental behavior. They

suggest that circulation from the previous blade's tip vortex migrates through the shear layer to augment the newly created tip vortex.

Potsdam and Strawn [64] studied a half span and full span V-22 configuration using a structured overset RANS solver. Since the rotor and fuselage are present in this study the blades are modeled dynamically (i.e. rotational source terms are not used). The full span configuration was modeled with 47.6 million nodes. This study provided a detailed look at the unsteady fountain effects over the V-22 wings in hover. More recent studies by Potsdam are given in [65].

1.2.4 Unstructured Euler/Navier-Stokes Methods

Structured grid solvers are currently the leading CFD analysis methods for solving helicopter aerodynamic problems. However, structured grids tend to be very time consuming to generate, especially on complex geometries. For this reason unstructured methods have generated increasing interest in recent years. Unstructured methods allow the grid generation process to be more automated, which greatly reduces the time and effort required to generate a grid. Another benefit of unstructured grids is that they lend themselves to adaptation more easily than a structured grid. Structured adaptation requires global refinement in that splitting a cell requires all cells in a grid plane to be split in order to retain the grid structure. An unstructured method allows for local refinement, since the grid can be adapted in a region of interest without affecting the rest of the mesh.

Strawn and Barth [66] developed an unstructured Euler solver to investigate rotary wing aerodynamics problems. In this approach rotational sources are added to the flow to simulate the blade rotation. A cell splitting technique was applied which divided one cell into eight new ones. To maintain connectivity with the rest of the grid, neighboring cells would become buffer cells which would split with a 1 to 4 or 1 to 2 ratio as required. Kang and Kwon [67] have more recently applied a similar adaptation technique to an Euler code.

Bottasso and Shephard [68] have applied a finite-element-based Euler solver for solving rotary wing aerodynamics. This method also used an adaptive strategy, but focused primarily on shock capturing at the blade tip rather than on wake refinement. This study

addressed the issue of load balancing an adaptive scheme when a parallel implementation is used.

Pan, Chao, and Chien [69] used an unstructured Euler code to model rotating blades within a single mesh. They used a sliding mesh approach to model the blade rotation relative to a stationary fuselage grid. In the sliding mesh approach a cylindrical grid centered at the axis of rotation is created for the rotating components. The cylindrical grid fits into a cylindrical hole created in the stationary grid and the two components transfer information through the sliding boundary. A nice feature of this approach is that flux conservation can be guaranteed across the interface, which is not true for an overset approach.

Kang and Kwon [67, 70] investigated the effect of adaptation on the rotor wake using an unstructured adaptive solver. The blade rotation was modeled through the use of rotational sources. In the first study [67] an Euler method was utilized. The subsequent study [70] used an RANS solver to examine the effect of viscosity on the rotor performance.

Lee and Kwon [71] were one of the first to implement an actuator disk boundary condition into an unstructured solver for the solution of rotor fuselage interactions. They used a pressure jump boundary condition and computed the blade loading with the blade element method. They compared with data from the GIT rotor airframe interaction model and obtained good correlation. Although their method showed a better forward peak prediction than Zori et. al. [46], their method did not do as well predicting the aft pressure peak.

O'Brien and Smith [72] showed that the correlation between the pressure peaks depends on whether a blade flapping velocity contribution is included in the blade element method. Zori et. al. [46] included the blade flapping, but Lee and Kwon [71] did not. When blade flapping is neglected the forward peak compares well with experiment, but the aft peak diminishes. If included, the blade flapping provides a good match with the aft peak, but the forward peak is greatly reduced.

A source-based actuator disk boundary condition has been developed by Schweikhard and Le Chuiton [73]. They compared the results of the unstructured code with a structured

code and found good correlation between the two methods. An unusual finite thickness actuator disk has been developed by Heise et al. [74] for studying rotor / fuselage interactions. This method assumes that the flow vectors do not change significantly across the thickness of the disk. This approach is based on a method developed for axial flow fans, in which the dominant flow direction is normal to the disk. Heise acknowledges that this may not work well for high advance ratios, but good correlation with lower advance ratios in the ROBIN experiment was obtained.

Park et al. [75, 76] also computed the rotor fuselage interaction using an unstructured sliding mesh approach for the GIT and ROBIN models. Grid adaptation was also utilized to improve the rotor wake resolution and blade pitch changes were modeled using a deforming mesh approach. The aft pressure peak was under predicted, but the blade flapping was not included. The ROBIN results show good peak to peak correlation with the unsteady surface pressures.

O'Brien and Smith [77] computed an unstructured Euler solution using overset grids. In this study a good correlation with experiment was obtained, but the solution was found to degrade over the sides of the fuselage. The degraded accuracy over the sides of the geometry were attributed to vortex dissipation and the lack of a viscous vortex / surface interactions.

The unstructured methods thus far have focused on tetrahedral unstructured methods. However, efforts are also underway to apply Cartesian unstructured grid methods to rotorcraft aerodynamics [78]. Cartesian methods allow for convenient grid adaptation, but are more difficult to utilize near curved surfaces for viscous flows.

1.2.5 Other Techniques

Hybrid methods couple a free wake analysis with a near-body Euler or Navier-Stokes scheme. Moulton, et al. [79] was one of the first to couple a Navier-Stokes method with a free-wake model to study a hovering rotor. Hybrid methods improve computational efficiency by eliminating the need to solve the Navier-Stokes equations in the off-body regions. They also help to prevent the diffusion of the tip vortex, since the vorticity does

not diffuse after it gets captured in a vortex filament upon leaving the near-body grid.

Another option for reducing the rotor wake is to utilize a vorticity confinement scheme [80]. In this approach an extra term is added to the momentum equations to reduce the diffusion of the tip vortex. The confinement term drives vorticity inward in vortical regions and is zero in irrotational regions. The difficulty in this approach is in determining an ideal value for the confinement term. However, this method can lead to significantly faster computation times than traditional RANS based methods.

The vorticity transport model [81, 82] provides one method for addressing the vortex diffusion that occurs by solving the RANS equations. With this model the momentum equations are recast in a vorticity conservation form. The vector form of the incompressible momentum equations is shown below.

$$\frac{\partial \vec{V}}{\partial t} + \vec{V} \bullet \nabla V = \frac{-\nabla p}{\rho} + \nu \nabla^2 \vec{V} \tag{1}$$

By taking the curl of Equation 1 the unsteady vorticity transport equation is obtained.

$$\frac{\partial \vec{\omega}}{\partial t} + \vec{V} \bullet \nabla \omega - \vec{\omega} \bullet \nabla \vec{V} = \nu \nabla^2 \vec{\omega} \tag{2}$$

The primary advantage of this approach is that numerical diffusion can not cause the loss of vorticity, since it is a conserved quantity. However, the compactness of the vortex structures will still be a function of the grid resolution.

1.2.6 CFD / CSD Coupling

In the present study the experimental models have stiff rotor blades. This would not be the case for a typical helicopter which has highly flexible blades. To be applicable to a broad range of problems an aerodynamic solver needs to be coupled with a computational structural dynamics (CSD) code. For completeness a brief description of the current state of the art in airloads prediction is presented.

CFD /CSD coupling has provided some of the most accurate helicopter airloads predictions to date. Efforts to couple CFD methods with comprehensive analysis methods are currently in progress as part of the UH-60 Airloads Workshop. A review of the current progress is presented in Datta, et. al. [83]. In general it has been observed that loose

coupling schemes have similar accuracy to tight coupling schemes for periodic problems. Since the tight coupling scheme requires significantly more computational effort, loose coupling schemes have been generally preferred for level flight conditions. Potsdam, et al. [84] have demonstrated some of the best CFD / CSD coupling results to date for the UH-60, using a loose coupling approach.

Sitaraman, et al. [85] have examined the physical mechanisms associated with CFD / CSD coupling. For high speed cases, coupling offers the biggest benefit, since the CFD is naturally able to predict the complex transonic flow effects for the advancing rotor. This leads to a significantly improved pitch moment calculation. At flight conditions where dynamic stall occurs, CFD also offers improvement in the prediction of stall effects, but the benefits are sensitive to grid spacing and turbulence modeling. Low speed cases see a strong wake interaction, which is also going to be highly sensitive to the grid spacing of the CFD mesh.

Additional CFD / CSD coupling efforts have also been performed under the French-German CHANCE program [86, 87]. The CHANCE program is focused on developing and validating CFD for computing the aerodynamics of complete helicopters. In their work they confirmed that there is little difference between loose and tight coupling for steady flow conditions.

1.3 Research Objectives

The objective of the present effort is to develop phenomenological and first-principles-based approaches for modeling complete rotorcraft configurations. In doing so the following contributions will be made to the field of rotary wing aerodynamics:

1. The importance of modeling all aspects of a configuration will be demonstrated.

2. The flexibility of using a source model instead of a pressure jump boundary condition actuator disk approach will be evaluated.

3. A new unsteady actuator blade approach based on the use of source terms will be developed and tested.

4. An overset technique will be integrated into the unstructured flow solver and applied to a complete rotorcraft configuration.

5. A comparative study of the physics associated with each of the rotor models will be performed. Limitations on simplified models will be determined, and efficiency of each method will be compared.

As a result of this investigation a suite of tools will be developed for modeling complex rotorcraft configurations using an unstructured flow solver to demonstrate the efficacy of each tool.

CHAPTER II

COMPUTATIONAL METHOD

2.1 Overview

Engineering analysis typically requires a fast response time. While computers have the ability to rapidly perform the required computations, the task of adequately defining the problem lies with the engineer. All computational analysis requires the engineer to create inputs for the computer to define the problem of interest. For a computational fluid dynamics (CFD) analysis, a computational grid must be generated which divides the region of interest (i.e. the configuration and the air around it) into discrete elements. The generation of the computational grid is typically the most time consuming portion of the solution process, especially when working with a complex geometry.

Computational grids are divided into two categories based on the grid organization: structured and unstructured. As the name implies, the structured grid utilizes an organized structure that enables neighboring cells to be identified via increments in the indexing scheme. An unstructured method has a relaxed structure, wherein neighboring cells are identified through a grid connectivity array. The use of a grid connectivity array increases the memory usage for an unstructured scheme. The arbitrary connectivity also causes the governing equations to result in a sparse matrix system, which cannot be solved as efficiently as the banded matrix system typical to a structured grid scheme. However, the relaxed grid structure allows unstructured grids to be significantly simpler and less time-consuming to generate.

The inefficient nature of unstructured grids caused structured methods to initially develop as the preferred option, since they made more efficient use of limited computational memory resources. However, with the rapid growth of computer memory and power over the last several years, renewed interest in the utilized of unstructured methods has arisen. Parallel processing has also enabled difficult problems to be broken into smaller parts,

allowing a problem that requires ten hours on a single processor to be solved on ten processors in parallel in approximately one hour. The limiting nature of computational resources has continued to decrease over time, which justifies the use of an unstructured method for the significantly reduced grid generation time [88]. Structured grids typically neglect or simplify complex component surfaces, but unstructured grids enable complex geometries to be generated without simplification.

A description of the software utilized in this effort is provided in this chapter. In an effort to concentrate primarily on rotary-wing aerodynamic configurations, a preexisting fixed-wing solver was modified. To enable the helicopter blades to rotate, additional software is incorporated into the flow solver to provide the capability to utilize overset grids. The first section provides an overview of the capabilities of the flow solver selected for this effort. The subsequent sections discuss the overset solver library and the overset mesh assembly program. The final section provides an overview of the unstructured grid generation system.

2.2 Flow Solver

NASA Langley Research Center's Fully Unstructured Navier-Stokes 3D (FUN3D) flow solver [89]-[92] was selected for the current work. FUN3D solves the Reynolds-Averaged Navier-Stokes (RANS) equations using an unstructured, tetrahedral-based discretization of the region of interest. The solver is fully parallel, allowing it to reduce solution times by distributing work across multiple processors. Since this flow solver has been documented in the references, only pertinent aspects of the code will be reviewed in this section.

One of the enabling features of FUN3D is the use of version control software to ensure that only two versions of the code exist at any given time: a release version and a development version. This significantly improves the commonality of the code, since users are ensured that they can duplicate the results obtained by anyone else. A rigorous test suite is evaluated continuously to ensure that the solver remains robust even when multiple developers are making changes to the source code [93].

The governing equations are solved using a node-centered finite volume scheme. In a

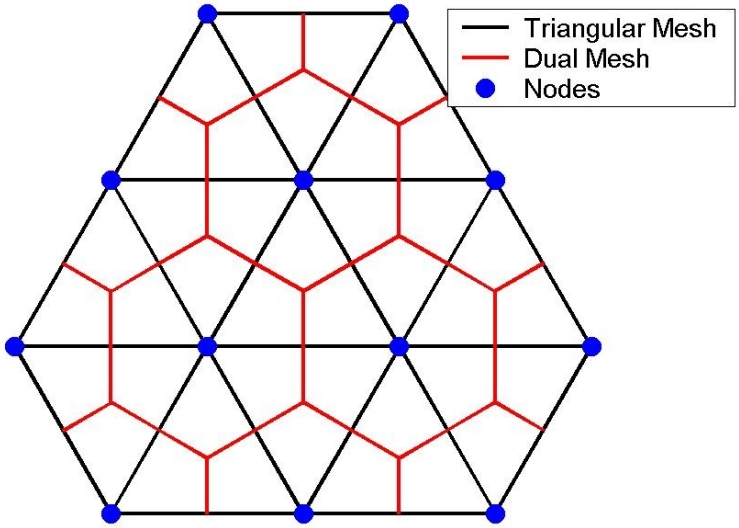

Figure 3: Node based dual mesh with original triangular mesh.

node-centered scheme the flow variables are stored at each vertex of the tetrahedral mesh rather than at the centroid of the tetrahedral cell. The control volume surrounding the node is conventionally referred to as the dual cell, since these cells form a mesh that is considered 'dual' to the tetrahedral mesh. A two-dimensional example of the dual mesh for a node-centered scheme is shown in Figure 3. With this approach each dual cell takes on an arbitrary polyhedral shape that depends on the number of tetrahedron that share the node. Inviscid fluxes are evaluated by looping over the edges of the tetrahedral mesh, since each edge corresponds to a dual cell face. The viscous flux terms are computed using an element-based approach.

One of the distinctive features of this code is the ability to solve both the compressible and incompressible RANS equations. The compressible equations are characterized as hyperbolic equations, which are solved by marching forward in time. The incompressible RANS equations are elliptical in nature and depend entirely on the boundary conditions. Unfortunately, different strategies are required to solve hyperbolic and elliptic equations. However, Chorin's [94] artificial compressibility method transforms the elliptical incompressible RANS equations into a hyperbolic set of equations, allowing the same solution procedure to be utilized for both forms of the RANS equations. The ability to accurately solve for low Mach number flows is important for helicopters, since the flow around the

fuselage is typically in the incompressible regime. The compressible equations have been found to become increasingly stiff as the Mach number is reduced due to disparity in the eigenvalues [95]. For low speed compressible flows the maximum eigenvalue tends toward the speed of sound and the minimum eigenvalue goes to zero. Since the stiffness of the system is proportional to the ratio of the eigenvalues, the stiffness tends toward infinity as the Mach number goes to zero, and the compressible solution has trouble obtaining converged solutions. The fix for this problem in many compressible codes is the use of a low Mach number preconditioning factor [96]. The incompressible formulation modifies the speed of sound to reduce the disparity of the eigenvalues and relax the stiffness of the resulting system of equation [91]. While the solutions are similar in principle, the outcome is very different.

Turbulence is modeled using either the Spalart-Allmaras [97] one-equation turbulence model or the two equation k-ω SST model [98]. The turbulence model can be solved in either a loosely-coupled or tightly-coupled manner, but only the loosely-coupled Spalart-Allmaras model is used in current work.

The integral form of the governing equations is written as

$$\frac{\partial}{\partial t}\iiint_V \vec{q}\,dV + \oiint_\Omega \left(\vec{F}_i \bullet \hat{n}\right) d\Omega - \oiint_\Omega \left(\vec{F}_v \bullet \hat{n}\right) d\Omega = \vec{S} \tag{3}$$

where $\hat{n}$ is the outward pointing unit normal on the boundary face of the dual cell. The state vector of conserved variables is denoted as $\vec{q}$ and the inviscid and viscous flux vectors are denoted by $\vec{F}_i$ and $\vec{F}_v$, respectively. The volume of the dual cell is given as V and the surface area is given as Ω. An optional source vector, $\vec{S}$, can also be added to the governing equations to model other forces acting on the fluid volume.

The components of the state vector and flux vectors for the compressible form of

Equation 3 are:

$$\vec{q}_{compressible} = \begin{bmatrix} \rho \\ \rho u \\ \rho v \\ \rho w \\ E \end{bmatrix} \tag{4}$$

$$\vec{F}_{i,compressible} \bullet \hat{n} = \begin{bmatrix} \rho\left(\vec{V} - \vec{W}\right) \bullet \hat{n} \\ \rho u\left(\vec{V} - \vec{W}\right) \bullet \hat{n} + p n_x \\ \rho v\left(\vec{V} - \vec{W}\right) \bullet \hat{n} + p n_y \\ \rho w\left(\vec{V} - \vec{W}\right) \bullet \hat{n} + p n_z \\ (E+p)\left(\vec{V} - \vec{W}\right) \bullet \hat{n} + p\vec{W} \bullet \hat{n} \end{bmatrix} \tag{5}$$

$$\vec{F}_{v,compressible} \bullet \hat{n} = \begin{bmatrix} 0 \\ \tau_{xx} n_x + \tau_{xy} n_y + \tau_{xz} n_z \\ \tau_{yx} n_x + \tau_{yy} n_y + \tau_{yz} n_z \\ \tau_{zx} n_x + \tau_{zy} n_y + \tau_{zz} n_z \\ \left(\tau\vec{V}\right) \bullet \hat{n} - \vec{q}_{heat} \bullet \hat{n} \end{bmatrix} \tag{6}$$

For moving grid simulations the fluid velocity vector, $\vec{V} = (u, v, w)^T$, is subtracted by the grid velocity, $\vec{W}$, to obtain a velocity relative to the cell. The stress tensor, τ, consists of the following components:

$$\begin{aligned} \tau_{xx} &= \tfrac{2}{3}\tfrac{M_\infty}{Re}(\mu + \mu_t)\left(2\tfrac{\partial u}{\partial x} - \tfrac{\partial v}{\partial y} - \tfrac{\partial w}{\partial z}\right) \\ \tau_{yy} &= \tfrac{2}{3}\tfrac{M_\infty}{Re}(\mu + \mu_t)\left(2\tfrac{\partial v}{\partial y} - \tfrac{\partial u}{\partial x} - \tfrac{\partial w}{\partial z}\right) \\ \tau_{zz} &= \tfrac{2}{3}\tfrac{M_\infty}{Re}(\mu + \mu_t)\left(2\tfrac{\partial w}{\partial z} - \tfrac{\partial u}{\partial x} - \tfrac{\partial v}{\partial y}\right) \\ \tau_{xy} &= \tau yx = (\mu + \mu_t)\left(\tfrac{\partial u}{\partial y} + \tfrac{\partial v}{\partial x}\right) \\ \tau_{xz} &= \tau zx = (\mu + \mu_t)\left(\tfrac{\partial u}{\partial z} + \tfrac{\partial w}{\partial x}\right) \\ \tau_{yz} &= \tau zy = (\mu + \mu_t)\left(\tfrac{\partial v}{\partial z} + \tfrac{\partial w}{\partial y}\right) \end{aligned} \tag{7}$$

The heat flux is defined as:

$$\vec{q}_{heat} = -\frac{M_\infty}{Re\,(\gamma - 1)}\left(\frac{\mu}{Pr} + \frac{\mu_t}{Pr_t}\right)\nabla T \tag{8}$$

The Reynolds number, Re, and Prandtl number, Pr, influence the viscous terms, but do not appear in the inviscid terms. The t-subscript quantities represent turbulent values and are computed by the turbulence model.

The compressible variables are nondimensionalized by the freestream density ($\overline{\rho}_\infty$), sonic velocity ($\overline{a}_\infty$), molecular viscosity ($\overline{\mu}_\infty$), thermal conductivity ($\overline{k}_\infty$), and a reference length ($\overline{L}_{ref}$). The reference length is defined as the ratio of the reference length of the actual configuration ($\overline{L}_{actual}$) and the reference length as defined in the grid (L_{grid}).

$$\overline{L}_{ref} = \frac{\overline{L}_{actual}}{L_{grid}} \tag{9}$$

The total energy is related to the pressure through the perfect gas equation of state to close Equation 3.

$$p = (\gamma - 1)\left(E - \frac{\rho}{2}\left(u^2 + v^2 + w^2\right)\right) \tag{10}$$

The laminar viscosity is computed via Sutherland's Law:

$$\mu = \frac{1 + C}{T + C} T^{3/2} \tag{11}$$

where $C = \frac{198.6}{T_\infty}$.

When solving the incompressible form of Equation 3, the state vector and flux vectors are:

$$\vec{q}_{incompressible} = \begin{bmatrix} p \\ u \\ v \\ w \end{bmatrix} \tag{12}$$

$$\vec{F}_{i,incompressible} \bullet \hat{n} = \begin{bmatrix} \beta\left(\vec{V} - \vec{W}\right) \bullet \hat{n} \\ u\left(\vec{V} - \vec{W}\right) \bullet \hat{n} + pn_x \\ v\left(\vec{V} - \vec{W}\right) \bullet \hat{n} + pn_y \\ w\left(\vec{V} - \vec{W}\right) \bullet \hat{n} + pn_z \end{bmatrix} \tag{13}$$

$$\vec{F}_{v,incompressible} \bullet \hat{n} = \begin{bmatrix} 0 \\ \tau_{xx}n_x + \tau_{xy}n_y + \tau_{xz}n_z \\ \tau_{yx}n_x + \tau_{yy}n_y + \tau_{yz}n_z \\ \tau_{zx}n_x + \tau_{zy}n_y + \tau_{zz}n_z \end{bmatrix} \tag{14}$$

Using the artificial compressibility technique the pressure is coupled to the continuity equation through the use of the artificial compressibility parameter, β. As the problem approaches steady state, the divergence of the velocity goes to zero and the coupling disappears, recovering the elliptical form of the incompressible RANS equations. The incompressible variables are nondimensionalized as follows

$$\begin{aligned} u &= \frac{\overline{u}}{\overline{V}_{ref}} \\ p &= \frac{\overline{p}-\overline{p}_{ref}}{\overline{\rho}_{\infty}\overline{V}_{ref}^2} \\ t &= \frac{\overline{t}\overline{V}_{ref}}{\overline{L}_{ref}} \end{aligned} \tag{15}$$

The reference velocity is an arbitrary velocity which is typically taken to be the free stream velocity. However, in certain situations, such as a hovering helicopter where the free stream velocity is zero, the reference velocity is taken to be another appropriate non-zero value such as the rotor tip speed. The reference pressure is defined such that the nondimensional free stream pressure is equal to one.

$$\overline{p}_{ref} = \overline{p}_{\infty} - \overline{\rho}_{\infty}\overline{V}_{ref}^2 \tag{16}$$

An interesting aspect of this formulation is that it is possible for the nondimensional incompressible pressure to be negative. Another important feature of the incompressible form of Equation 3 is that it does not utilize the energy equation. Therefore, the incompressible formulation requires less computational effort and can be advantageous to utilize whenever it is applicable.

The inviscid flux, F_i, at the dual cell face is determined from a linear reconstruction of the variables at the nodes on either side of the face. The gradients of the variables at each node are computed using a least squares technique. Roe's flux difference splitting technique [99] is utilized to determine the value of the flux at the face. Viscous fluxes are computed using a finite volume formulation, which is equivalent to a Galerkin type approximation on tetrahedral meshes [100]. The resulting scheme is second-order spatially accurate.

Temporal discretization is achieved using either a backward Euler method for steady

Table 1: Coefficients for the Backwards Differentiation Formula

Order	ϕ_{n+1}	ϕ_n	ϕ_{n-1}	ϕ_{n-1}	ϕ_{n-2}
1	1	-1	0	0	0
2	3/2	-2	1/2	0	0
3	11/6	-3	3/2	-1/3	0
4	25/12	-4	3	-4/3	1/4

state problems or the second-order backward differentiation formula (BDF) [100] for unsteady problems. If the computational control volume does not deform over time, Equation 3 can be rewritten in terms of the volume averaged state vector as follows:

$$V\frac{\partial \vec{Q}}{\partial t} = \vec{R} \tag{17}$$

Here the viscous and inviscid flux has been lumped into the residual, $\vec{R}$. This expression can then be expanded via backwards series expansion about the time level $n+1$.

$$\frac{V}{\Delta t}\left(\phi_{n+1}\vec{Q}^{n+1} + \phi_n\vec{Q}^{n} + \phi_{n-1}\vec{Q}^{n-1} + ...\right) = \vec{R}^{n+1} \tag{18}$$

In the above expression the backward differentiation formula coefficients (ϕ) determine the temporal accuracy of the scheme. A list of coefficients up to fourth order temporal accuracy is shown in Table 1. The first order scheme in the BDF family is simply the backward Euler scheme.

Rather than linearize right hand side of Equation 18 about time level $n+1$, a pseudo time term is introduced. The pseudo time term advances the solution during each time step as if the problem were a steady-state problem. Assuming the process converges the pseudo time term disappears, leaving the solution at time level $n+1$. This approach works well with the incompressible scheme, which must achieve a zero divergence state at each time step for the solution to be physical. The resulting scheme is as follows:

$$\left[\left(\frac{V}{\Delta\tau} + \frac{V\phi_{n+1}}{\Delta t}\right)\mathbf{I} - \frac{\partial \vec{R}^m}{\partial \vec{Q}}\right]\Delta\vec{Q}^m = \vec{R}^m - \frac{V\phi_{n+1}}{\Delta t}\left(\vec{Q}^m - \vec{Q}^n\right) - \frac{V\phi_{n-1}}{\Delta t}\left(\vec{Q}^{n-1} - \vec{Q}^n\right) \tag{19}$$

Throughout this work the $\frac{\partial \vec{R}}{\partial \vec{Q}}$ term will be referred to as the Jacobian and the $\vec{R}$ term as the residual of the system of equations. The unsteady computations presented in this work

utilize the second order BDF scheme for temporal discretization. For the second-order scheme, time terms are added to the residual, but for a first-order scheme the time terms disappear from the right hand side of Equation 19. Since Equation 19 depends on the unknown conserved variables at the new time step, the system of equations needs to be solved using an iterative approach. A point-implicit or line-implicit relaxation scheme is used to iterate the solution during each time step [101].

Boundary conditions are applied implicitly through the modification of the Jacobian and residual terms at the boundary nodes to reflect the appropriate condition. The standard slip and no-slip wall boundary conditions are applied for inviscid and viscous solutions, respectively. The far field boundary condition is typically based on Riemann invariants. However, the Riemann far field boundary condition strictly enforces the condition that the velocity perturbations go to zero. This can lead to nonphysical solutions for rotors, which energize the flow causing the far wake velocity to exceed the freestream velocity. To remedy this situation a specified back pressure boundary condition can be used, since it does not restrict velocity. The back pressure far field enforces a pressure equal to a specified value. The typical condition for a rotor is that $p_{back} = p_\infty$, but in a wind tunnel experiment a different condition may be appropriate.

A comparison of the far field boundary conditions' influence on a hovering rotor solution is shown in Figure 4. In both cases the pressure discontinuity due to the actuator disk induces a downward velocity that propagates to the far field. In the Riemann approach the boundary condition forces the wake velocity to return to the freestream value, causing the wake energy to be converted into a nonphysical pressure rise at the far field boundary. In the back pressure boundary condition the pressure is specified to be equal to the freestream, which is consistent with the predicted solution prior to the far field.

2.3 Overset Grid Library

The Donor interpolation Receptor Transaction library (DiRTlib) [57] provides a solver independent library of overset routines. The generalized nature of this library enables it

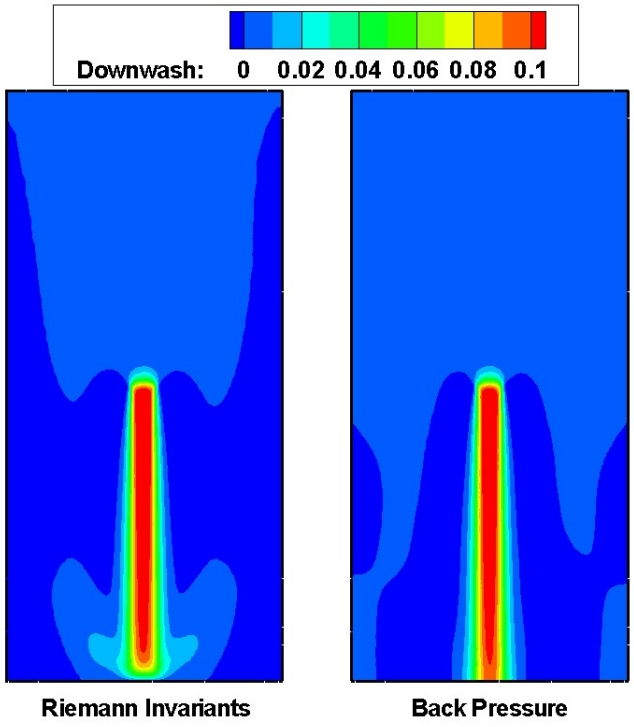

(a) Downwash Velocity

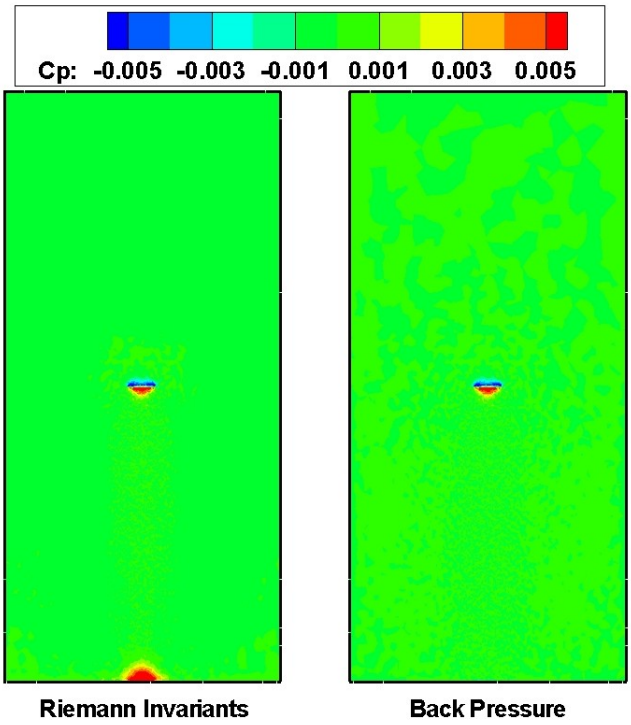

(b) Pressure Coefficient

Figure 4: Effect of the far field boundary condition on the wake solution of a hovering rotor.

to be easily incorporated into any type of flow solver (e.g. structured or unstructured, cell-centered scheme or node-based scheme, parallel or sequential, etc.). The solver interacts with the library through a variety of interface routines, but in this work they interact in primarily two ways.

The first process is an initialization routine, which allows the solver to exchange information with DiRTlib. A set of pointers are created to provide DiRTlib with the means to interact with the flow solver memory. During the initialization process, DiRTlib also reads and stores the connectivity information for the component grids. The grid connectivity consists of the node classification (in, out, fringe, or orphan) and the interpolation weights for the fringe nodes.

The other interaction between the solver and DiRTlib is during the solution process. At the beginning of each time step DiRTlib performs the interpolations between component grids and transmits the data to the appropriate fringe nodes. The fringe values are updated using a weighted average of the donor nodes from overlapping component grids. The solver then performs its standard update step to advance the solution. For time-accurate solutions the interpolation step must also be repeated at the beginning of each subiteration to ensure that the most accurate data available is being applied at the overset boundary.

2.4 Overset Grid Assembly

In order to utilize the overset capabilities incorporated into the flow solver via DiRTlib, a grid connectivity file is required. In this effort a Domain Connectivity Information (DCI) file is created using the Structured Unstructured Generalized Grid AssembleR (SUGGAR) [58]. The DCI file identifies grid nodes as in, out, fringe, or orphan and how to interpolate information across grids. The DCI file also contains data to allow a component grid to be translated, rotated, or scaled when creating the overset mesh.

SUGGAR marks grids nodes as in, out, fringe, or orphan by creating a variable resolution, cartesian approximation to the body surfaces. Nodes inside of the approximated body are marked as out and nodes outside of the body are marked as in. The nodes at the in/out boundary are marked as fringe nodes and indicate where the component grids should

transfer information. A double layer of fringe nodes is utilized by default to preserve the second order spatial accuracy of the flow solver. Figure 5 depicts a simple example of two overlapping structured grids.

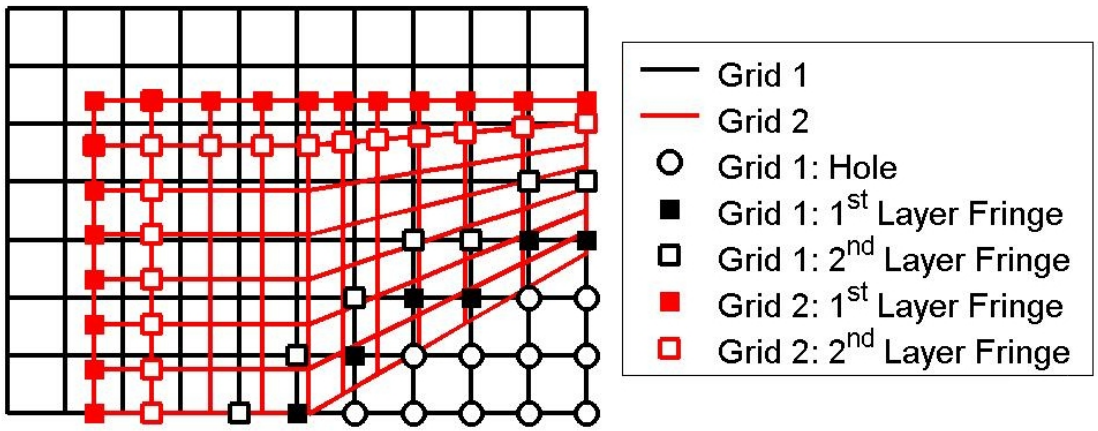

Figure 5: Overset mesh example, depicting in, out, and fringe nodes.

Orphan nodes are created when SUGGAR can not generate a satisfactory interpolation stencil for a node. Ideally the number of orphan nodes should be zero; however, they can be difficult to avoid in practice. A large number of orphan nodes typically indicates a significant difference in resolution between two overlapping grids. When an orphan node is encountered, the solver averages the values at the neighboring nodes to obtain a reasonable approximation of the flow variables.

To assemble a composite grid, the file names and orientations of the component grids are specified in an input file. For a static problem SUGGAR is run once, prior to the flow solver, to generate a composite grid and the DCI file. In a dynamic simulation, SUGGAR and the flow solver run in a coupled manner. SUGGAR generates a DCI file, which is read in by the flow solver at the beginning of a time step. The flow solver then performs the flow update for that step and writes out a new input file for SUGGAR and waits. SUGGAR takes the new input file and updates the DCI file for the next time step. Once SUGGAR completes its task, the flow solver takes over again and the process continues until the specified number of iterations is achieved.

2.5 Unstructured Grid Generator

Unstructured grids are generated using VGRIDns v3.5 [102, 103]. This process is completely automated once the user provides an input deck created with the GridTool v3.5 utility [104]. The first portion of the input deck requires creating a set of patches to define the geometry. Sources are then placed throughout the domain to specify the grid clustering. Once the density distribution is determined the input deck is written and the grid is generated.

VGRIDns generates the grid in four phases. The first phase determines the grid distribution on the boundary faces of the domain. If the viscous grid option is turned on, a series of advancing layers is then generated off of the viscous boundary surfaces (inviscid grids skip the advancing layers step). Spacing between the layers is specified by the following equation:

$$\Delta_n = \Delta_1 \left(1 + k_1 \left(1 + k_2\right)^{(n-1)}\right)^{(n-1)} \tag{20}$$

This results in a geometric progression based on the growth rate, k_1. The second rate, k_2, provides a means for accelerating the growth rate of the layers. The typical parameters used in this work are $\Delta_1 = 1.0x10^{-5}$, $k_1 = 0.15$, and $k_2 = 0.10$. These parameters were observed to yield y^+ values less than one for all of the configurations tested. The next phase fills in the remaining volume, using the advancing front technique. During the advancing front phase the grid fills in starting from the finest regions and progressing out to the coarser regions until no more tetrahedra can be generated. Typically a few holes are left over where the front closes in on itself. These holes are cleaned up during a final post-processing phase.

The majority of the grid generation time is spent during the setup of the input deck. Patch generation is relatively easy and can be achieved within a few hours (minutes for simple geometries), but source placement requires some thought and/or experience to obtain a good distribution. Once the input deck is set up, the grid is automatically generated by VGRIDns. The process typically requires two to three days to generate a complex grid on a PC. However, an experienced user could realistically start a complex configuration at

the beginning of the day and have an input deck ready for VGRIDns to generate the grid overnight.

2.6 Flow Visualization

Flow visualizations are generated using two commercial packages: Fieldview v10.0 [105, 106] and Tecplot v10.0 [107, 108]. Both programs provide excellent visualization capabilities and their associated formats have already been incorporated into the FUN3D post-processing utility. The state vector ($\vec{q}$) is the standard output from FUN3D, but a variety of derived quantities are also used in this work. The most common compressible derived quantities are shown below.

$$\begin{gathered} u = \frac{\rho u}{\rho} \\ p = (\gamma - 1)\left(E - \frac{\rho}{2}\left(u^2 + v^2 + w^2\right)\right) \\ C_p = 2\left(p - \frac{1}{\gamma}\right)\frac{1}{M_\infty^2} \end{gathered} \tag{21}$$

It is important to note that the velocity (u) and pressure (p) are not state vector variables and therefore must be extracted from the momentum (ρu) and energy (E) as shown. For incompressible solutions the velocity and pressure are standard outputs, but the pressure coefficient is computed slightly differently.

$$C_p = 2\,(p - 1) \tag{22}$$

Since the incompressible pressure is normalized by the freestream velocity rather than the speed of sounds, the Mach number is not present in the incompressible pressure coefficient computation. Hover creates a problem for the traditional pressure coefficient, since the freestream velocity is zero. Therefore, a modified pressure coefficient based on tip speed is frequently utilized. The modified pressure coefficient is related to the standard pressure coefficient as follows:

$$C_p^* = C_p \frac{\mu^2}{2} \tag{23}$$

where μ denotes the rotor advance ratio.

The vorticity is commonly used to visualize the rotor tip vortex. The vorticity is

computed from the curl of the velocity as shown below:

$$\vec{\omega} = \left(\frac{\partial w}{\partial y} - \frac{\partial v}{\partial z}\right)\hat{i} + \left(\frac{\partial u}{\partial z} - \frac{\partial w}{\partial x}\right)\hat{j} + \left(\frac{\partial v}{\partial x} - \frac{\partial u}{\partial y}\right)\hat{k} \tag{24}$$

Vorticity will typically be computed using the nondimensional velocity, so comparisons between compressible and incompressible solutions need to be scaled appropriately. Another way to visualize the tip vortex is with the Q criteria [109].

$$\begin{aligned} Q = \quad & \tfrac{1}{4}\left\|\vec{\omega}\right\|^2 - \left[\left(\tfrac{\partial u}{\partial x}\right)^2 + \left(\tfrac{\partial v}{\partial y}\right)^2 + \left(\tfrac{\partial w}{\partial z}\right)^2 + \tfrac{1}{2}\left(\tfrac{\partial u}{\partial y} + \tfrac{\partial v}{\partial x}\right)^2 + \right. \\ & \left. \tfrac{1}{2}\left(\tfrac{\partial u}{\partial z} + \tfrac{\partial w}{\partial x}\right)^2 + \tfrac{1}{2}\left(\tfrac{\partial w}{\partial y} + \tfrac{\partial v}{\partial z}\right)^2\right] \end{aligned} \tag{25}$$

The Q criteria was originally developed to identify vortex structures in turbulent boundary layer flows, since it is not possible to distinguish between turbulence and a vortex structure by plotting vorticity. The Q criteria simplifies vortex identification because $Q > 0$ indicates a vortex structure. A disadvantage of Q criteria based visualization is that it does not identify a vortex sheet structure.

CHAPTER III

ROTOR MODELING

3.1 Overview

Precise modeling of a helicopter rotor is difficult for a variety of reasons. The rotational motion of the blades with respect to the fuselage ensures that the aerodynamic problem is naturally unsteady. The blades may also be articulated to allow pitch, flap, and lag, adding additional degrees of freedom to the motion. Light weight, large aspect ratio rotor blades are typically flexible, which means that the blades can not be modeled as rigid bodies. While detailed modeling is desirable to capture the physics of the problem, it can quickly render the rotor aerodynamic problem intractable.

Through the use of judicious assumptions, the rotor problem can be simplified to allow for greater computational efficiency by sacrificing some accuracy. The list of assumptions utilized in this work are listed sequentially from least restrictive to most restrictive.

1. CFD can provide an accurate prediction of the flow.
2. The rotor blades can be modeled as rigid bodies.
3. The rotor blades can be modeled as infinitely thin surfaces.
4. The influence of the rotor can be time-averaged.

The first assumption is implied by the nature of the current work, but is essential to understand. Verification cases are presented in later sections to justify the first assumption. The rigid body assumption assumes that the blades do not deform. Technically this is an unrealistic assumption, but small deformations will have little influence on the flow over the blades. The test cases utilized herein were designed with highly rigid blades, so this assumption is reasonable. Application of the first two assumptions leads to the overset blade rotor model utilized in this work.

The third assumption is more restrictive than the previous two. By assuming that the blades are infinitely thin, the blade geometry is lost, meaning the blade loads are no longer based on first principles. With this assumption, the blade loading now needs to be provided through an approximate aerodynamic loading model. The actuator blade rotor model utilizes the first three assumptions and provides an unsteady simulation while reducing the computational cost by eliminating the nodes required to grid the rotor blades.

The final assumption states that a time-averaged representation of the flow is sufficient. Application of all four assumptions leads to an actuator disk representation of the rotor. The actuator disk approximation is convenient for obtaining rapid performance estimates, since steady-state computations are considerably faster and computationally less expensive than unsteady simulations.

The remaining sections describe the rotor models, beginning with the most simple (actuator disk) and ending with the overset rotor model.

3.2 Actuator Disk Model

The most basic method for modeling the influence of a helicopter rotor is through the use of an actuator disk. In this approach, the rotor is represented as an infinitely thin disk capable of sustaining a pressure discontinuity. The actuator disk is essentially a limiting case in which the number of blades goes to infinity. Since helicopters possess a finite number of blades, the actuator disk assumption provides a time-averaged representation of the flow. Although it is commonly used to simplify the rotor for basic analytical methods, the actuator disk has also been successfully utilized to simplify rotor modeling in Euler and RANS approaches [46, 48, 51, 50, 71]. The fundamental difference between a basic analysis and CFD approach is that CFD does not require an inflow assumption, since the inflow develops naturally as a part of the solution process.

In the literature, actuator disk implementations fall into two categories: a pressure jump boundary condition and a source term approach. A survey of these two approaches is presented by Le Chuiton [110]. The primary difference between the two categories is whether the rotor is included or removed from the global control volume. In the pressure

jump approach, the control volume is wrapped around the actuator disk in such a way that the actuator disk lies outside of the control volume. Conversely, in the source approach the actuator disk is present inside the control volume.

To demonstrate the differences between the pressure jump and source terms, consider the one-dimensional duct flow problem shown in Figure 6. In this example an actuator disk will be present between cells 2 and 3. A typical internal cell (i.e. without an actuator disk) will have the same flux on the left and right sides of the face shared by cells 2 and 3. The pressure jump method will update the state vector in the same fashion as the typical internal cell. However, the flux at the actuator disk face will no longer be the same on the left and right sides of the face. Instead, the fluxes are related by a proportionality condition, which in this case is the imposed actuator disk boundary condition. In the source term approach the fluxes are computed just as they were for a typical internal cell, but the update of the state vector is different. To make the presence of the actuator disk known to the flow solver an extra source term is added to the equation.

Naturally the pressure jump approach and the source term approach are similar, since they are both introducing the influence of the rotor. However, the implementation of each of these approaches differs significantly. This difference is particularly noticeable when the state vector is updated implicitly. Since the pressure jump approach depends on the state vector at cell 2 and 3, an implicit pressure jump approach will add diagonal and off-diagonal contributions to the Jacobian. The source approach only influences cell 3 so it only has a contribution on the diagonal.

3.2.1 Pressure Jump Boundary Condition Implementation

An actuator disk implemented through a pressure jump boundary condition is similar to other flow through boundary conditions (e.g. inflow / outflow). The difference is that the actuator disk boundary uses information from other internal flow cells rather than constant information from a reference condition. The dependence on other flow cells means that the actuator disk nodes will have both diagonal and off diagonal contributions in the Jacobian matrix. In a structured grid approach, it is straightforward to determine the two neighbors

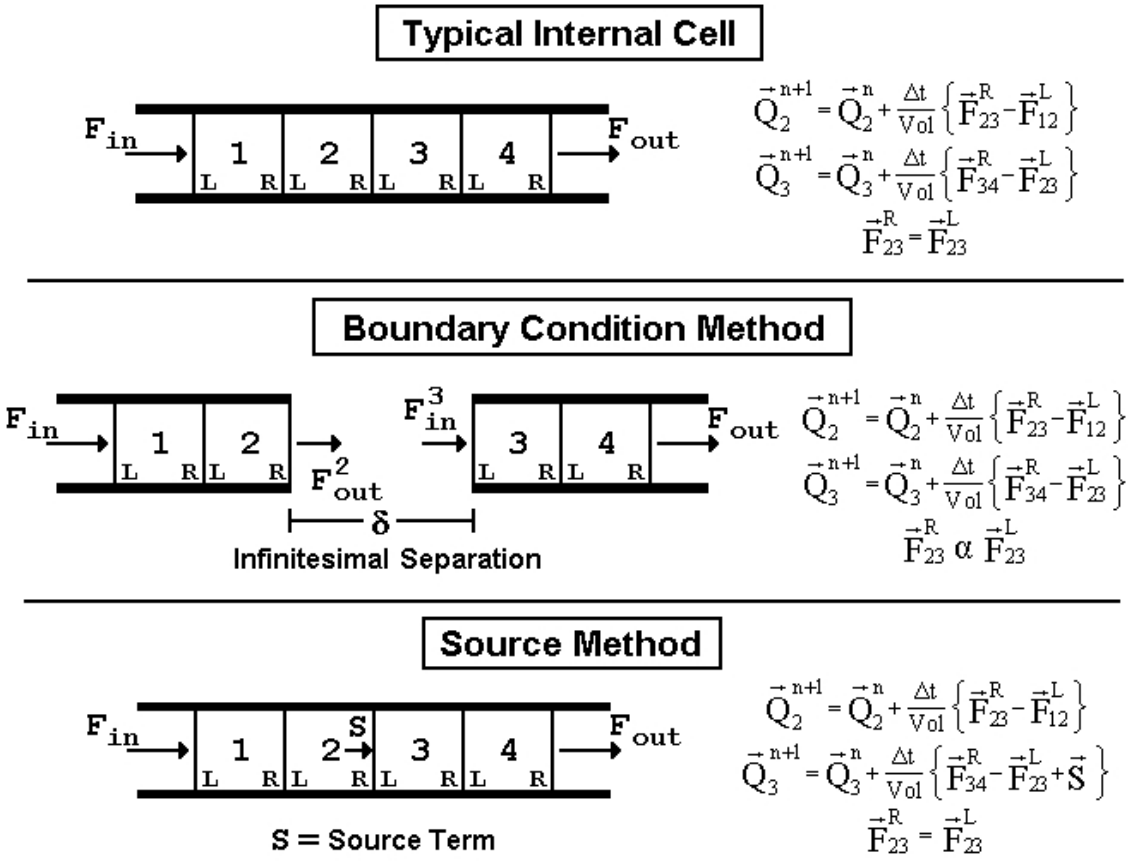

Figure 6: Flux calculation comparison for a one-dimensional duct flow problem.

who must exchange data. However, in an unstructured approach a node correspondence array is required.

For the purpose of this discussion the two sides of the pressure jump actuator disk boundary will be referred to as the upper surface (low pressure side) and lower surface (high pressure side). The first step is to determine the direction of the flow through the disk, since characteristic theory requires that four conditions (three for incompressible) are specified on the inflow side and one condition is specified on the outflow side. The flow direction, V_{norm}, is defined as positive when the flow is directed from the upper surface to the lower surface. In an explicit scheme the remaining conditions are interpolated from the grid interior. However, to be consistent with the FUN3D solver an implicit approach was applied, in which the remaining conditions develop naturally as part of the solution process.

In this work the actuator disk boundary conditions are based on the ones used by Fejtek and Roberts [48]. The first condition ensures that the mass flow is continuous though the disk. The second condition requires that two velocities tangential to the disk (V_{radial} and $V_{tangent}$) are continuous through the disk. Chaffin and Berry [50] introduced the rotor swirl by also adding a jump to $V_{tangent}$. However, they noted that the use of a swirl velocity jump could lead to nonphysical solutions, so this was not attempted in the current study. The final two conditions enforce the pressure jump across the disk and specify a condition on density. Fejtek and Roberts [48] specified that the inflow density was equal to the freestream density. However, a more general approach is to specify that the density is continuous through the disk. Enforcing the continuity of density was applied in the present work. The conditions are summarized in Table 2. In an incompressible approach the density condition is not utilized since the continuity of density is assumed.

The implicit treatment of the actuator disk proved to be a computationally intensive task. This is due to the fact that the governing equation at any actuator disk node depends on both itself and the node on the opposite surface. To simplify the method, the off diagonal contribution was neglected. As a result the flow variables on the actuator disk boundary had a tendency to diverge from one another. To maintain the desired continuity

Table 2: Boundary Condition Enforcement

	Upper Surface	Lower Surface
$V_{norm} \geq 0$	$(\rho V_{norm})_{upper} = (\rho V_{norm})_{lower}$	$p_{lower} = p_{upper} + \Delta p_{rotor}$ $\rho_{lower} = \rho_{upper}$ $V_{tan,lower} = V_{tan,upper}$ $V_{rad,lower} = V_{rad,upper}$
$V_{norm} < 0$	$p_{upper} = p_{lower} - \Delta p_{rotor}$ $\rho_{upper} = \rho_{lower}$ $V_{tan,upper} = V_{tan,lower}$ $V_{rad,upper} = V_{rad,lower}$	$(\rho V_{norm})_{lower} = (\rho V_{norm})_{upper}$

a balancing step, mirroring the boundary condition enforcement, was added after the state vector update. The drawback to this balancing is that it added some explicit nature to the solution process. Another drawback that was discovered in formulating the pressure jump boundary condition approach is that an incompressible formulation that was robust for all of the test cases was never achieved. This resulted in a limitation of the approach for incompressible methodologies, which was deemed unacceptable for rotorcraft fuselage aerodynamics.

3.2.2 Source Implementation

The source term actuator disk model was originally proposed by Rajagopalan and Fanucci [44] for the analysis of vertical axis wind turbines and later extended to helicopter rotors [45, 46]. Since source terms are fairly general, two approaches can be utilized to introduce the sources into the computational domain. In one approach the actuator disk surface is defined in the computational grid as the boundary between two sets of cells, allowing both the source method and the boundary condition method to be applied to the same grid. A more generalized approach is to allow the actuator disk to be arbitrarily inserted into the computational grid. Arbitrary insertion of the actuator disk simplifies grid generation, since the disk surface does not need to be incorporated into the grid. Another benefit of the arbitrary approach is that a single grid can be utilized for a variety of disk orientations. With a grid fixed approach a new grid would need to be generated for each orientation of the disk. Since the ideal for unstructured methods is to reduce the grid

generation time, the arbitrary insertion method is well suited for unstructured methods and was the avenue pursued in this research.

In the perfect case, the computational element should feel a force proportional to the area of the actuator disk that intersects the cell. However, in a node-based unstructured method each cell has an arbitrary polyhedral shape, making the determination of the exact area of intersection a non-trivial computational task. An alternative approach is to use a discrete approximation as depicted in Figure 7 where sources do not intersect identically with the unstructured grid cells. The advantage of using a discrete approximation is that the source elements can be defined using a simple structured grid approach as shown in Figure 8.

With either the discrete or exact model the sources do not influence the spatial accuracy of the CFD solution scheme. However, the accuracy of the rotor solution is dependent on the distribution of the sources. The disadvantage of the discrete approach is that an increased number of sources are required to obtain the same accuracy as an exact area computation. If the source grid is coarser than the computational grid the rotor influence is no longer smoothly distributed, which introduces non-physical vorticity into the flow as shown in Figure 9. In this figure the view has been tilted to show the correlation between the actuator disk source grid and the vortex pairs generated in the plane normal to the disk. Since the actuator disk is an approximation of the true rotor behavior, the additional error introduced by the discrete approximation is assumed be negligible.

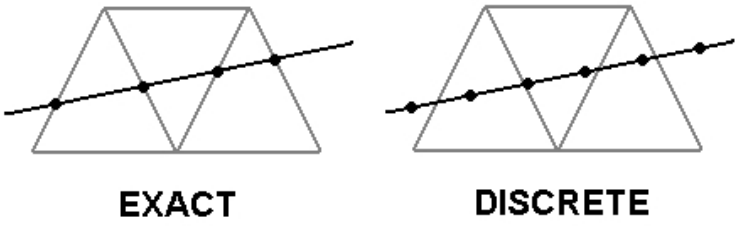

Figure 7: Comparison of exact intersections versus a discretized approximation.

The source term is equal to blade loading acting on a given actuator disk element or the work done by the blade load. The blade loads can be obtained in a variety of ways,

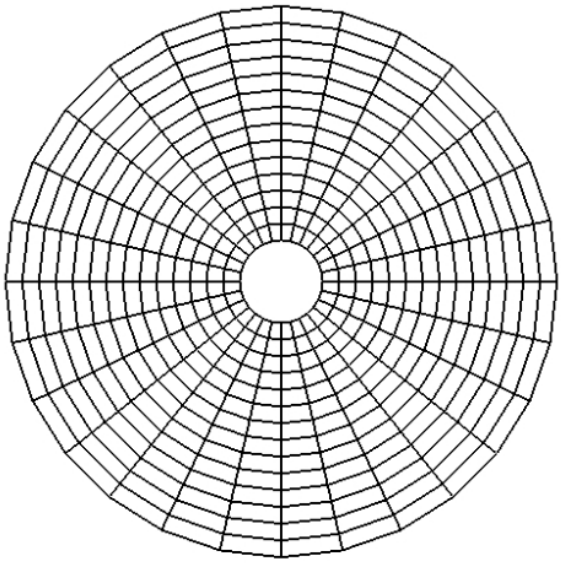

Figure 8: Source elements on an actuator disk.

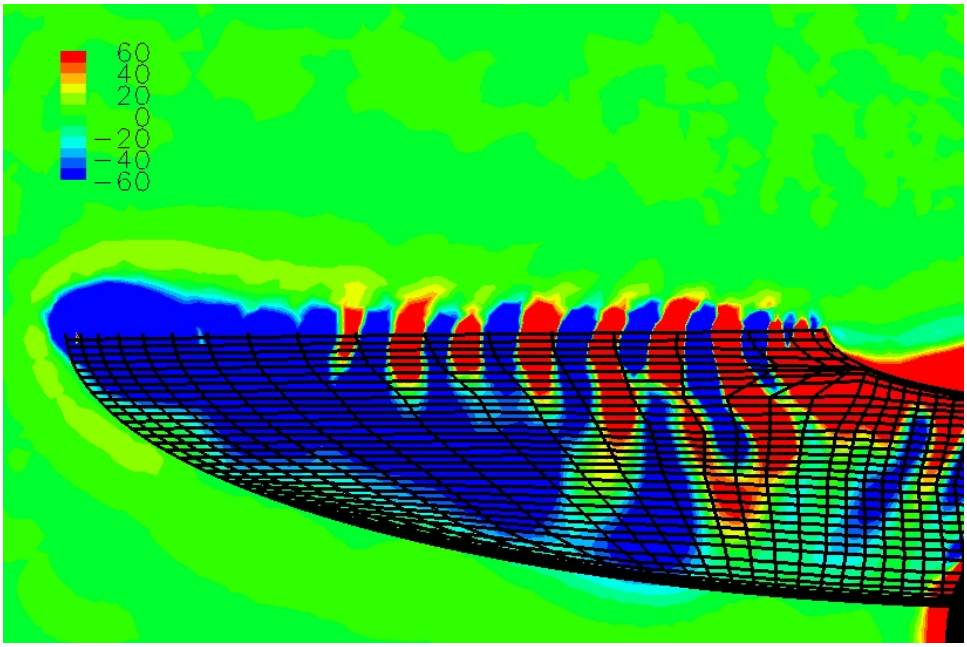

Figure 9: Non-physical vorticity contours generated in a plane normal to a coarse actuator disk source grid.

but all loading models fall into two categories based on whether they depend on the CFD solution or are independent of it. The independent or fixed distribution is simple to apply since the force is not coupled to the flow solution. The contribution to the compressible governing equations for a fixed distribution are:

$$RHS = RHS + \begin{bmatrix} 0 \\ f_x \\ f_y \\ f_z \\ \vec{f} \bullet \vec{V} \end{bmatrix} \quad LHS = LHS + \begin{bmatrix} 0 & 0 & 0 & 0 & 0 \\ 0 & 0 & 0 & 0 & 0 \\ 0 & 0 & 0 & 0 & 0 \\ 0 & 0 & 0 & 0 & 0 \\ -\vec{f} \bullet \frac{\vec{V}}{\rho} & \frac{f_x}{\rho} & \frac{f_y}{\rho} & \frac{f_z}{\rho} & 0 \end{bmatrix} \tag{26}$$

Since the incompressible formulation does not require the solution of the energy equation, incompressible source contributions become even simpler.

$$RHS = RHS + \begin{bmatrix} 0 \\ f_x \\ f_y \\ f_z \end{bmatrix} \quad LHS = LHS + \begin{bmatrix} 0 & 0 & 0 & 0 \\ 0 & 0 & 0 & 0 \\ 0 & 0 & 0 & 0 \\ 0 & 0 & 0 & 0 \end{bmatrix} \tag{27}$$

An interesting feature of a fixed distribution when incompressible flow is assumed is that the sources do not contribute anything to the Jacobian, but the actuator disk method remains fully implicit.

Although a fixed distribution is convenient, it may lack the physical realism obtained from coupling the force computation to the flow. The variable distribution methods do not require additional terms on the right hand side of the equation, but the Jacobian matrix will become more populated. The compressible contribution to the Jacobian for a coupled force distribution is:

$$LHS = LHS + \begin{bmatrix} 0 & 0 & 0 & 0 & 0 \\ \frac{\partial f_x}{\partial \rho} & \frac{\partial f_x}{\partial (\rho u)} & \frac{\partial f_x}{\partial (\rho v)} & \frac{\partial f_x}{\partial (\rho w)} & 0 \\ \frac{\partial f_y}{\partial \rho} & \frac{\partial f_y}{\partial (\rho u)} & \frac{\partial f_y}{\partial (\rho v)} & \frac{\partial f_y}{\partial (\rho w)} & 0 \\ \frac{\partial f_z}{\partial \rho} & \frac{\partial f_z}{\partial (\rho u)} & \frac{\partial f_z}{\partial (\rho v)} & \frac{\partial f_z}{\partial (\rho w)} & 0 \\ \frac{\partial \vec{f}}{\partial \rho} \bullet \vec{V} - \vec{f} \bullet \frac{\vec{V}}{\rho} & \frac{\partial \vec{f}}{\partial (\rho u)} \bullet \vec{V} + \frac{f_x}{\rho} & \frac{\partial \vec{f}}{\partial (\rho v)} \bullet \vec{V} + \frac{f_y}{\rho} & \frac{\partial \vec{f}}{\partial (\rho w)} \bullet \vec{V} + \frac{f_z}{\rho} & 0 \end{bmatrix} \tag{28}$$

The fixed distribution terms are still present, but additional terms have appeared to represent the dependence of the force on the flow variables. The incompressible contribution to the Jacobian is

$$LHS = LHS + \begin{bmatrix} 0 & 0 & 0 & 0 \\ 0 & \frac{\partial f_x}{\partial u} & \frac{\partial f_x}{\partial v} & \frac{\partial f_x}{\partial w} \\ 0 & \frac{\partial f_y}{\partial u} & \frac{\partial f_y}{\partial v} & \frac{\partial f_y}{\partial w} \\ 0 & \frac{\partial f_z}{\partial u} & \frac{\partial f_z}{\partial v} & \frac{\partial f_z}{\partial w} \end{bmatrix} \tag{29}$$

Once again the incompressible contribution is simpler than the compressible one, but the Jacobian contribution is no longer zero. If the Jacobian contributions for the variable solution are ignored, the actuator disk method becomes explicit and the flow solver loses considerable stability.

The advantages of the source approach over the boundary condition strategy for an unstructured method are summarized below:

1. Grid independent rotor definition
2. Simple implicit formulation
3. Incompressible actuator disk requires no Jacobian terms for a fixed loading

The disadvantage of the current source approach results from the discrete element approximation.

3.3 Actuator Blade Model

The actuator blade model is similar to an actuator disk model, but rather than distribute the load over a disk, the loads are distributed over the blade planform as shown in Figure 10. The actuator blade model is a more generalized version of the unsteady actuator disk models of Boyd [53] or Tadghighi [55]. Their unsteady actuator disk models use a disk surface and distribute the loading along a radial line, zeroing out the load at the other disk points. These implementations are similar to having a lifting-line representation replace each rotor blade. Unlike these models, the actuator blade model distributes the loading

along both the blade radius and chord. In the limit where the number of chordwise elements is set to one the actuator blade model becomes equivalent to the unsteady actuator disk.

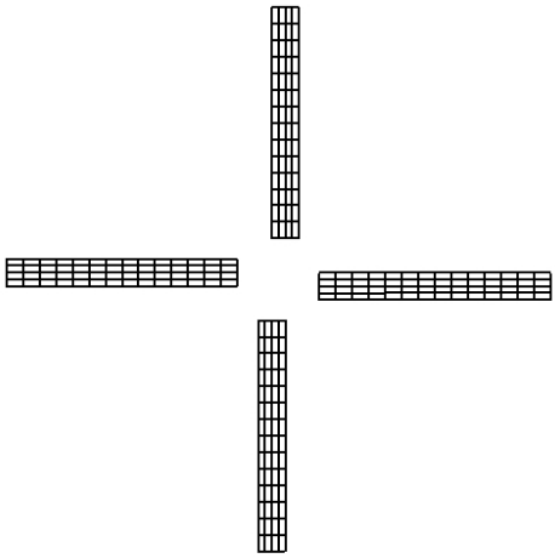

Figure 10: Source elements on the actuator blades.

Because the location of the blade planforms changes after each iteration the actuator blade model can not be modeled through a boundary condition. Therefore, the actuator blade model is applied through the use of source terms. The implementation of the actuator blade source terms into the flow solver is identical to the actuator disk source terms just described. The primary difference between the actuator disk and the actuator blade model is in the computation of the blade loads.

3.4 Aerodynamic Loading Models

The aerodynamic blade loading is a critical element of the actuator disk and actuator blade rotor models. Neither of these methods physically model the blade geometry, so the influence of the rotor is approximated implicitly through the blade loading model. In this effort four blade load models were considered: user specified, uniform, linearly increasing, and blade element theory.

The first three methods utilize a fixed load distribution. This significantly simplifies the approach, since the load can be determined once and then reapplied during successive

iterations. For the fixed sources the contribution to the left and right hand sides of the governing equations were shown in Equations 26 and 27. The blade element theory utilizes the local flow velocities provided by the solver to compute the blade forces. Coupling the blade forces to the flow variables increases the fidelity of the model, but adds additional terms to the Jacobian as shown in Equation 28 and 29.

3.4.1 User Specified Model

The user specified loading allows the user to provide the solver with an input file containing all of the blade loads at each source location. This method is convenient for utilizing the blade loads computed by an alternate analysis such as a comprehensive code. This approach was utilized in Renaud, et al. [111] to compare a nonuniform loading among three partners for the Dauphin configuration.

3.4.2 Algebraic Models

The uniform and linearly increasing distributions are simple algebraic models that are fully determined by the rotor thrust. The uniform distribution assumes that the load is constant along the radius of the blade as shown in Figure 11. The linear distribution assumes that the load linearly increases from zero at the center of the disk to a maximum value at the blade tip as shown in Figure 12. Both models assume that the blade loading is not a function of the azimuth angle. Since the areas of the actuator disk elements are not necessarily constant, the blade loading is written in terms of the force per unit area (pressure).

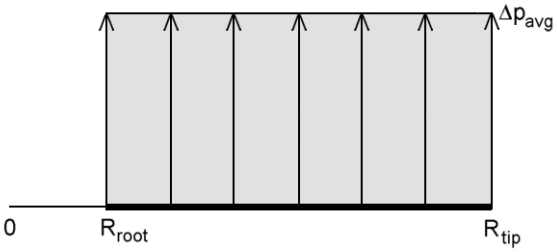

Figure 11: Blade loading with the uniform pressure distribution.

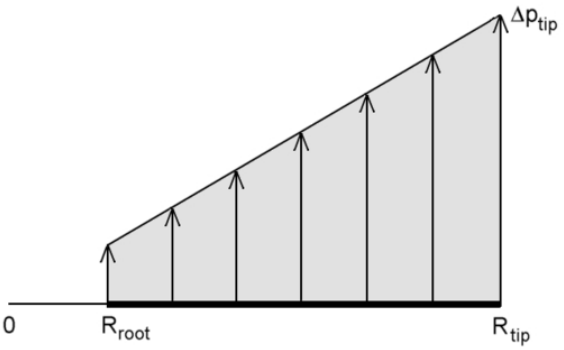

Figure 12: Blade loading with the linearly varying pressure distribution.

The rotor thrust is input into the algebraic models in terms of a rotor thrust coefficient.

$$C_T = \frac{\overline{T}}{\overline{\rho}_{ref}\pi\overline{R}^2\left(\overline{\Omega R}\right)^2} \tag{30}$$

Since the solver nondimensionalizes forces by $\overline{\rho}_{ref}\overline{V}_{ref}^2\overline{L}_{ref}^2$, the nondimensional thrust is related to the thrust coefficient as follows:

$$T = \frac{\overline{T}}{\overline{\rho}_{ref}\overline{V}_{ref}^2\overline{L}_{ref}^2} = \pi\frac{\overline{\rho}_{ref}}{\overline{\rho}_{ref}}\left(\frac{\overline{R}}{\overline{L}_{ref}}\right)^2\left(\frac{\overline{\Omega R}}{\overline{V}_{ref}}\right)^2 C_T = \pi R^2 V_{tip}^2 C_T \tag{31}$$

The blade cutout region is accounted for by dividing the nondimensional thrust by the nondimensional lifting area.

For the actuator disk model the nondimensional disk loading is:

$$\Delta p_{avg} = \frac{R^2}{\left(R^2 - R_{root}^2\right)} V_{tip}^2 C_T \tag{32}$$

If the cutout region is set to zero the uniform pressure simplifies to the thrust coefficient times the nondimensional tip speed. For the actuator blade model the nondimensional blade loading is

$$\Delta p_{avg} = \frac{\pi R}{N_{blade} c}\left(\frac{R}{R - R_{root}}\right) V_{tip}^2 C_T = \frac{R}{\sigma\left(R - R_{root}\right)} V_{tip}^2 C_T \tag{33}$$

In the limiting case where the blade cutout goes to zero the actuator blade loading is equal to the actuator disk loading divided by the rotor solidity.

The linearly increasing load can be defined as a function of the the blade radial station.

$$\Delta p\left(r\right) = \Delta p_{tip}\frac{r}{R} \tag{34}$$

For the actuator disk model the tip loading can be related to the average loading by integrating over the surface of the disk and enforcing that the thrust is equal for both models.

$$2\pi \int_{R_{root}}^{R} \Delta p_{avg} r dr = 2\pi \int_{R_{root}}^{R} \Delta p_{tip} \frac{r}{R} r dr \tag{35}$$

This results in the following relation:

$$\Delta p_{tip} = \frac{3}{2} \Delta p_{avg} \frac{R\left(R^2 - R_{root}^2\right)}{\left(R^3 - R_{root}^3\right)} \tag{36}$$

In the limiting case where R_{root} is zero the tip loading is equal to three halves the average load.

A similar process holds for the actuator blade model, but instead of integrating over the disk the loading is integrated over the length of the blade.

$$N_{blade} \int_{R_{root}}^{R} \Delta p_{avg} dr = N_{blade} \int_{R_{root}}^{R} \Delta p_{tip} \frac{r}{R} dr \tag{37}$$

Integrating this expression leads to the following result:

$$\Delta p_{tip} = 2\Delta p_{avg} \frac{R}{(R - R_{root})} \tag{38}$$

In the limit of $R_{root} = 0$, the tip load will be twice the average blade loading.

3.4.3 Blade Element Theory Model

The blade element distribution follows the approach outlined in Zori, et al. [46]. The flow solver provides the components of the local flow velocity (u, v, w) in terms of the grid coordinate system. The velocities are reoriented into a blade aligned coordinate system through a series of successive transformations. In general the blade motions can occur in any order, but in this work they are assumed to occur in a specific order: lag, flap, then pitch.

The first transform reorients the velocities with respect to the rotor shaft aligned system, which is defined by the 1-2-3 set of Euler angles.

$$\begin{pmatrix} u_s \\ v_s \\ w_s \end{pmatrix} = \begin{bmatrix} C_{\phi_2} C_{\phi_3} & C_{\phi_1} S_{\phi_3} + S_{\phi_1} S_{\phi_2} C_{\phi_3} & S_{\phi_1} S_{\phi_3} - C_{\phi_1} S_{\phi_2} C_{\phi_3} \\ -C_{\phi_2} S_{\phi_3} & C_{\phi_1} C_{\phi_3} - S_{\phi_1} S_{\phi_2} S_{\phi_3} & S_{\phi_1} C_{\phi_3} + C_{\phi_1} S_{\phi_2} S_{\phi_3} \\ S_{\phi_2} & -S_{\phi_1} C_{\phi_2} & C_{\phi_1} C_{\phi_2} \end{bmatrix} \begin{pmatrix} u \\ v \\ w \end{pmatrix} \tag{39}$$

The shaft system velocity, $\vec{V}_s$, is then rotated to the appropriate azimuth angle.

$$\begin{pmatrix} u_\psi \\ v_\psi \\ w_\psi \end{pmatrix} = \begin{bmatrix} C_\psi & \frac{\Omega}{|\Omega|}S_\psi & 0 \\ -\frac{\Omega}{|\Omega|}S_\psi & C_\psi & 0 \\ 0 & 0 & 1 \end{bmatrix} \begin{pmatrix} u_s \\ v_s \\ w_s \end{pmatrix} \tag{40}$$

A sign operator ($\frac{\Omega}{|\Omega|}$) is applied in front of the sine functions to account for either clockwise or counterclockwise rotation. The rotor angular velocity (ω) is defined to be positive for counter-clockwise rotation when viewed from above. The lead-lag angle transform is defined as:

$$\begin{pmatrix} u_\delta \\ v_\delta \\ w_\delta \end{pmatrix} = \begin{bmatrix} C_\delta & -\frac{\Omega}{|\Omega|}S_\delta & 0 \\ \frac{\Omega}{|\Omega|}S_\delta & C_\delta & 0 \\ 0 & 0 & 1 \end{bmatrix} \begin{pmatrix} u_\psi \\ v_\psi \\ w_\psi \end{pmatrix} \tag{41}$$

where the lead-lag angle (δ) is positive for lag. Since the azimuth and lead-lag angle transforms occur about the same axis, they have been combined into a single operation.

$$\begin{pmatrix} u_\delta \\ v_\delta \\ w_\delta \end{pmatrix} = \begin{bmatrix} C_{(\psi-\delta)} & \frac{\Omega}{|\Omega|}S_{(\psi-\delta)} & 0 \\ -\frac{\Omega}{|\Omega|}S_{(\psi-\delta)} & C_{(\psi-\delta)} & 0 \\ 0 & 0 & 1 \end{bmatrix} \begin{pmatrix} u_s \\ v_s \\ w_s \end{pmatrix} \tag{42}$$

The next transformation in the sequence occurs about the flap angle, β.

$$\begin{pmatrix} u_\beta \\ v_\beta \\ w_\beta \end{pmatrix} = \begin{bmatrix} C_\beta & 0 & S_\beta \\ 0 & 1 & 0 \\ -S_\beta & 0 & C_\beta \end{bmatrix} \begin{pmatrix} u_\delta \\ v_\delta \\ w_\delta \end{pmatrix} \tag{43}$$

No further transformations are required, since the blade pitch angle is accounted for in the blade element theory. It is important to note that the assumed order of transformations allowed for two simplifications that would not be possible if a generic set of transforms was used. In a generic sense the azimuth and lead-lag transforms could not be combined and an additional transform would be required to account for pitch.

The flow velocity provided by the solver represents the velocity induced by the rotor. To compute the effective angle of attack for the blade section the velocity due to the blade motion must also be included. The rotational motion is especially important, since the tip

velocity is much larger than the induced velocity. Other velocity components due to flap and lead-lag can also be significant.

The velocity due to the blade rotation is specified as Ωr. The contribution due to flap is $\dot{\beta} r$ and lead-lag is $\dot{\delta} r$. The velocities normal and tangent to the blade are now specified as

$$\begin{aligned} V_{norm} &= -v_\beta + \dot{\beta} r \\ V_{tan} &= -\frac{\Omega}{|\Omega|} v_\beta + \Omega r - \dot{\delta} r \\ V_{total} &= \sqrt{V_{norm}^2 + V_{tan}^2} \end{aligned} \tag{44}$$

Figure 13 shows the positive orientation of the normal and tangent vectors along with the unit vectors in the flap frame. The only difference between clockwise and counter-clockwise blade rotation is that the i_2 axis is reversed.

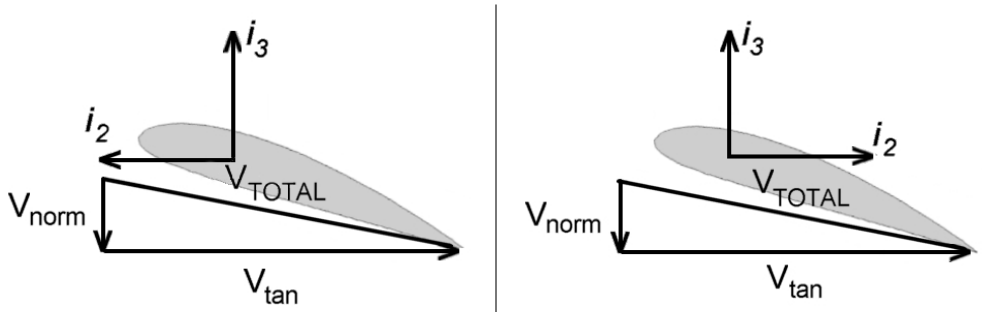

Counter-clockwise Rotation, $\Omega \geq 0$ | Clockwise Rotation $\Omega < 0$

Figure 13: Velocity orientation in the blade element model.

The inflow angle is computed from the normal and tangential velocities as follows

$$\phi = \arctan\left(\frac{V_{norm}}{V_{tan}}\right) \tag{45}$$

The blade pitch is determined from the blade twist, collective, and cyclic pitch angles.

$$\theta(r, \psi) = \theta_0 + \frac{r}{R}\theta_{twist} + \theta_{1C}\cos(\psi) + \theta_{1S}\sin(\psi) \tag{46}$$

The effective angle of attack is then found.

$$\alpha = \theta - \phi \tag{47}$$

With the effective angle of attack known, there is sufficient information to proceed to the determination of the lift and drag.

The sectional lift and drag model is based on a quasi-steady approximation in which the angle of attack fully determines the lift and drag. The algebraic model uses a set of user defined coefficients to compute the blade loads. The lift coefficient uses C_{ℓ_α} and α_0. The drag coefficient uses C_{d0}, C_{d1}, and C_{d2}. Limits are applied to ensure that the coefficients do not not exceed realistic limits. Since rotor blades have the potential to experience very large angles of attack, the algebraic model is defined over the range $-\pi < \alpha \leq \pi$ by assuming that the lift and drag behave the same at π as they do at 0. The lift coefficient is defined as follows

$$C_\ell = \begin{cases} C_{\ell_\alpha}(\alpha - \alpha_0) & \alpha_{min} \leq \alpha \leq \alpha_{max} \\ C_{\ell_\alpha}(\alpha - \pi - \alpha_0) & \alpha_{min} + \pi \leq \alpha \leq \pi \\ C_{\ell_\alpha}(\alpha + \pi - \alpha_0) & -\pi < \alpha \leq \alpha_{max} - \pi \\ C_{\ell_\alpha,stall}(\alpha - \alpha_0) & \alpha_{max} < \alpha < \pi + \alpha_{min} \\ C_{\ell_\alpha,stall}(\alpha - \alpha_0) & \alpha_{max} - \pi < \alpha < \alpha_{min} \end{cases} \tag{48}$$

where

$$\begin{aligned} \alpha_{max} &= \frac{C_{\ell,max}}{C_{\ell_\alpha}} + \alpha_0 \\ \alpha_{min} &= \frac{C_{\ell,min}}{C_{\ell_\alpha}} + \alpha_0 \\ C_{\ell_\alpha,stall} &= \frac{C_{\ell,max} - C_{\ell,min}}{\alpha_{max} - \alpha_{min} - \pi} \end{aligned} \tag{49}$$

The drag coefficient model is

$$C_d = \begin{cases} C_{d0} + C_{d1}\alpha + C_{d2}\alpha & -\frac{\pi}{2} \leq \alpha \leq \frac{\pi}{2} \\ C_{d0} + C_{d1}(\alpha - \pi) + C_{d2}(\alpha - \pi)^2 & \alpha > \frac{\pi}{2} \\ C_{d0} + C_{d1}(\alpha + \pi) + C_{d2}(\alpha + \pi)^2 & \alpha < -\frac{\pi}{2} \end{cases} \tag{50}$$

Since the drag model can increase very rapidly due to the squared terms, the limiters are used to enforce that the drag does not exceed reasonable bounds.

$$C_d = \begin{cases} C_{min} & C_d < C_{d,min} \\ C_{max} & C_d > C_{d,max} \end{cases} \tag{51}$$

In general, setting the maximum is more important than the minimum, but use of the minimum can be useful to obtain better overall fits. A sample loading distribution using this approach is shown in Figure 14.

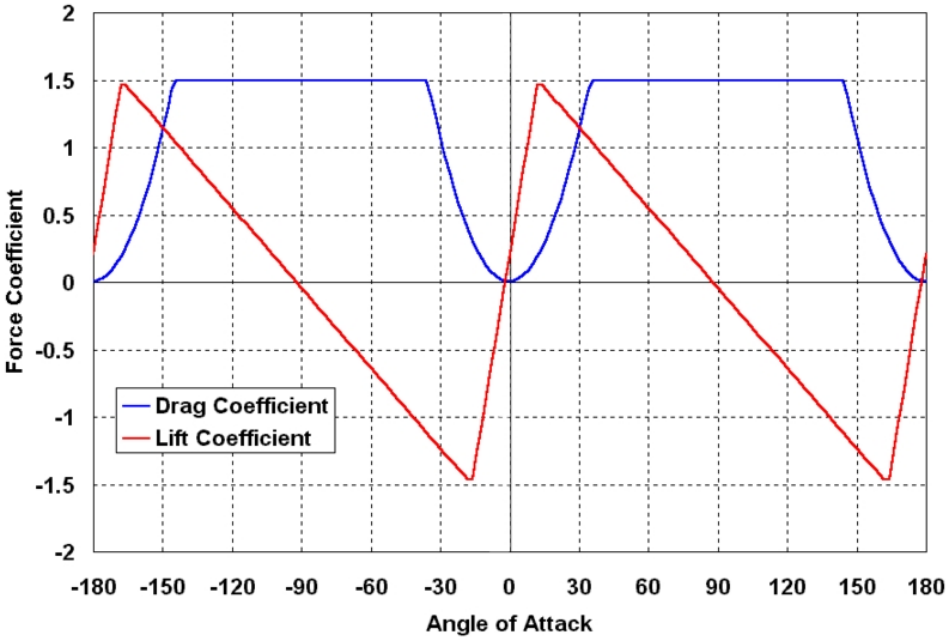

Figure 14: Algebraic force coefficient example for the blade element model.

The sectional lift and drag forces are now computed as

$$\begin{aligned} \Delta L &= C_\ell \rho V_{total}^2 c \Delta r \\ \Delta D &= C_d \rho V_{total}^2 c \Delta r \end{aligned} \tag{52}$$

In the actuator disk model the forces are then time averaged by considering that the blade only spends a fraction of the time at any point on the disk.

$$\begin{aligned} \Delta L_{disk} &= \Delta L \frac{N_{blades} \Delta\psi}{2\pi} \\ \Delta D_{disk} &= \Delta D \frac{N_{blades} \Delta\psi}{2\pi} \end{aligned} \tag{53}$$

For the actuator blade method the force is distributed over the chord. In the current effort a uniform chordwise distribution is assumed, so the force is divided by the number of chordwise sections.

$$\begin{aligned} \Delta L_{blade} &= \Delta L \frac{1}{N_{chord}} \\ \Delta D_{blade} &= \Delta D \frac{1}{N_{chord}} \end{aligned} \tag{54}$$

The final step is to rotate out of the wind aligned system and into the flap reference frame.

$$\begin{pmatrix} f_{1,\beta} \\ f_{2,\beta} \\ f_{3,\beta} \end{pmatrix} = \begin{pmatrix} 0 \\ -\frac{\Omega}{|\Omega|} \left(\Delta L \sin\left(\phi\right) + \Delta D \cos\left(\phi\right) \right) \\ \Delta L \cos\left(\phi\right) - \Delta D \sin\left(\phi\right) \end{pmatrix} \tag{55}$$

The blade forces are then transformed back into the grid aligned coordinate system by multiplying by the transpose of the transforms shown in Equations 43, 42, and 39 in that order.

3.5 Overset Rotor Blades

The implementation of overset rotor blades is achieved using DiRTlib and SUGGAR. The strategy for developing the overset unstructured grids is to incorporate all of the the stationary features into a single grid and create an additional grid for each dynamic component. The ROBIN configuration shown in Figure 15 provides a good example of this strategy. The fuselage, rotor shaft, and fuselage strut form the first grid that extends from the fuselage to the far field. The dynamic components (i.e. the four rotor blades) are individually modeled with an additional grid, which extends a few chord lengths away from the blade. It should also be noted that the rotor blades for this configuration are identical and can be duplicated for the overset grid, so the user is only needs to create the static grid and a single blade grid.

The DiRTlib overset library handles the majority of the implementation, but a few comments need to be mentioned here. The ideal approach for incorporating the blade motion is to use a six degree-of-freedom (6DOF) solver in which the rotor blades move based on a combination of control inputs and the applied loading. The 6DOF capability is being implemented separately from this effort as the test cases herein utilize prescribed blade motions.

The initial FUN3D grid motion implementation [100] allowed for constant or sinusoidal rotation about a single axis. This is sufficient for the blade rotation about the rotor shaft, but does not accommodate additional motions due to pitch, flap, and lead-lag. Since these rotations are necessary to capture the physics of the rotor blade motions, the initial implementation was modified to include the additional rotations.

The basic implementation uses a standard rotation of $\Delta\psi$ about the rotation axis $\hat{n}$ that brings a point from is current location $\vec{X}_{old}$ to the new position $\vec{X}_{new}$.

$$\vec{X}_{new} = \mathbf{R}_{\Delta\psi}\left(\vec{X}_{old} - \vec{X}_0\right) + \vec{X}_0 + \Delta\vec{X} \tag{56}$$

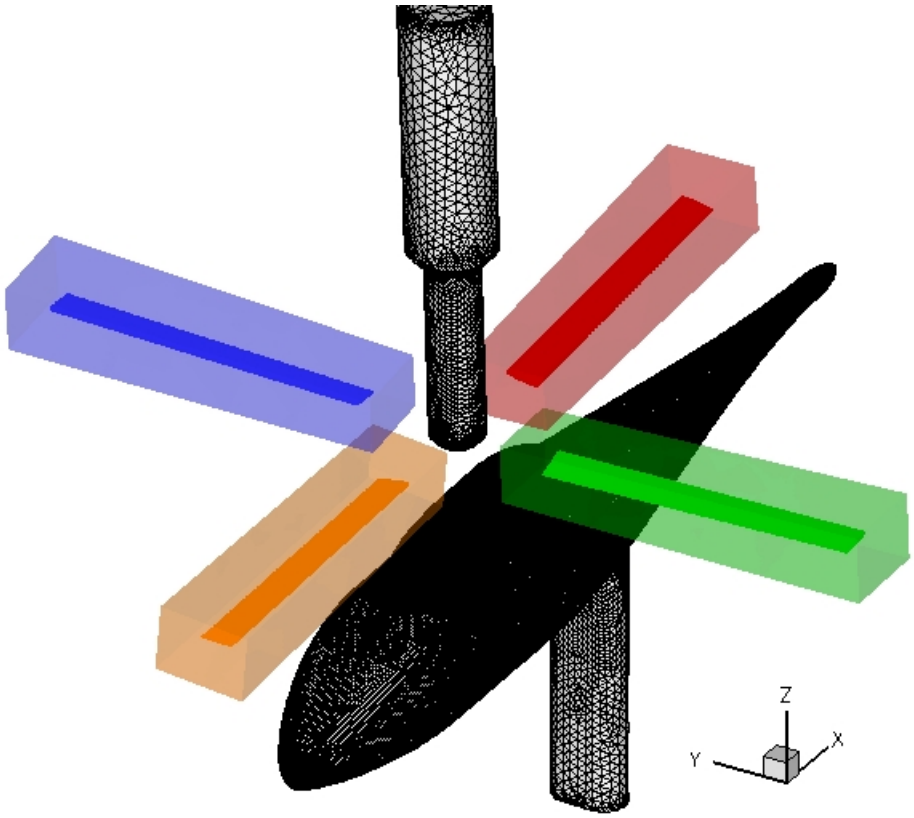

Figure 15: The five overset grids for modeling the ROBIN configuration.

The center of rotation is denoted as $\vec{X}_0$ and the contribution due to translation is $\Delta\vec{X}$. The rotation tensor is shown below.

$$\mathbf{R}_{\Delta\psi} = \begin{bmatrix} \left(1 - C_{\Delta\psi}\right) n_x^2 + C_{\Delta\psi} & \left(1 - C_{\Delta\psi}\right) n_x n_y - S_{\Delta\psi} n_z & \left(1 - C_{\Delta\psi}\right) n_x n_z + S_{\Delta\psi} n_y \\ \left(1 - C_{\Delta\psi}\right) n_y n_x + S_{\Delta\psi} n_z & \left(1 - C_{\Delta\psi}\right) n_y^2 + C_{\Delta\psi} & \left(1 - C_{\Delta\psi}\right) n_y n_z - S_{\Delta\psi} n_x \\ \left(1 - C_{\Delta\psi}\right) n_z n_x - S_{\Delta\psi} n_y & \left(1 - C_{\Delta\psi}\right) n_z n_y + S_{\Delta\psi} n_x & \left(1 - C_{\Delta\psi}\right) n_z^2 + C_{\Delta\psi} \end{bmatrix} \tag{57}$$

To simplify the incorporation of the additional rotations, $\vec{X}_0$ was also assumed to be the center of rotation for pitch, flap, and lead-lag. This allows for the extra rotations to be incorporated with minimal changes to Equation 56, resulting in the following equation

$$\vec{X}_{new} = \mathbf{R}_{\theta_{new}} \mathbf{R}_{\beta_{new}} \mathbf{R}_{\delta_{new}} \mathbf{R}_{\Delta\psi} \mathbf{R}_{\delta_{old}}^T \mathbf{R}_{\beta_{old}}^T \mathbf{R}_{\theta_{old}}^T \left(\vec{X}_{old} - \vec{X}_0\right) + \vec{X}_0 + \Delta\vec{X} \tag{58}$$

The basic strategy is to take the current blade and rotate it back to the reference position at the zero azimuth. The blade is then rotated to the new azimuth position and the new pitch, flap, and lead-lag rotations are applied.

If the center of rotation differed for each rotation (e.g. flap hinge offset), Equation 58 would be considerably more complex. Allowing for an offset for each rotation results in the following generalized equation.

$$\begin{aligned} \vec{X}_{new} = \mathbf{R}_{\theta_{new}} \Big(\mathbf{R}_{\beta_{new}} \Big(\mathbf{R}_{\delta_{new}} \Big(\mathbf{R}_{\Delta\psi} \Big(\mathbf{R}_{\delta_{old}}^T \Big(\mathbf{R}_{\beta_{old}}^T \Big(\mathbf{R}_{\theta_{old}}^T \Big(\vec{X}_{old} - \vec{r}_{\theta_{old}} - \vec{r}_{\beta_{old}} - \vec{r}_{\delta_{old}} - \vec{X}_0 \Big) \\ + \vec{r}_{\theta_{old}} \Big) + \vec{r}_{\beta_{old}} \Big) + \vec{r}_{\delta_{old}} \Big) - \vec{r}_{\delta_{new}} \Big) - \vec{r}_{\beta_{new}} \Big) - \vec{r}_{\theta_{new}} \Big) + \vec{r}_{\theta_{new}} + \vec{r}_{\beta_{new}} + \vec{r}_{\delta_{new}} + \vec{X}_0 + \Delta\vec{X} \end{aligned} \tag{59}$$

Although the basic strategy is still the same, there is a considerable amount of book keeping that is required to correctly enforce the blade dynamics. Another difficulty presented in Equation 59 is that the hinge offsets are conveniently defined in different basis systems. Therefore, they must be rotated into a consistent basis before use. Due to these difficulties, the modeling of the detailed blade dynamics is reserved for the 6DOF implementation.

CHAPTER IV

TEST CASES AND CFD MODELING

4.1 Unstructured Modeling Process

The ultimate goal of the grid generation process is to obtain sufficient resolution to ensure a grid independent solution. Since CFD problems possess millions of degrees of freedom that must be solved on limited computational resources, true grid independence is seldom achieved in practice. Typically, references to grid independence indicate asymptotic behavior of a limited aspect of the problem such as forces or moments. Attempts were made to achieve limited grid independence with the computational grids utilized herein by iterating on the placement of GridTool sources to obtain an optimal solution. The best practices observed for placing sources in rotor grids is described below.

Unstructured grids are typically created by concentrating points on the surface of the configuration and utilizing large spacing in the far field. The unstructured algorithm automatically generates the volume mesh based on the specified surface spacing. This process works well for most configurations, but fails to produce quality grids for rotary wing problems. The problem with helicopter configurations is that the rotor induces significant flow effects that occur away from the fuselage.

To ensure that adequate refinement was present in the rotor wake a two- to three-stage approach was utilized. The first step is to generate a good surface distribution by following the traditional approach outlined above. An example of the sourcing required for the first step is shown Figure 16. Once the baseline grid is established, off-body sources are placed to refine the grid in the region of the rotor wake. The precise location of the wake is unknown for the second step, so three general source placement strategies are applied:

1. Place strong sources along the path swept by the blade tip.

2. Place medium strength sources along the path swept by the blade root.

3. Place a series of lightly weighted line sources in the vicinity of the rotor to generate a fairly uniform grid point distribution throughout a rotor wake box.

Figure 17 shows an example of this general rotor wake refinement strategy.

When a specific flow condition is considered a more precise wake refinement can be applied. Prior to applying this refinement approach, a solution using the general wake refinement strategy must be obtained. The typical process is to obtain an actuator disk solution using the blade element loading model. Once the general rotor wake solution is know, streamlines are generated with a flow visualization program. These streamlines are then imported into GridTool and rotor wake sources are placed directly on the streamlines as shown in Figure 18. The premise of the precise wake refinement strategy is to concentrate grid points along the trajectory of the tip vortex.

It is important to note that the strategy for rotor wake refinement described here is unnecessary when an adaptive unstructured method is utilized. Adaptive methods refine the rotor wake as it develops, so only the first step of generating the baseline grid is required. However, adaptive strategies can encounter difficulties after a few levels of refinement as grids cells tend to become highly stretched. Refinement can also lead to numerical stiffness if the grid size changes too rapidly.

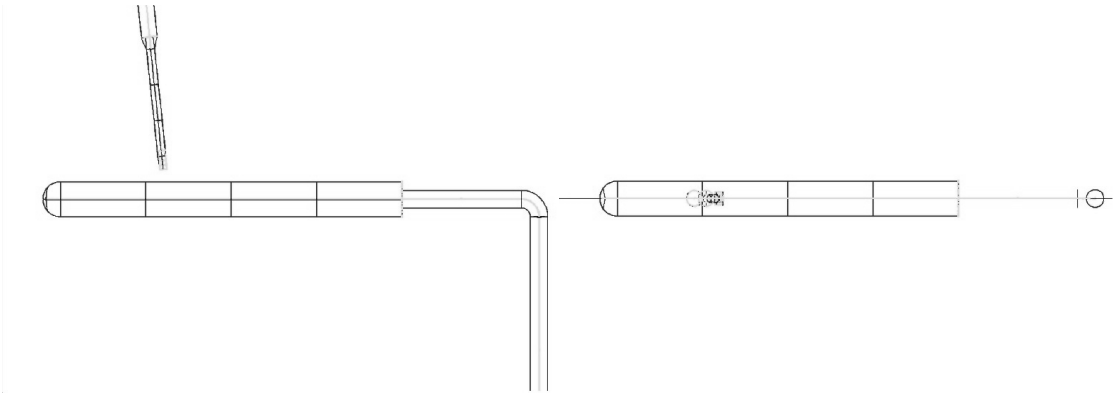

(a) Side View (b) Top View

Figure 16: GridTool source distribution for a baseline configuration.

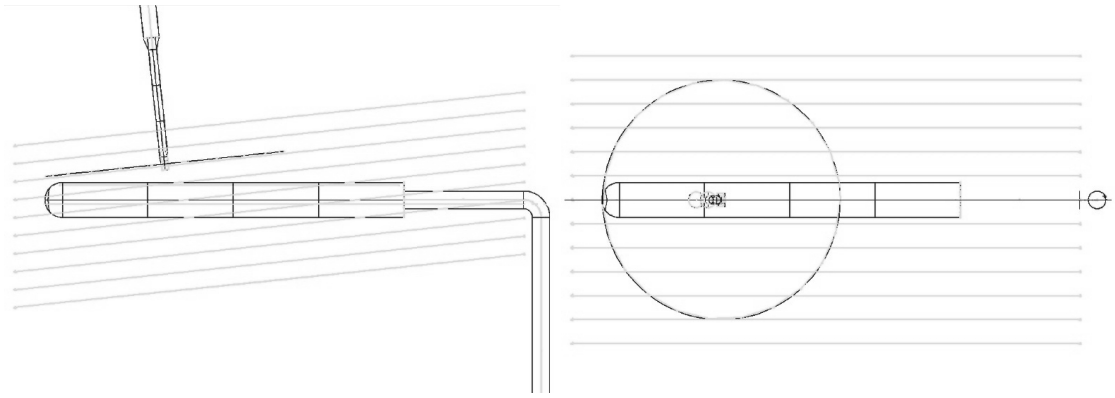

(a) Side View (b) Top View

Figure 17: GridTool source distribution for general rotor wake refinement.

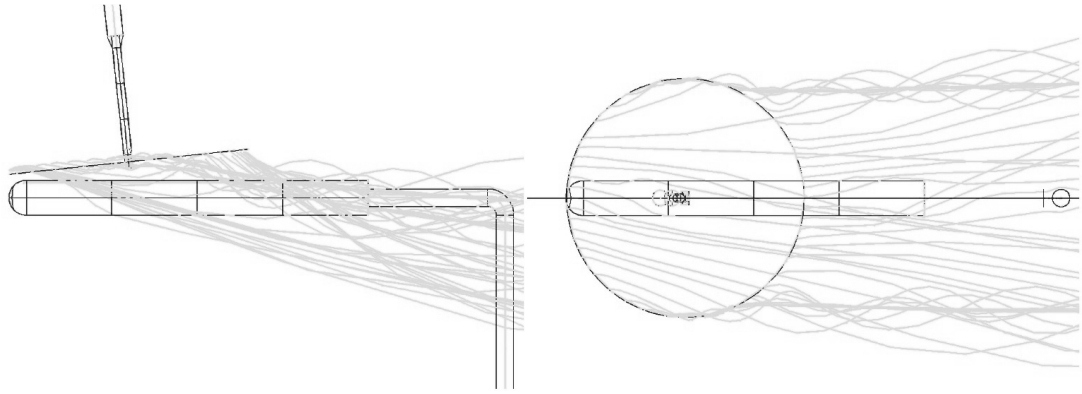

(a) Side View (b) Top View

Figure 18: GridTool source distribution for precise rotor wake refinement.

4.2 Theoretical Rotor

The implementation of the actuator disk was verified through comparison with momentum theory. According to theory, a uniformly loaded actuator disk will accelerate a flow such that the wake velocity far downstream of the disk is twice the induced velocity at the disk center. The magnitude of the induced velocity, v_i, is related to the rotor disk loading, $\frac{T}{A}$, as follows:

$$v_i = -\frac{V_{climb}}{2} + \sqrt{\left(\frac{V_{climb}}{2}\right)^2 + \frac{T}{2\rho A}} \tag{60}$$

The rate of climb, V_{climb}, has the effect of decreasing the induced velocity below the hover value. It should also be noted that Equation 60 is not valid for descent (i.e. $V_{climb} < 0$). Although any disk loading could be used, a value of $\frac{T}{A} = 6.26$ lb/ft^2 was selected to match the condition used by Bettschart [51]. This loading leads to a theoretical induced velocity of 36.3 ft/s at the center of the disk for hover.

The computational grid had a nondimensional blade radius of one and the outer boundaries form a box whose sides are located ten radii from the center of the disk. A specified back pressure boundary condition was used downstream of the actuator disk and characteristic far field conditions were used on the remaining boundaries. Due to an occasional instability at the back pressure boundary for true hover a climb rate of 32.8 ft/s was applied (also used by Bettschart), reducing the expected induced velocity to 23.4 ft/s.

4.3 Supersonic Ramp

The overset implementation was tested using a supersonic ramp test case similar to the one used to verify the overset implementation in USM3D [112]. The USM3D test case had a 15° ramp and a $M_\infty = 2.5$ free stream flow. In the current study the ramp angle was set to be 14.51°. For the 14.51° ramp, the exact pressure ratio across the shock is $\frac{p_2}{p_1} = 2.4027$ and the corresponding shock angle is $\theta_{shock} = 36.4133°$ [113].

The primary goal of this test case is to verify that the shock is not distorted across the overset grid boundaries. The lower grid ranges from the ramp surface to Z=0.6 and the upper grid ranges from Z=0.4 to Z=1.5. The region between Z=0.4 and Z=0.6 is the overlap

region between the two grids. The width of the grid is 0.5. The grid geometry is shown in Figure 19.

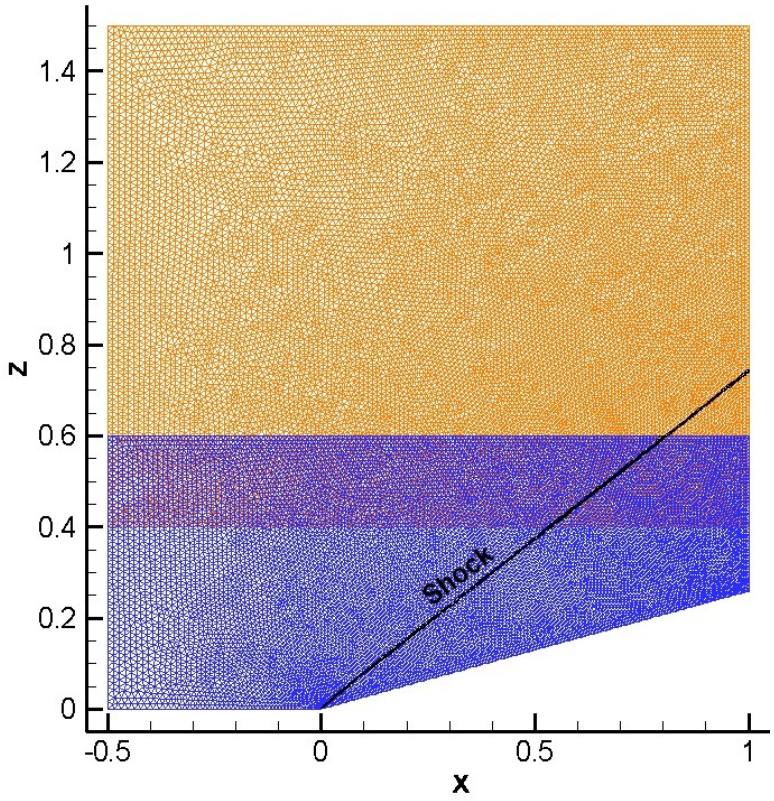

Figure 19: Geometry for the supersonic ramp test case.

4.4 Georgia Institute of Technology (GIT) Model

The GIT rotor / airframe interaction configuration was utilized as the initial validation case for all of the rotor models implemented into FUN3D. This geometry has been extensively tested [11]-[18] in the GIT John J. Harper 7 ft x 9 ft wind tunnel [114]. A number of convenient features make this model ideal for validating numerical analyses.

- Nearly rigid blades allow structural deformations to be neglected.
- A teetering rotor causes the blades to flap as a single body rather than individually.
- The pitch links are removed to reduce the hub size and decrease the number of rigid body degrees of freedom for the blade.

- The minimized hub size reduces hub effects on the flow.
- A simple fuselage geometry enables easier identification of flow effects.
- The radial symmetry of the fuselage allows for pressure measurements to be made around the entire body.

Details of the testing procedure can be found in Brand [11] and Liou [16]. The CFD model for this configuration with the wind tunnel floor and ceiling is shown in Figure 20.

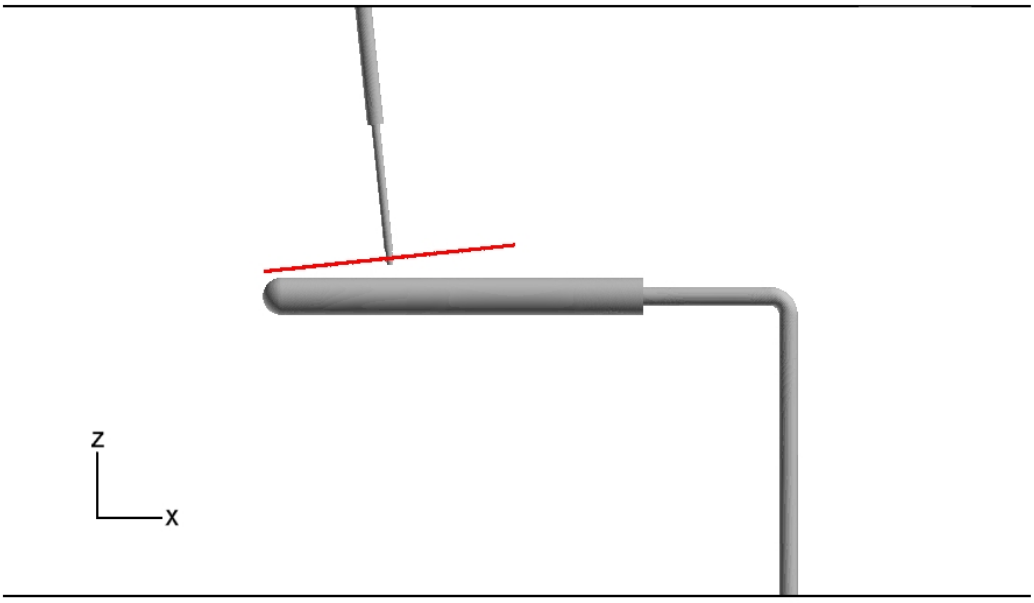

Figure 20: CFD model of the GIT configuration with an actuator disk.

The GIT configuration consists of a cylindrical fuselage with a hemispherical nose mounted from the wind tunnel floor through a strut that attaches to the rear face of the fuselage. A summary of the model parameters normalized by the blade radius are shown in Table 3. The fuselage length and strut dimensions are not given in the references, but have been approximated from the diagrams given in Brand [11]. The fuselage length is estimated to be three rotor radii. The strut is assumed to be cylindrical with a diameter equal to one half the diameter of the fuselage. The strut is assumed to extend one rotor radius downstream before bending 90 degrees and connecting to the floor.

The rotor is mounted from the ceiling via a rotor shaft that is tilted six degrees forward to simulate forward flight. The rotor blades are rectangular and are comprised of the

NACA 0015 airfoil section. The blades are untwisted and have a fixed collective pitch of ten degrees. The dimensional blade radius is 0.4572 m. The hub center is located one radius downstream of the fuselage nose and three tenths of a radius above the fuselage centerline. The dimensions of the shaft have been approximated from the diagrams in Brand [11]. The rotor shaft was assumed to be cylindrical with a diameter of 0.0678 R. After a shaft length of one rotor radius the shaft diameter is increased to 0.1312 R, but this change probably has negligible influence on the resulting flow.

Table 3: Geometry for the GIT Configuration

Variable	**Value**
Fuselage Diameter	0.2931 R
Fuselage Nose Radius	0.1465 R
Fuselage Length (estimated)	3.0000 R
Floor Distance (to fuselage centerline)	2.3684 R
Fuselage Angle of Attack	0°
Fuselage Sideslip Angle	0°
Strut Diameter (estimated)	0.1465 R
Shaft Diameter (estimated)	0.0678 R
Rotor Blade Radius	1.0000 R
Rotor Blade Chord	0.1881 R
Rotor Blade Cutout	0.0270 R
Rotor Blade Collective	10°
Rotor Hub Location, X_0	1.0000 R
Rotor Hub Location, Z_0	0.3000 R
Rotor Shaft Angle	-6.0°

Two hub geometries were considered for the CFD model. The actual hub was essentially 71 mm tall, 51 mm wide, and 25 mm deep. A simplified geometry with a cylindrical shape was created to approximate the hub influence when the rotor was on. The diameter of the simplified hub is equal to the shortest dimension of the actual hub (25 mm). The approximate hub is representative of the actual hub geometry, but is blended into the shaft to reduce the number of fine details to resolve. A depiction of the CFD hub models is shown in Figure 21.

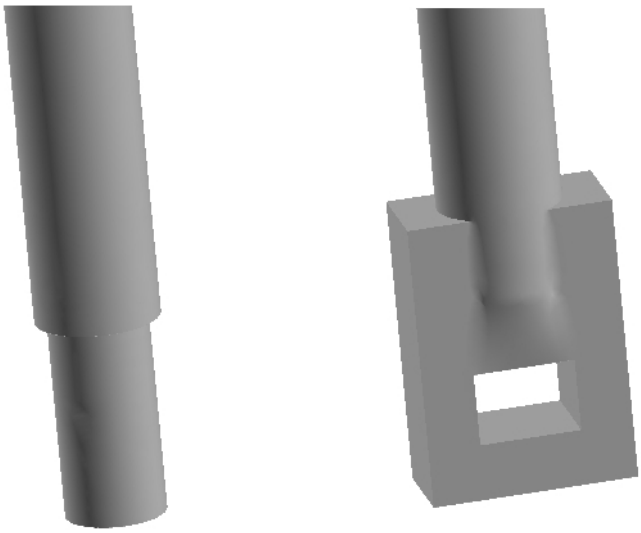

(a) Simplified (b) Approximate

Figure 21: GIT hub comparison: Simplified vs. Approximate.

In the present study an advance ratio of $\mu = 0.1$ was selected for comparison. This advance ratio is low enough to provide a strong rotor / airframe interaction while being large enough to minimize the influence of the rotor wake reflecting off of the floor (i.e. no ground effect). The rotor speed is fixed at a value of $\Omega = 2100$ RPM corresponding to a tip velocity of 100.5 m/s ($M_{tip} = 0.295$). This results in a very small free stream velocity of 10.05 m/s ($M_\infty = 0.0295$). For this case the thrust coefficient and flap angles were measured [11] to be $C_T = 0.009045$, $\beta_{1S} = -2.02$, and $\beta_{1C} = -1.94$.

4.5 NASA Langley ROBIN Model

The NASA Langley ROtor Body INteraction (ROBIN) model is more representative of an actual helicopter geometry, but is simple enough to be described by a set of equations. The ROBIN model has been examined in a variety of experiments [9],[19]-[31] performed in the NASA Langley 14 ft by 22 ft wind tunnel [115] (formerly known as the Langley V/STOL tunnel). This model also provides a good database of information for validating analyses. However, three different test arrangements have been utilized over the years. The three arrangements differed by the mounting of the rotor and the fuselage support, but the nondimensional description of the ROBIN fuselage is consistent among the various

experiments. A summary of the test arrangements used in each experiment is listed below.

1. The Freeman and Mineck experiment [9] had a fuselage mounted rotor. The fuselage was supported with an inclined sting. Figure 22 shows a sketch of this arrangement.

2. The Ghee and Elliott experiment [30] had a fuselage mounted rotor. The fuselage was supported by a vertical strut.

3. The Mineck and Althoff experiment [31] had a ceiling mounted rotor. The fuselage was supported by a vertical strut. A photograph of this arrangement is shown in Figure 23.

The inflow experiments (References [19] to [27]) also used the second arrangement. Due to differences in the experimental setup, the CFD model differs for each experimental setup.

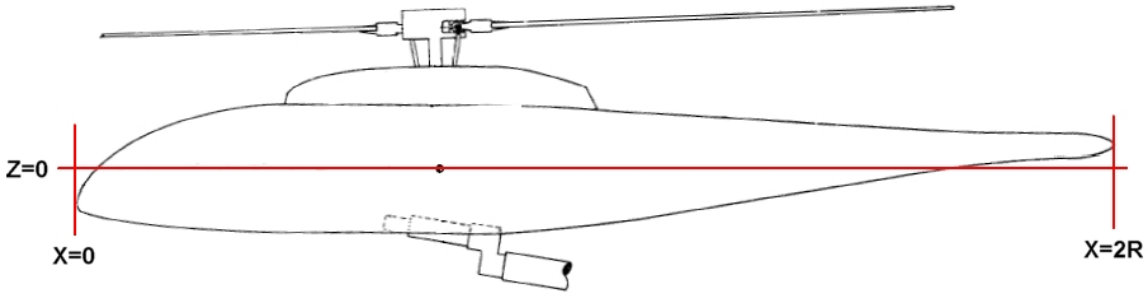

Figure 22: ROBIN experimental setup. From Reference [9].

The ROBIN body and nacelle are generated through a set of super-ellipse equations. Using the body longitudinal station, X/L_{ref}, the height (H), width (W), camber (Z_0), and elliptical power (N) are defined as follows:

$$\begin{bmatrix} H\left(X/L_{ref}\right) \\ W\left(X/L_{ref}\right) \\ Z_0\left(X/L_{ref}\right) \\ N\left(X/L_{ref}\right) \end{bmatrix} = C_6 + C_7\left(C_1 + C_2\left(\frac{X/L_{ref} + C_3}{C_4}\right)^{C_5}\right)^{\frac{1}{C_8}} \tag{61}$$

Each parameter depends on a set of eight coefficients. The Mineck and Althoff [31] coefficients require logic statements to avoid division by zero in Equation 61. In the present

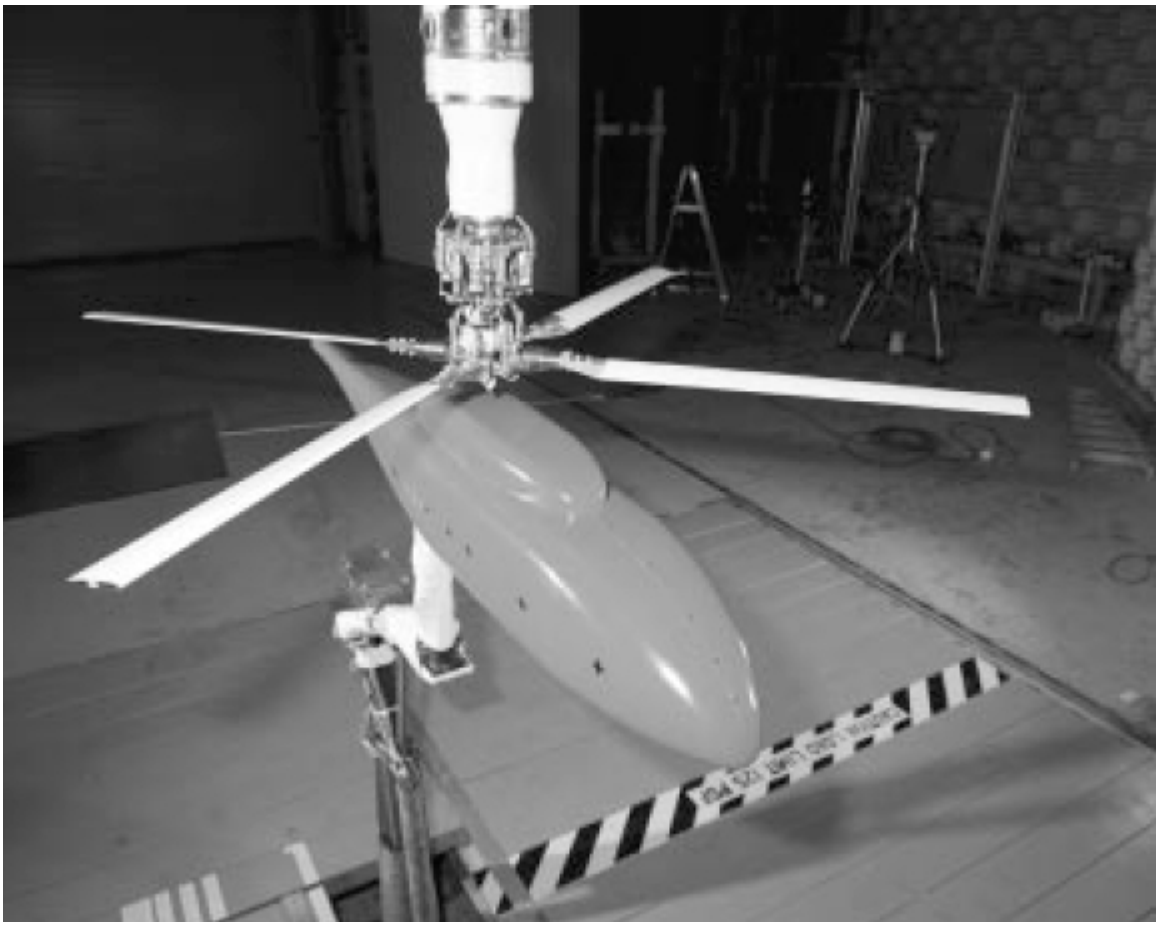

Figure 23: ROBIN experimental setup. From Reference [31].

work a modified set of coefficients is utilized, which generate the correct configuration, but enable direct use of Equation 61. the modified coefficients are listed in Table 4 for the body and Table 5 for the pylon.

Once the height, width, camber, and elliptical power are known the radial coordinate for a given longitudinal station and angular coordinate, ϕ, can be computed.

$$r = \left(\frac{(0.25\, H\, W)^N}{\left(0.5\, H \sin\phi\right)^N + \left(0.5\, W \cos\phi\right)^N} \right)^{\frac{1}{N}} \tag{62}$$

The cross section coordinates for a point on the body are computed from the following equations.

$$Y/L_{ref} = r \sin\phi \tag{63}$$

$$Z/L_{ref} = r \cos\phi + Z_0 \tag{64}$$

By varying the longitudinal coordinate ($0 \leq X/L_{ref} \leq 2$) and the angular coordinate ($0 \leq \phi < 2\pi$) the ROBIN fuselage can be completely described.

The U.S. Army 2-Meter Rotor Test System [116] was used for the rotor in all but the Freeman and Mineck experiment. The ROBIN experiments typically used four rectangular blades with a -8° linear twist (References [28, 29] used tapered blades). NACA 0012 airfoil sections were used for all but the Freeman and Mineck experiment, which used a NACA RC-10-(B) M002 profile.

In this study only two of the three experimental arrangements are modeled. Steady simulations are compared to Freeman and Mineck [9] and unsteady computations are validated with the Mineck and Althoff experiment [31]. Relevant model parameters for both experiments are listed in Table 6. The rotor system was similar for both arrangements, but Freeman and Mineck had a 16% longer nondimensional radius and a different airfoil section. The other signifcant differences are the Mineck and Althoff rotor was shifted to the right of the fuselage centerline and had a 32% larger rotor / fuselage clearance.

Rotor-off computations are compared with Run 12 Point 90 and Run 13 Point 94 in the Freeman and Mineck experiment. These two tests were performed at the same conditions and can therefore be used as an indication of the experimental uncertainty. For these test

Table 4: ROBIN Body Shape Coefficients

	$0.0 < X/L_{ref} < 0.4$							
Function	C_1	C_2	C_3	C_4	C_5	C_6	C_7	C_8
H	1.0	-1.0	-0.4	0.4	1.8	0.0	0.25	1.8
W	1.0	-1.0	-0.4	0.4	2.0	0.0	0.25	2.0
Z_0	1.0	-1.0	-0.4	0.4	1.8	-0.08	0.08	1.8
N	2.0	3.0	0.0	0.4	1.0	0.0	1.0	1.0
	$0.4 < X/L_{ref} < 0.8$							
Function	C_1	C_2	C_3	C_4	C_5	C_6	C_7	C_8
H	0.25	0.0	0.0	1.0	0.0	0.0	1.0	1.0
W	0.25	0.0	0.0	1.0	0.0	0.0	1.0	1.0
Z_0	0.0	0.0	0.0	1.0	0.0	0.0	1.0	1.0
N	5.0	0.0	0.0	1.0	0.0	0.0	1.0	1.0
	$0.8 < X/L_{ref} < 1.9$							
Function	C_1	C_2	C_3	C_4	C_5	C_6	C_7	C_8
H	1.0	-1.0	-0.8	1.1	1.5	0.05	0.2	0.6
W	1.0	-1.0	-0.8	1.1	1.5	0.05	0.2	0.6
Z_0	1.0	-1.0	-0.8	1.1	1.5	0.04	-0.04	0.6
N	5.0	-3.0	-0.8	1.1	1.0	0.0	1.0	1.0
	$1.9 < X/L_{ref} < 2.0$							
Function	C_1	C_2	C_3	C_4	C_5	C_6	C_7	C_8
H	1.0	-1.0	-1.9	0.1	2.0	0.0	0.05	2.0
W	1.0	-1.0	-1.9	0.1	2.0	0.0	0.05	2.0
Z_0	0.04	0.0	0.0	1.0	0.0	0.0	1.0	1.0
N	2.0	0.0	0.0	1.0	0.0	0.0	1.0	1.0

Table 5: ROBIN Pylon Shape Coefficients

	$0.4 < X/L_{ref} < 0.8$							
Function	C_1	C_2	C_3	C_4	C_5	C_6	C_7	C_8
H	1.0	-1.0	-0.8	0.4	3.0	0.0	0.145	3.0
W	1.0	-1.0	-0.8	0.4	3.0	0.0	0.166	3.0
Z_0	0.125	0.0	0.0	1.0	0.0	0.0	1.0	1.0
N	5.0	0.0	0.0	1.0	0.0	0.0	1.0	1.0
	$0.8 < X/L_{ref} < 1.018$							
Function	C_1	C_2	C_3	C_4	C_5	C_6	C_7	C_8
H	1.0	-1.0	-0.8	0.218	2.0	0.0	0.145	2.0
W	1.0	-1.0	-0.8	0.218	2.0	0.0	0.166	2.0
Z_0	1.0	-1.0	-0.8	1.1	1.5	0.065	0.06	0.6
N	5.0	0.0	0.0	1.0	0.0	0.0	1.0	1.0

Table 6: Geometry for the ROBIN Configuration

Variable	Freeman & Mineck	Mineck & Althoff
Reference Length, L_{ref}	5.164 ft	3.279 ft
Fuselage Length	2.0 L_{ref}	1.997 L_{ref}
Rotor Hub Location, X_0	0.690 L_{ref}	0.696 L_{ref}
Rotor Hub Location, Y_0	0.000 L_{ref}	0.051 L_{ref}
Rotor Hub Location, Z_0	0.274 L_{ref}	0.322 L_{ref}
Fuselage Angle of Attack	Varies	0°
Shaft Angle w.r.t. Fuselage	-2.0°	Varies
Fuselage Sideslip Angle	0°	1.2°
Rotor Blade Radius	1.0 L_{ref}	0.861 L_{ref}
Rotor Blade Chord	0.0686 L_{ref}	0.0663 L_{ref}
Rotor Blade Cutout	0.2 L_{ref}	0.2066 L_{ref}
Rotor Blade Airfoil	NACA RC-10-(B) M002	NACA 0012
Rotor Blade Twist	-8.0°	-8.0°

the fuselage angle of attack was set to zero and the tunnel flow was set at 137.89 ft/s (M_∞ = 0.1235).

The simple actuator disk models are compared to Run 25 Point 148 in the Freeman and Mineck experiment. Test 25-148 was run at an advance ratio of 0.15, which corresponds to a tunnel velocity of 97.3 ft/s (M_∞ = 0.0871). The fuselage angle of attack was set to 2.86 degrees and the thrust coefficient was 0.00500.

The Results chapter compares with the Mineck and Althoff experiment. The run at an advance ratio of 0.151 and thrust coefficient of 0.00643 was chosen as the basis for comparison. Since the rotor is mounted from the ceiling the fuselage angle of attack is set to zero for this case, but the rotor shaft is tilted forward three degrees with respect to the free stream flow. The control angles are given as $\theta_0 = 16.3°$, $\theta_{1S} = -2.4°$, and $\theta_{1C} = 2.7°$. Test conditions for this case are summarized in Table 7. The assumed references conditions are listed in Table 8.

4.6 ONERA Dauphin Model

The ONERA Dauphin configuration was obtained through a US-France Memorandum of Agreement (MoA) for studying the effects of rotor /airframe interactions. This geometry

Table 7: ROBIN Test Data

Variable	Value
Advance Ratio, μ	0.151
Rotor Rotational Speed, Ω	2000 RPM
Free stream Mach Number, M_∞	0.080
Thrust Coefficient, C_T	0.00643
Shaft Tilt, α_{shaft}	3.0°
Collective Pitch, $\theta_{0.75R}$	10.3°
Lateral Cyclic Pitch, θ_{1C}	2.7°
Longitudinal Cyclic Pitch, θ_{1S}	-2.4°
Coning Angle (assumed), β_0	1.5°
Reynolds Number, Re	1.86x10^6

Table 8: ROBIN Reference Values

Variable	Value
Density, ρ_∞	0.002378 slug/ft^3
Viscosity, μ	3.74 x 10^{-7} slug/(ft*s)
Temperature, T	518.67 R
Length (half fuselage), L_{ref}	3.2792 ft
Velocity (compressible), a_∞	1116.4 ft/s
Velocity (incompressible), V_∞	89.278 ft/s

has been tested [35]-[37] in the ONERA S2Ch (now decommissioned) and F1 [117] wind tunnels. This configuration is a 1/7.7 scale model of the Eurocopter Dauphin 365N helicopter and is significantly more complex than the generic shapes of the GIT and ROBIN models. A picture of the model in the ONERA F1 wind tunnel is shown in Figure 24.

Figure 24: Dauphin experimental setup. From Reference [111].

The rotor system is mounted on the fuselage and consists of four rectangular blades with an OA209 airfoil shape. The blades have a radius of 0.75 m, a 0.05 m chord, and a linear twist of -12 degrees [37]. The blades rotate clockwise when viewed from above with a tip velocity of ΩR = 100 m/s. The rotor shaft is tilted forward 4 degrees with respect to the fuselage reference line.

Due to the proprietary nature of this configuration, only previously published results [111] are shown. All of the cases presented in this work are at a free stream Mach number of M_∞ = 0.044 and a fuselage angle of attack of $\alpha_F = -3°$. This results in an advance ratio of μ = 0.15 for the rotor on case. The measured thrust coefficient with the rotor on is C_T = 0.00615.

CHAPTER V

METHOD VERIFICATION

5.1 Flow Assumptions

The majority of verification cases utilized the fully turbulent RANS equations coupled with the Spalart-Allmaras turbulence model. The viscous spacing for all RANS cases resulted in a $y^+ < 1$ over the fuselage. The two exceptions are the isolated rotor and the overset verification cases, which were performed with the inviscid flow assumption. The actuator disk is inherently and inviscid model, so the use of the RANS equations is unnecessary when a fuselage is absent from the computation. The overset ramp and overset GIT computations utilized the inviscid flow option to reduce the number of nodes for these cases, since access to a large memory computer was not available at the time. The incompressible flow option is utilized for all of the isolated fuselage and source based actuator disk cases, except where a direct comparison between compressible and incompressible results is desired. An incompressible pressure jump actuator disk boundary condition was not available, so all of these cases use the compressible flow option. The time-accurate computations are performed with compressible flow, since the rotor tip speed becomes important for these cases.

5.2 Flow Solver Verification

In this section the FUN3D flow solver is verified against the baseline experimental test cases (i.e. the rotor-off cases). One item of particular interest during this investigation was the ability of unstructured methods to model complex geometries. Although the details of the experimental setup were not always known (e.g. strut and hub geometries), an attempt was made to model as many features of the wind tunnel test geometry as possible. Features that are specifically not modeled include:

- Hub details such as pitch linkages and hinges.

- Fuselage gaps which are typically present at strut and hub attachment points.
- Geometric imperfections such as a dent, bump, or crease in a fuselage.
- The attachment from the blade root to the hub.

Modeling hub details is prohibitively expensive, since these features tend to be very small and are in constant motion. The other detailed features are neglected because they are either not well described or are simply unknown.

The isolated fuselage cases utilized the fully turbulent RANS equations coupled with the Spalart-Allmaras turbulence model. The viscous spacing for these cases resulted in a $y^+ < 1$ over the fuselage. Since the free stream Mach number was less that 0.1 for GIT and ROBIN geometries, the incompressible flow option is utilized for the isolated fuselage computations.

5.2.1 GIT Configuration Without Rotor

The GIT configuration is a nominally simple fuselage, but the rotor-off pressure coefficient distribution has never been adequately captured by a computational technique. Considering the simplicity of this model, an effort to successfully match the experimental pressure coefficient was undertaken. Previous investigations [46, 71, 78] have been unsuccessful primarily because the rotor shaft and hub have been neglected from the computational model. The shaft and hub are located in close proximity to the fuselage and therefore create a local blockage in the flow. These features need to be modeled to match the experimental trend and provide credibility to the computational result.

CFD solutions have been obtained for five hub variations for this configuration. The isolated configuration follows the common CFD approach of neglecting the rotor shaft and hub. The remaining cases included the rotor shaft and tested the two hub geometries shown in Figure 21. The simplified hub was modeled as a cylinder with a diameter equal to the shortest dimension of the actual hub. The approximate hub is a rigid representation of the actual hub geometry, and therefore it can not flap about the teetering hinge.

The corresponding grid information is summarized in Table 9. The number of nodes

nearly doubles when the hub is modeled because the rotor shaft and fuselage strut have also been included. The strut, hub, and shaft are modeled as viscous walls, so the majority of the additional nodes are introduced through the viscous layers generated on these features. Additional nodes are required for the approximate hub due to the more detailed hub representation. All of these grids are a product of iterative sourcing attempts in GridTool to achieve a grid independent solution.

Table 9: GIT Rotor Off Grid Information

Configuration	Nodes	Tetrahedra	Boundary Faces
Isolated Fuselage	1.1 million	6.3 million	76 thousand
Simplified Hub	1.9 million	11.1 million	115 thousand
Approximate Hub	2.1 million	12.1 million	136 thousand

The centerline pressure coefficient results for each of the cases are shown in Figure 25. The isolated fuselage obviously fails to predict the blockage ($C_p = -0.3$) attributed to the rotor shaft. Using the simplified hub provides a good trend, but fails to predict the magnitude of the pressure drop, resulting in a pressure coefficient of -0.09. The reason for this discrepancy is attributed to the fact that the simplified hub is more aerodynamic than the experimental hub, reducing its interference on the flow. The approximate hub improves the prediction of the magnitude of the pressure drop ($C_p = -0.24$), but overpredicts the pressure coefficient forward of the hub by 0.1. The overprediction is a result of the high pressure region in the vicinity of the stagnation point on the forward face of the hub.

The CFD model clearly over predicts the pressure rise forward of the hub. Since the orientation of the hub in the experiment was not known, a variety of orientations were evaluated in an effort to rectify this discrepancy. When the widest side faces the incoming flow ($\psi = 0°$), the over prediction of the pressure is largest due to the larger surface area, and hence the largest effective blockage. When the smaller face is oriented toward the flow ($\psi = 90°$) the over prediction reduces to approximately one-half the $\psi = 0°$ value. A third orientation, which hypothesized that the free stream velocity would blow the hub back in the $\psi = 0°$ orientation, was also tested. With a deflection angle of $\delta = 20°$ the result is similar to that of the undeflected hub, but there is an aft shift in the hub influence. Since

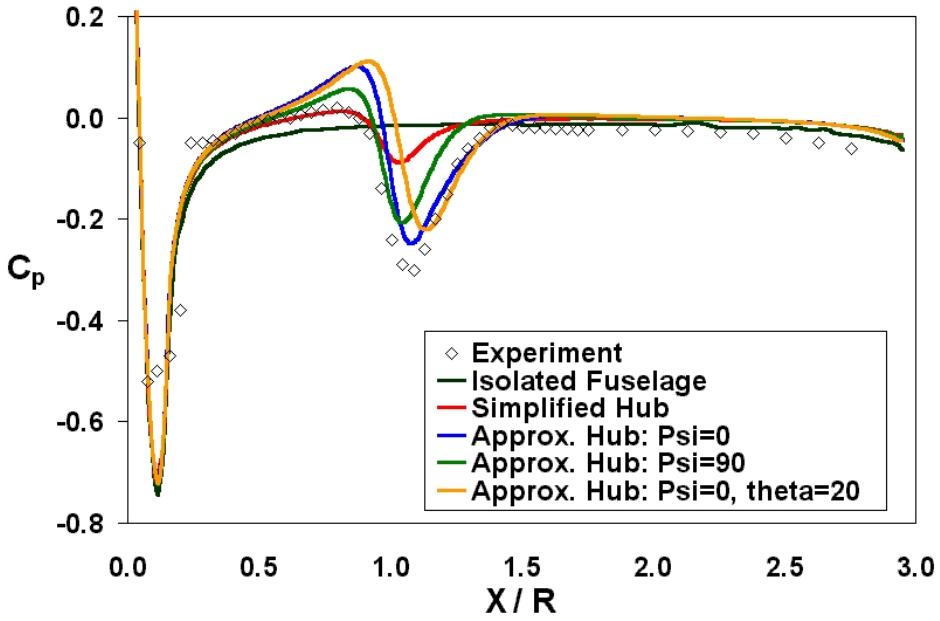

Figure 25: GIT rotor off centerline C_p distribution.

there is ambiguity in the precise orientation of the hub for the rotor-off experiments, further investigation of the pressure over prediction was not pursued. An additional possibility is that the bluff-body shape of the hub may have generated a unsteady separation, which caused it to flap about the teetering hinge. Unsteady flow may have a relieving effect on the high pressure region forward of the hub.

5.2.2 Robin Configuration Without Rotor

The ROBIN configuration was tested with and without the fuselage strut. Surface pressures from the Freeman and Mineck experiment [9] were utilized in this investigation. Although an exact strut model is not given in the report, the strut was approximated to examine its influence on the fuselage surface pressure. Two of the experimental data sets taken at the same conditions (Run 12 Point 90 and Run 13 Point 94) are compared with the computational results from FUN3D. The experimental data from both the left and right halves of the fuselage are shown to give an indication of experimental error and flow unsteadiness. Both test points were taken in a free stream velocity of 138 ft/s (42.0 m/s) and a fuselage angle of attack of zero. The tunnel free stream temperature and pressure are not

specified and are assumed to be sea level standard atmosphere. Since this is a symmetric configuration, the computational results were obtained by modeling half of the geometry. The isolated fuselage configuration had 876,305 nodes and 5,049,303 tetrahedra. The grid with the fuselage and strut consisted of 1,113,365 nodes and 6,363,703 tetrahedra.

A comparison of the predicted surface pressure coefficient contours is shown in Figure 26, where the isolated fuselage, experiment, and fuselage with strut are depicted from top to bottom of the figure. For the purpose of comparison, the experimental data has been mapped to the fuselage where available. The influence of the strut is observed to extend over the sides of the fuselage. The region forward of the strut sees an increase in pressure due to the blockage effects. Aft of the strut, the flow accelerates creating a low pressure region that extends further aft than the isolated geometry. The prediction with the strut is found to be in better agreement with the experimental contours in the area of the strut and aft.

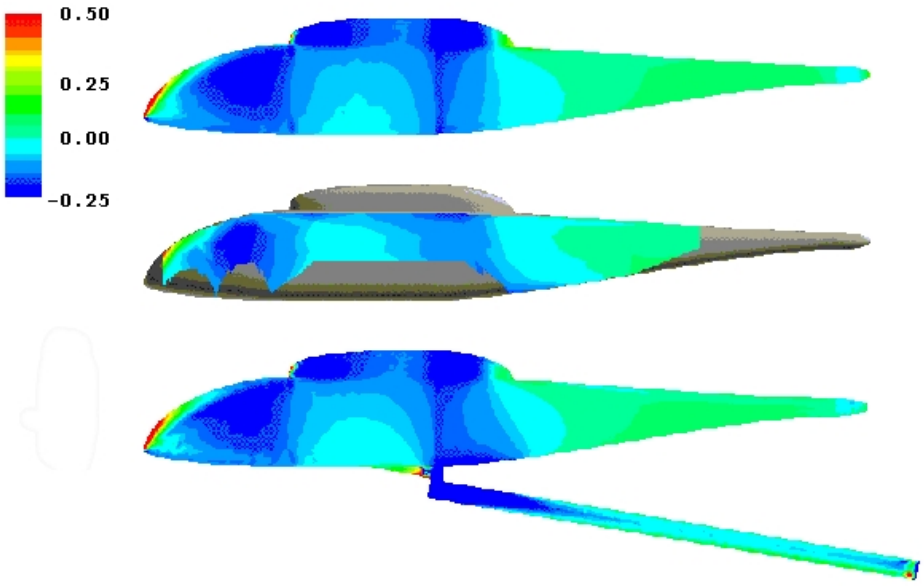

Figure 26: ROBIN surface C_p comparison for the isolated fuselage, experiment, and fuselage with strut.

A quantitative comparison of the pressure data at the six cross sections in the vicinity of the strut is shown in Figure 27. For reference, the strut attaches to the fuselage at approximately X/L = 0.7, where L is defined to be one-half the fuselage length. Figure

27(a) shows little influence due to the strut that far upstream. The minor differences here are attributed to grid variations and provide an indication of the computational error. At X/L = 0.4669 (Figure 27(b), the result with the strut shows a minor shift toward the experimental data; however, this difference may be a result of the computational error and not attributable to the strut. Figure 27(c) is the first section that indicates a significant effect due to the strut. The lower portion of the fuselage sees an increased pressure due to the blockage created by strut. Naturally, the pressure rise increases closer to the strut and reaches a maximum on the lower centerline where $\Delta C_p = 0.1$.

Just aft of the strut (Figure 27(d) the flow acceleration creates a significant decrease in pressure ($\Delta C_p = -0.4$ along the bottom centerline). Unfortunately the cross section in the immediate vicinity of the strut did not include experimental data over the lower half of the fuselage. However, the next section downstream of the strut, shown in Figure 27(e), had pressure taps that extended down to the lower half. At this cross-section an excellent agreement with the experimental data is obtained, verifying once again the importance of modeling all aspects of the geometry. In Figure 27(f) the experimental data indicate that the influence of the strut is still present, but the CFD solution no longer demonstrates a significant effect. The probable reason that the X/L = 1.1619 section no longer sees a strut influence is that the separated flow region aft of the strut is not correctly captured by the approximate strut geometry. There may also have been a gap between the fuselage and strut that may have also influenced the flow in unexpected ways such as flow leakage (e.g., the Dauphin experimental results in the following chapter).

5.3 Actuator Disk Verification

The actuator disk implementation was verified by investigating an isolated rotor with a uniform disk loading in near hover conditions. A uniform disk loading of 6.26 lb/ft^2 was used to duplicate the conditions used by Bettschart [51]. An initial coarse grid was created by clustering nodes at the tip of the actuator disk. Additional sources to refine the rotor wake were not used for the initial grid. This resulted in a grid with 94,678 nodes and 552,909 tetrahedra. The actuator disk model acts on the inviscid portion of the governing

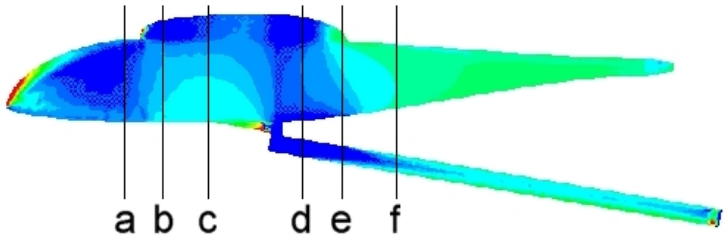

Cross-section Locations

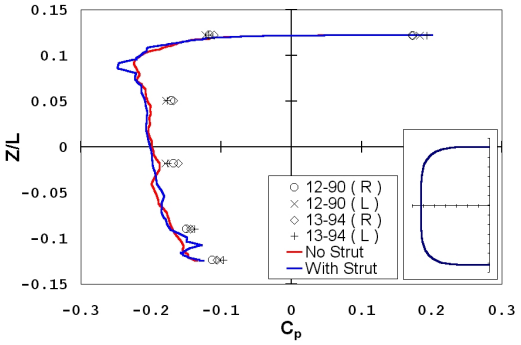

(a) X/L = 0.3498

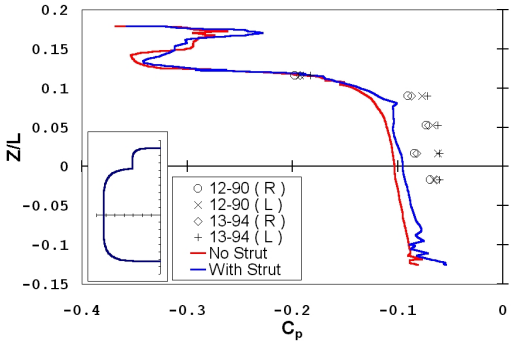

(b) X/L = 0.4669

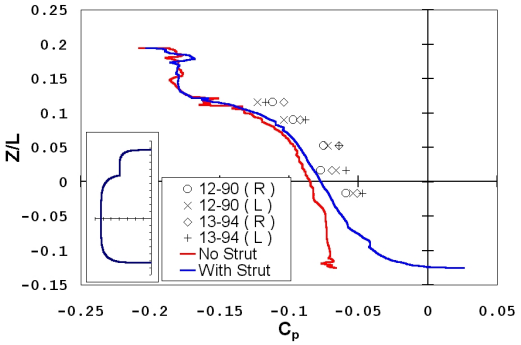

(c) X/L = 0.6003

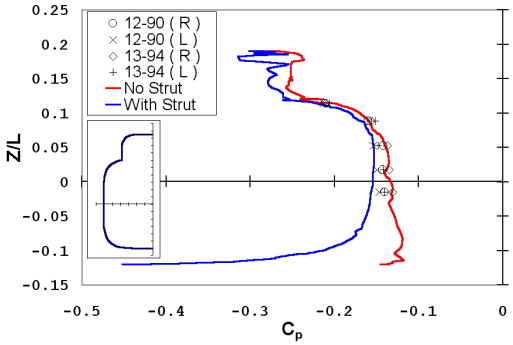

(d) X/L = 0.8809

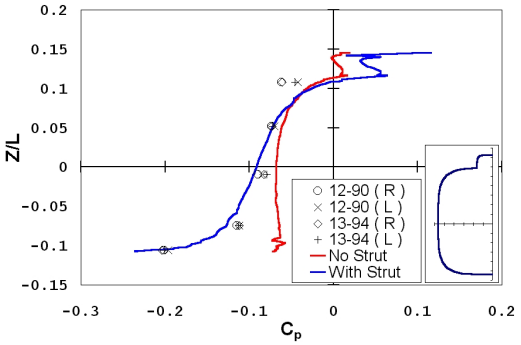

(e) X/L = 1.0008

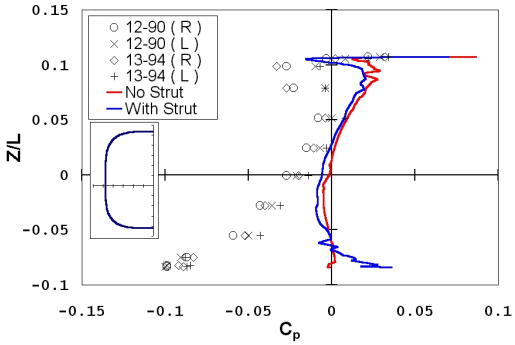

(f) X/L = 1.1619

Figure 27: ROBIN cross-section C_p in the vicinity of the strut.

equations, so the use of the RANS equations was deemed unnecessary since a fuselage is absent from the isolated rotor computations. Both incompressible and compressible computations are performed in this section to study the effect of compressibility on the solution. The source grid was held constant at 200 radial by 720 azimuthal sources, which is overly fine for the isolated actuator disk study.

5.3.1 Isolated Rotor In Hover

Vorticity contours normalized by a reference velocity of $2v_i$ are shown in Figure 28. The compressible tip vortex sheet is observed to diffuse faster than the incompressible case. However, both are found to degrade more rapidly than desired. A small amount of vorticity is observed to be generated in the vicinity of the incompressible actuator disk as a result of source placement. This negligible vorticity is a result of how close the sources are to their associated nodes. The reason this vorticity does not appear in the compressible actuator disk solution is a result of the increased diffusion observed for compressible solutions.

The grid was subsequently refined by applying the precise wake refinement strategy described in the previous chapter. Refinement of the rotor wake yielded a fine hover grid with 799,972 nodes and 4,682,955 tetrahedra. Figure 29 shows the vorticity contours generated on the fine grid. The resulting contours are significantly improved and the vortex is found to propagate downstream with significantly less diffusion than the coarse grid solution. The incompressible solver is once again observed to preserve the tip vortex sheet better than the compressible solver. This is particularly important in establishing the velocity induced by the rotor as shown in Figure 30.

As a vortex diffuses, the effective distance between the vortex and any point in the flow decreases. Assuming the diffused vortex maintains its total strength, the decreased distance causes the velocity induced by the vortex at a point in the flow to increase by the Biot-Savart Law. This explains the induced velocity trend observed for the coarse grid. The vortex initially diffuses inward while maintaining its overall strength, creating a large increase in induced velocity. As diffusion continues to take place the vortex also begins to

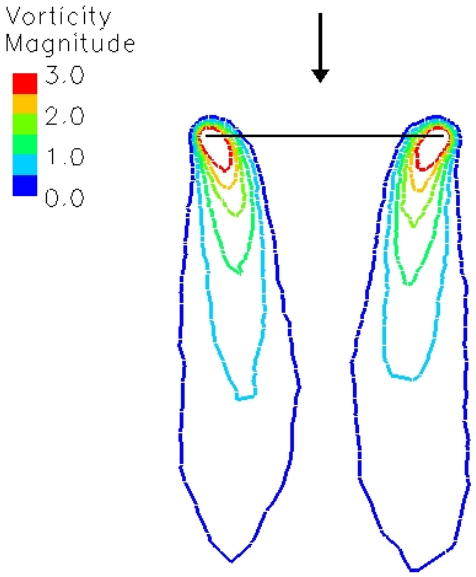

(a) Compressible Solution

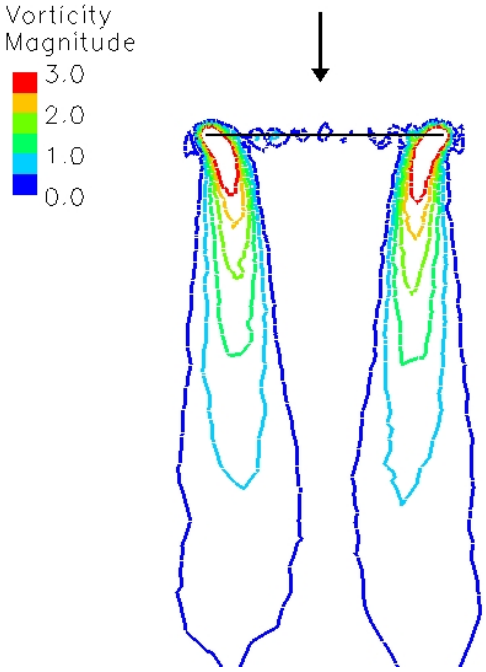

(b) Incompressible Solution

Figure 28: Vorticity contours for a uniform source disk on a coarse grid.

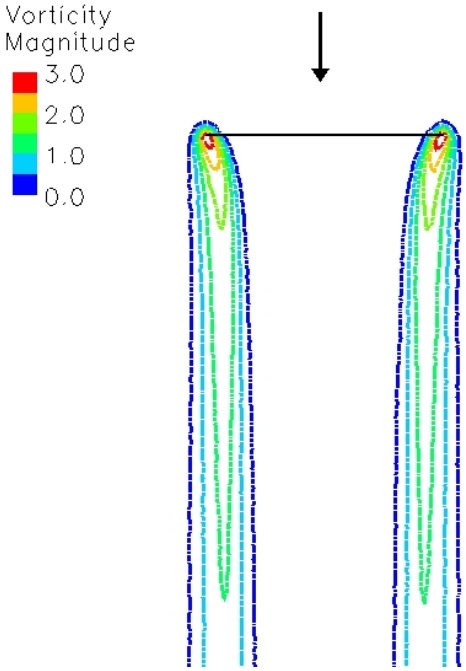

(a) Compressible Solution

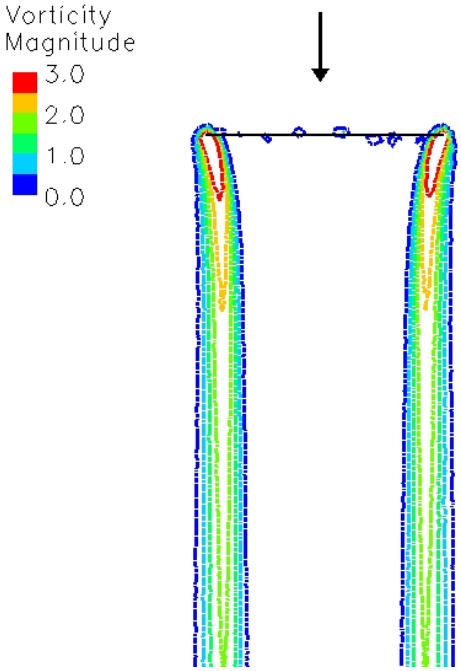

(b) Incompressible Solution

Figure 29: Vorticity contours for a uniform source disk in hover on a fine grid.

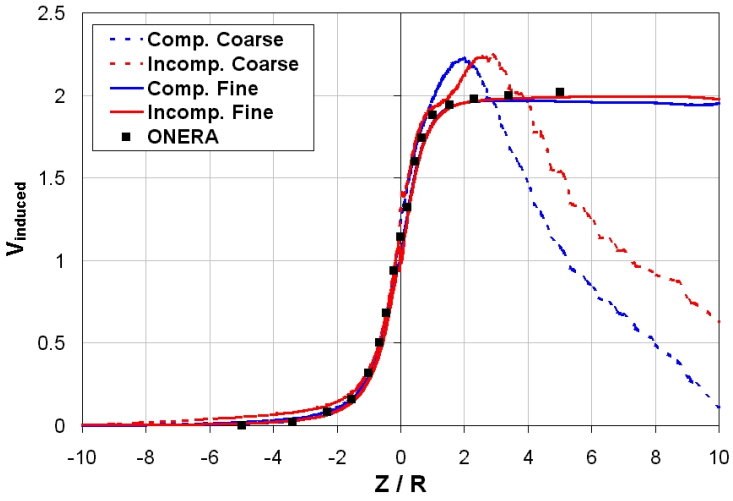

Figure 30: Induced velocity through the centerline of the actuator disk in near hover conditions.

dissipate, which causes the induced velocity to decrease and eventually return to the free stream value.

For the fine grids, the tip vortex is found to be sufficiently captured, allowing the induced velocity to approach the theoretical value of 2. The incompressible solution is found to come closer to the theoretical value of 2, which indicates that it does not suffer as much dissipation as the compressible solution. The fine grid results compare well with the ONERA result [51], which also used a refined rotor wake. The induced velocity for the refined grid cases are shown in Figure 31. Although it is not as obvious as it was with the vorticity contours, the compressible velocity contours also show signs of increased diffusion when compared to the incompressible solution.

5.3.2 Isolated Rotor In Forward Flight

Similar results were also obtained for an isolated rotor in forward flight. For this case an advance ratio of $\mu = 0.1$ was chosen and the disk was aligned at to the free stream at $\alpha = 0°$. The precise wake refinement strategy was utilized by generating streamlines from the coarse grid solution in forward flight. The fine forward flight grid had 721,354 nodes and 4,221,090 tetrahedra.

The vorticity contours for the fine grid solution are shown in Figure 32. As observed

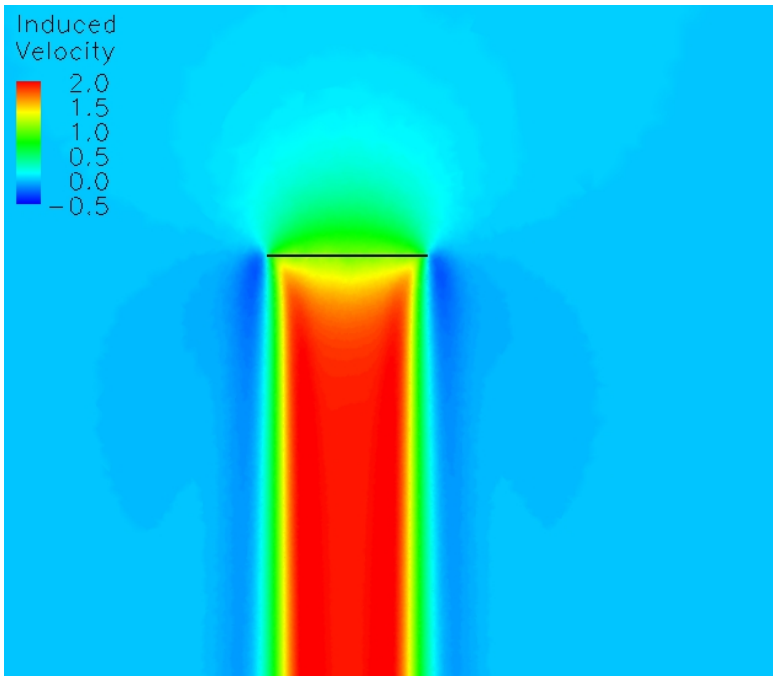

(a) Compressible Solution

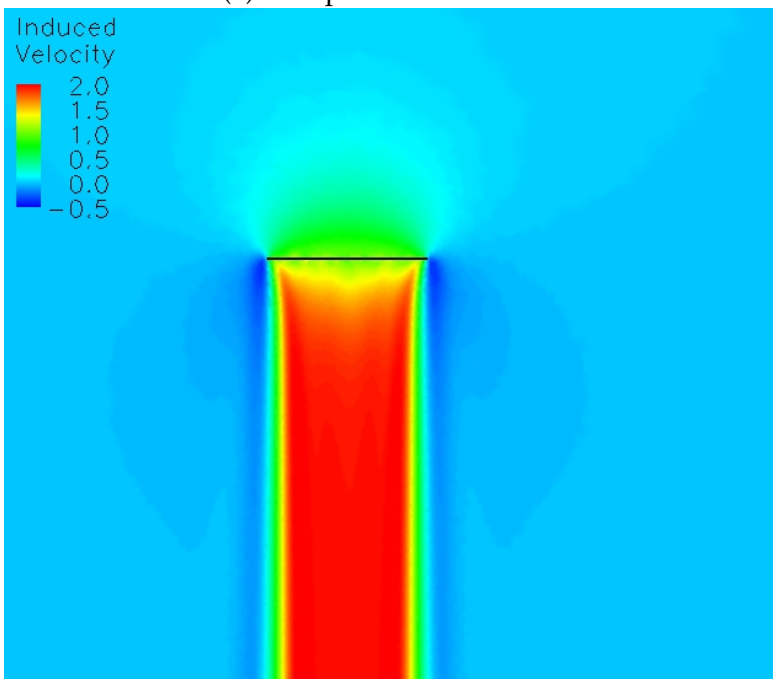

(b) Incompressible Solution

Figure 31: Velocity contours for a uniform source disk in hover on a fine grid.

in hover, the compressible solution is found to diffuse the tip vortex more rapidly than the incompressible solution. Another observation in forward flight is that the forward tip vortex passes through the plane of the actuator disk while the aft tip vortex propagates away from the disk. The interaction between the actuator disk and the forward tip vortex is observed to significantly increase the rate of diffusion for the tip vortex.

Contours of the velocity normal to the actuator disk are shown in Figure 33. The largest difference is observed in the region just below the aft disk tip, where the incompressible velocity contours tend to show sharper features than the compressible ones. This is a direct result of the vortex diffusion smearing out the details in the compressible case. Another observation for the forward flight condition is that the rotor wake distorts as it propagates away from the disk. This differs from theoretical models that assume a wake skew angle. In the present actuator disk result the wake shows a variable skew angle, demonstrating that the wake is developing from first-principles.

5.4 Simple Actuator Disk Loading Models

5.4.1 GIT with a Uniform and Linear Disk Loading

The rotor results for the GIT configuration were initially obtained with a pressure jump actuator disk. The free stream Mach number for this case was $M_\infty = 0.029$ and the fuselage angle of attack was zero. The actuator disk was tilted forward 6 degrees with respect to the fuselage and the blade flap was not modeled. The advance ratio for this case was μ=0.1. In this result the rotor shaft and hub were neglected, but will be considered in the source-based actuator disk results. The grid in this study was based on the isolated configuration, but has additional grid refinement in the rotor wake to give a total of 1,826,529 nodes with 20,834 nodes on the fuselage surface. Both of these cases were run using the compressible flow option in FUN3D, since a robust incompressible pressure jump boundary condition could not be obtained. The fully-turbulent RANS equations are solved for both the pressure jump and source based actuator disk methods in this section.

A pressure coefficient comparison for the uniform and linear actuator disk models along the upper centerline of the GIT configuration is shown in Figure 34. The uniform loading

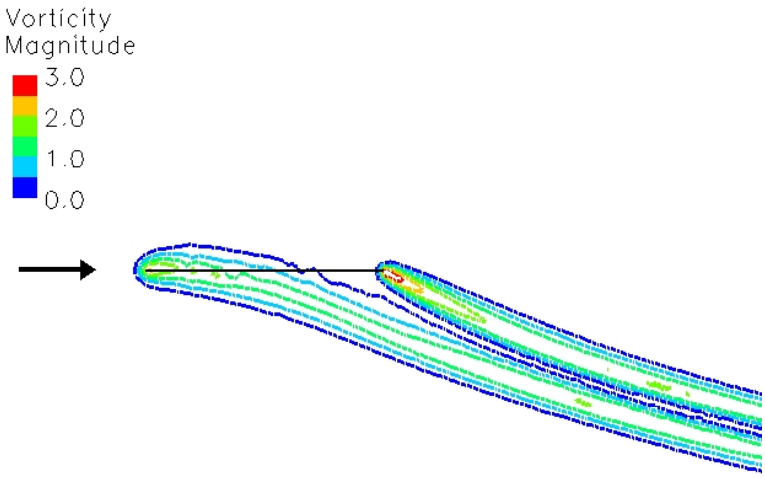

(a) Compressible Solution

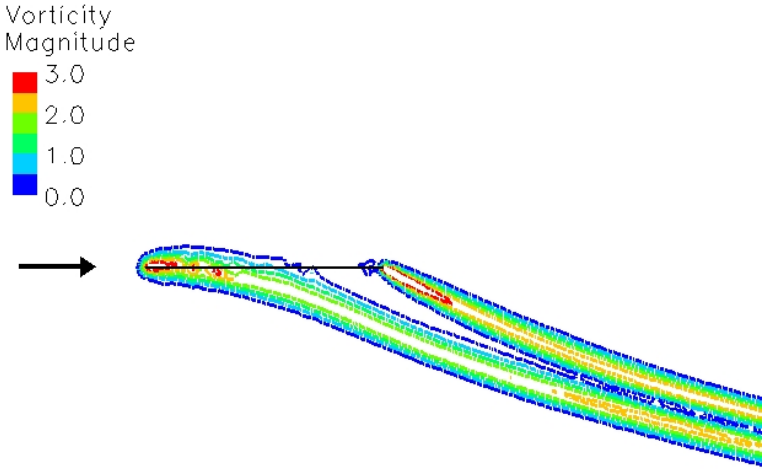

(b) Incompressible Solution

Figure 32: Vorticity contours for a uniform source disk in forward flight on a fine grid.

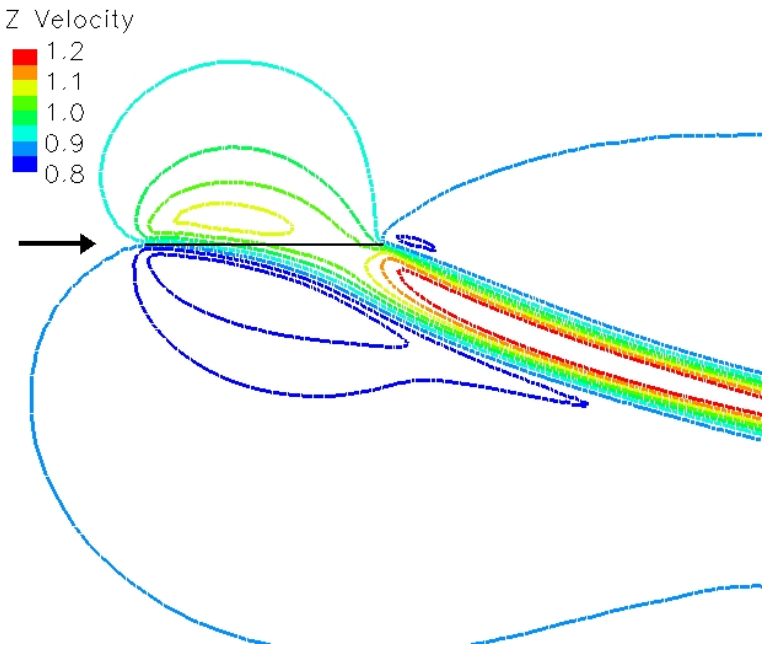

(a) Compressible Solution

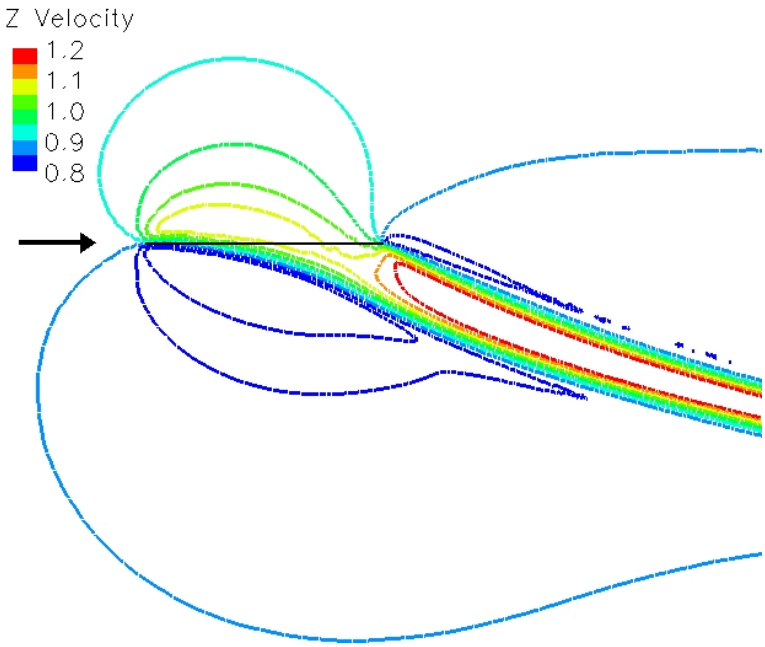

(b) Incompressible Solution

Figure 33: Normal velocity contours for a uniform source disk in forward flight on a fine grid.

model is found to significantly over predict the pressure at the center of the disk as a result of the uniform loading assumption. The linear model correlates well with the experiment, since it uses a more realistic loading. The streamlines predicted by the two results are plotted in Figure 35. The uniform pressure actuator disk induces a larger downwash over most of the disk area. When the linearly varying load is applied, the rotor downwash is primarily concentrated at the disk tips. An interesting aspect of the linearly varying load is that very little rotor downwash is observed in the center of the disk as a result of the light disk loading in this region.

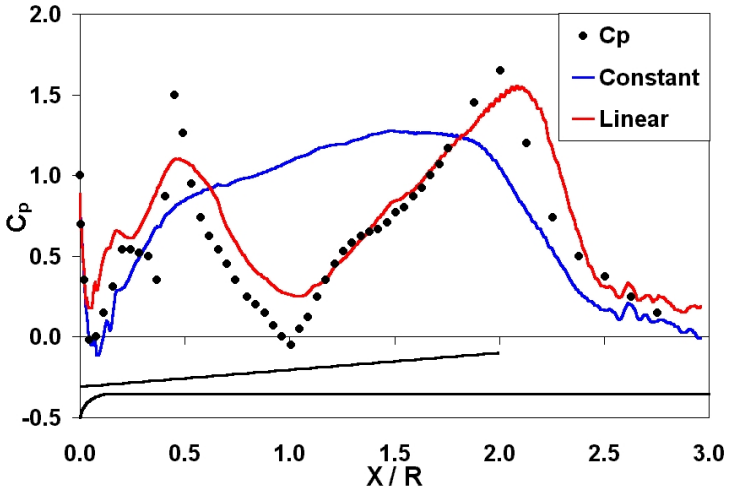

Figure 34: C_p distribution for the GIT configuration with a pressure jump actuator disk.

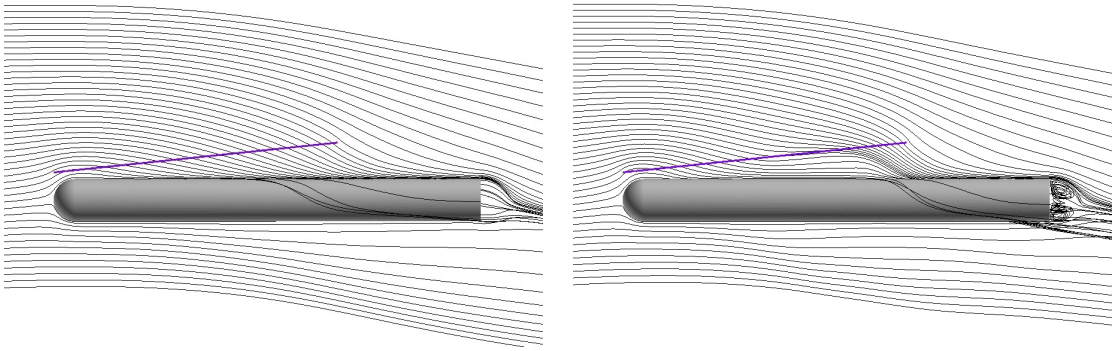

(a) Uniform Loading (b) Linear Loading

Figure 35: Streamline comparison for the GIT configuration with a pressure jump actuator disk.

Uniform and linear loading results were also obtained for the GIT configuration with a source-based actuator disk. Since the source-based actuator disk is easily integrated into the grid, the fuselage strut, rotor shaft, and hub were included for the source model computations. This grid utilized a general rotor wake refinement strategy which resulted in 1,890,497 nodes and 11,066,200 tetrahedra. The fuselage surface was paneled with 59,689 triangular faces. The source-based actuator disk cases utilized the incompressible option in FUN3D, since this is the preferred flow option for predicting fuselage aerodynamics at low Mach numbers. The coarse source distributions had 100 radial by 720 azimuthal sources. The fine source grid doubled the number of radial sources. Further refinement in either the azimuthal or radial direction had no effect on the solution.

The centerline pressure coefficient distributions are shown for both loading models in Figure 36. Once again the uniform distribution is over predicting the pressure in the hub region. However, the uniform source result differs from the pressure jump actuator disk due to the influence of the rotor shaft and hub. The linear model does a good job of predicting the low pressure in the hub region, but fails to exhibit the pressure peaks that were seen in the pressure jump disk model. The number of disk sources was doubled for the linear model to see if the peak pressure loss was a result of a coarse source distribution. The surface pressure in the vicinity of the disk tips was observed to change, but the additional refinement had no effect on the peak pressure. The presence of the stationary rotor shaft appears to be the primary reason for the loss of peak pressure. The blade element loading was observed to recover the peak pressures when the rotor shaft and hub were present, so the difference in the linear loading pressure coefficient trends was not pursued further.

The pressure coefficient contours in symmetry plane of the configuration are shown in Figure 37. The uniform model clearly shows an increased pressure under the hub when compared with the linear model. The low pressure region above the uniform loaded actuator disk also appears to be more uniformly distributed. The linear model shows the low pressure regions to be concentrated at the tips of the actuator disk. The constant model also shows signs of an increased rotor downwash effect, since the energized rotor wake creates a high pressure region on the fuselage strut at a lower position than observed with

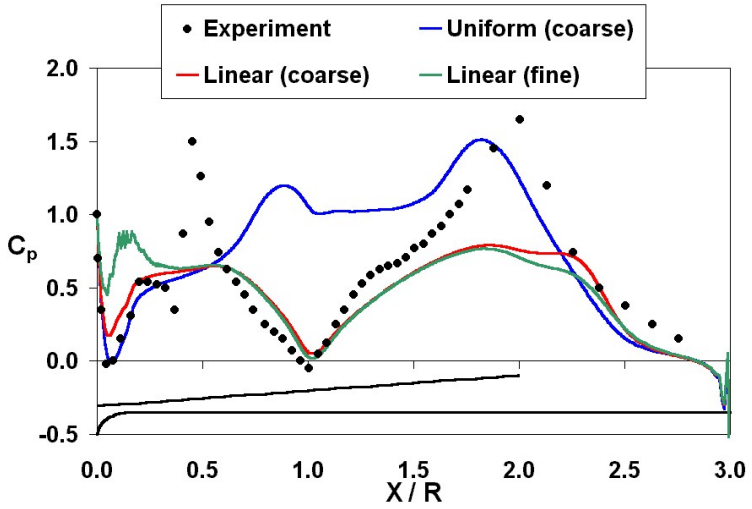

Figure 36: C_p distribution for the GIT configuration with a uniform and linear source based actuator disk.

the linear loading model.

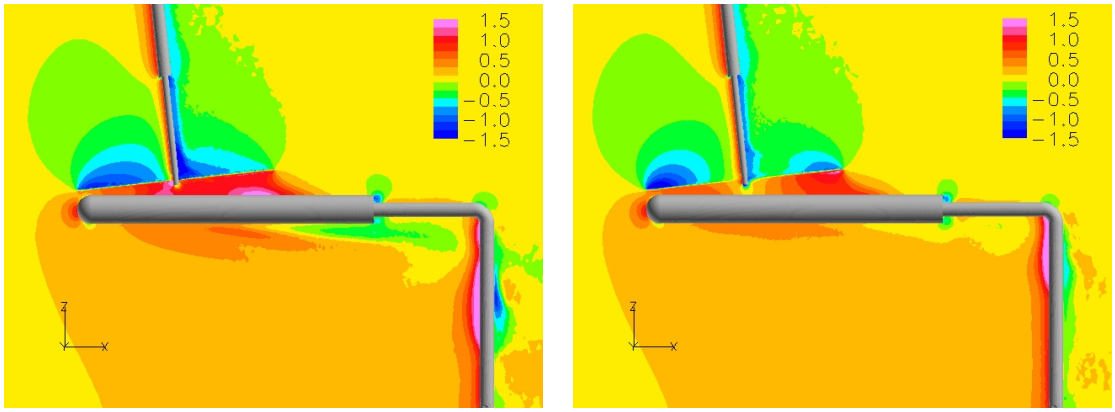

(a) Uniform Loading (b) Linear Loading

Figure 37: C_p contours for GIT configuration with a uniform and linear source based actuator disk.

Visualization of the vorticity generated by the linear loading model is shown in Figure 38. A clear vortex ring is seen around the tip of the actuator disk. The effects of numerical diffusion in the scheme are also apparent, since only a ring is visible and not a cylindrical wake. However, if the magnitude of the contour was reduced, more of the vortex wake would become visible. The other clear feature of the actuator disk wake is the roll up of the tip vortex that occurs in forward flight. This tip vortex is the result of the differential pressures of the actuator disk, which acts as a pseudo lifting surface or wing. The resulting

structure is similar for the constant model.

The tip vortex roll up is symmetric for both the constant and linear models since the loading does not vary by azimuth for these simple models. This is clearly apparent in Figure 39 showing the vorticity contours at the X=2.0 plane. This slice is taken at the rear tip of the actuator disk, which is why a strong vorticity region is located above the fuselage. The vortex sheet from the forward portion of the disk still exists as seen by the contours located under the fuselage that extend out to the tip roll up.

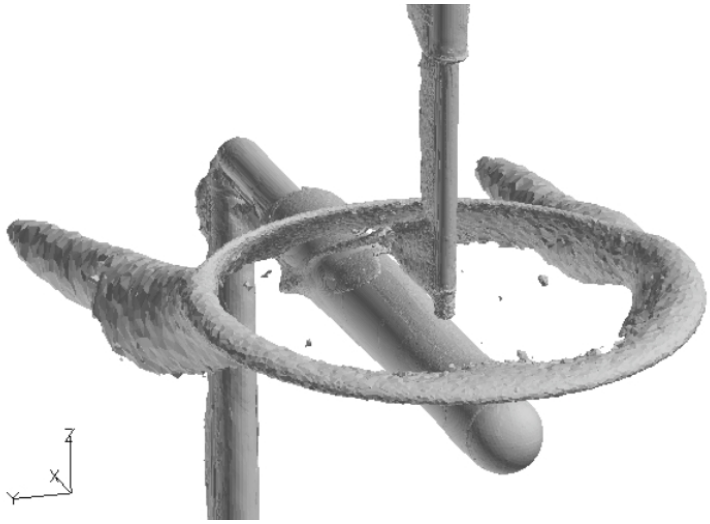

Figure 38: GIT vorticity iso-surfaces with a linear actuator disk.

5.4.2 ROBIN with a Uniform and Linear Disk Loading

The ROBIN fuselage with the approximated strut was tested with the pressure jump actuator disk model and compared to Run 25, Point 148 from the Freeman and Mineck experiment [9]. The advance ratio for this case is $\mu = 0.15$, which corresponds to a free stream Mach number of $M_{inf} = 0.087$. The fuselage angle of attack with respect to the free stream was 2.86°. The rotor shaft was tilted forward 2.00° with respect to the fuselage reference line. The actuator disk was defined in the shaft plane and did not account for the 20% cutout or the blade flap. The rotor thrust coefficient for this case was $C_T = 0.005$. The grid for this study had a total of 1.83 million nodes with 107,839 triangular faces on the fuselage. Once again, the compressible flow option was exercised for this investigation, since an incompressible pressure jump boundary condition was not available.

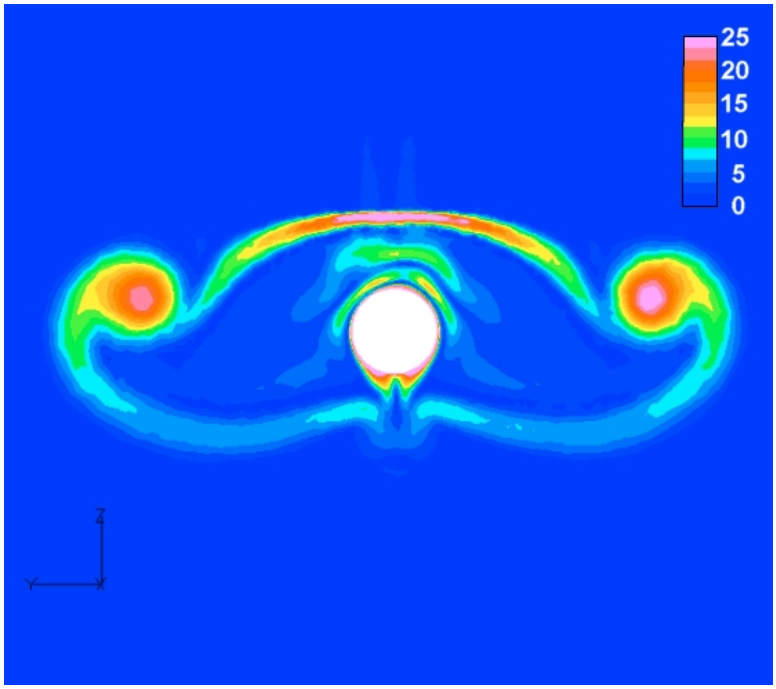

Figure 39: GIT vorticity contours at $X/R = 2.0$ with a linear actuator disk.

Pressure coefficient contours on the fuselage surface and symmetry plane are shown in Figure 40. The pressure over the nose region in both cases is found to exhibit a similar trend, indicating that the free stream flow is the dominant factor in this region. Similar to the GIT result, the constant distribution generates increased pressure over the hub region. However, it should also be noted that the large hub pressures are being exacerbated by the fact that the 20% cutout of the disk was not included. The increased tip load causes the linear model to predict a larger tail pressure.

An indication of how well each model is performing is obtained by comparing the computational result with the experimental pressure coefficient values as shown in Figure 41 and Figure 42. In the nose region (Figure 41(a)-(d) the uniform and linear distributions give similar results and are in good agreement with the experiment. Due to the proximity to the forward disk tip, the linear loading model tends to predict a slightly larger pressure over the nose region. In between the nose and pylon (Figure 41(e)-(g) the computational results remain similar to one another and in good agreement with the experiment. For the stations discussed so far the biggest difference between the two loading models occur over

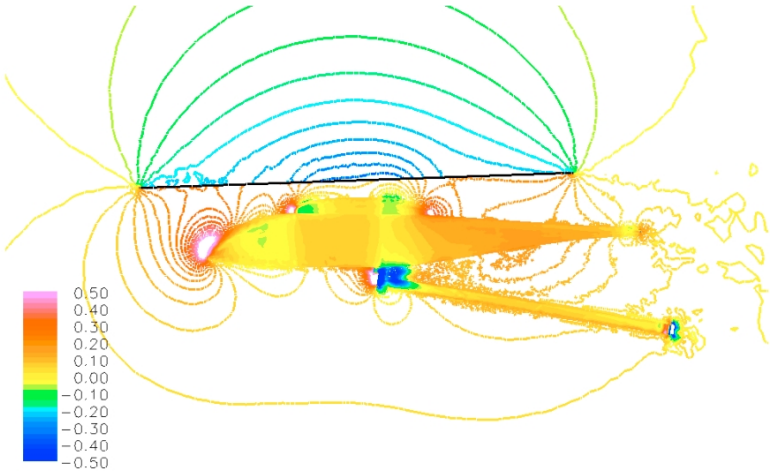

Uniform Actuator Disk

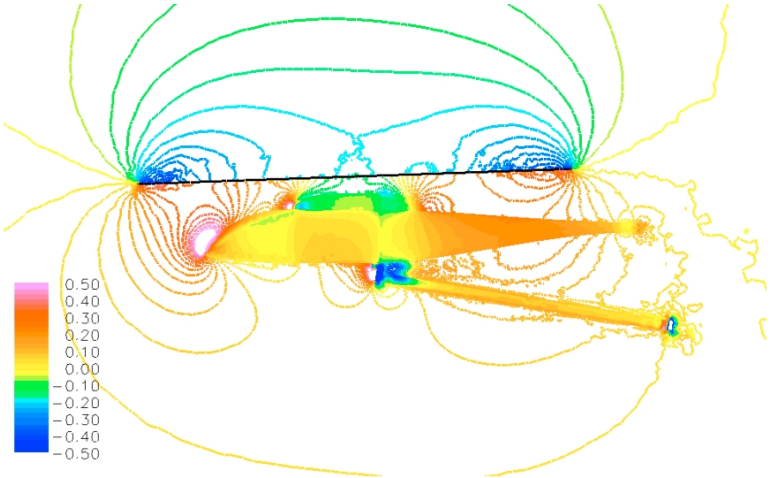

Linear Actuator Disk

Figure 40: C_p contours for ROBIN configuration with a pressure jump actuator disk boundary condition.

the side of the fuselage. The uniform loading begins to show larger pressures than linear model over the upper half of the fuselage in Figure 41(g).

Over the hub (Figure 42(a)-(d), the uniform model clearly over predicts the pressure and does not provide a good correlation with the experiment. In contrast, the linear model demonstrates an excellent correlation with the experiment, especially near the center of the disk (Figure 42(b). The tail sections (Figure 42(e)-(g) indicate that the linear model is over predicting the pressure, most likely since the cut-out was not modeled so that the source magnitude is lower than it should be. In this region the constant model shows a better trend compared to the experiment.

The inflow due to the simple actuator disk loading models was also investigated by comparing with experimental inflow measurements [19]. The computed and experimental inflow distributions are shown in Figure 43. It is clearly seen that neither loading model obtains a good correlation with experiment. However, each model is predicting the inflow reasonably well over portions of the disk. Both models show the upwash over the forward tip of the disk. On the advancing and retreating sides of the disk, the linear model shows a stronger downwash similar to what is observed in the experiment. However, the constant model shows a better correlation with experiment at $\psi = 0$. The poor inflow correlation with the experiment over the aft region of the linearly loaded actuator disk is consistent with the poor experimental pressure coefficient trend over the tail of the ROBIN. Streamlines for both disk loading models are shown in Figure 44. The streamline trends are consistent with the disk inflow. The linear model generates a weak downwash over the aft portion of the disk, so the streamlines show predominately streamwise flow over the tail of the configuration. The constant model shows that the rotor wake is impacting the tail.

5.5 Blade Element Loading Model

5.5.1 GIT with a Blade Element Disk Loading

The blade element loading model was verified using the GIT configuration at an advance ratio of μ=0.1. The GIT grid utilized in this case was the same as the one used for testing the uniform and linear loading actuator disk. Unless otherwise noted, all of the

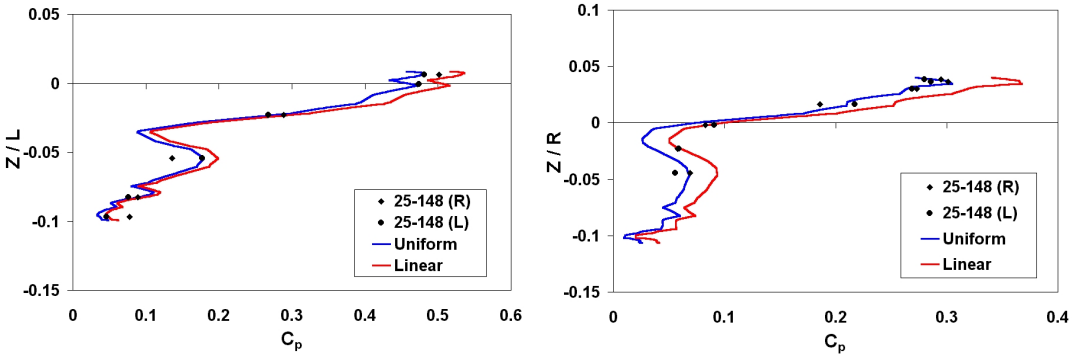

(a) X/L = 0.0517

(b) X/L = 0.0941

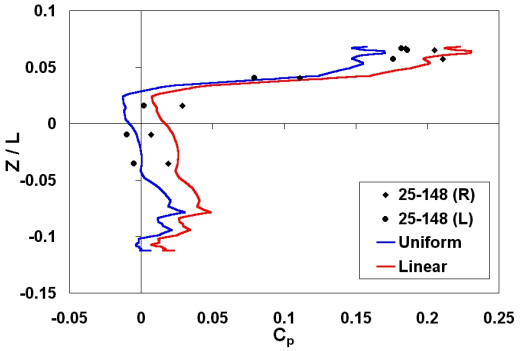

(c) X/L = 0.1451

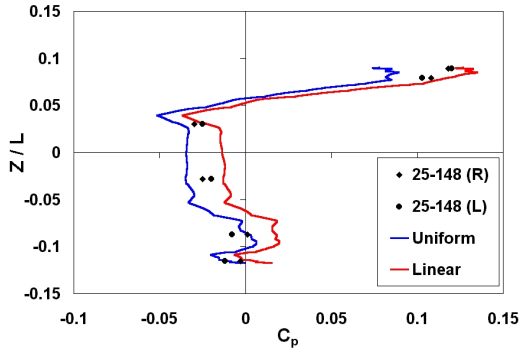

(d) X/L = 0.2007

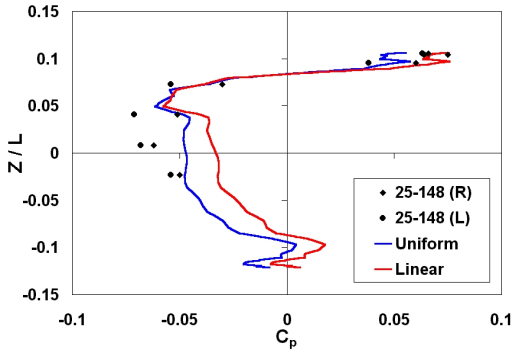

(e) X/L = 0.2562

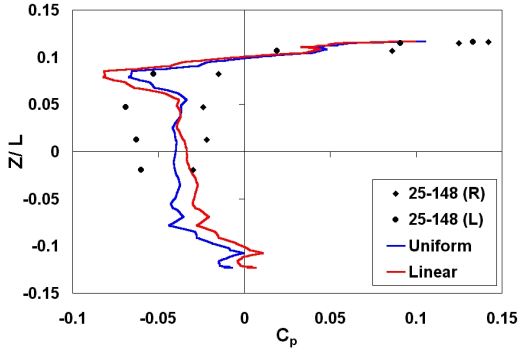

(f) X/L = 0.3074

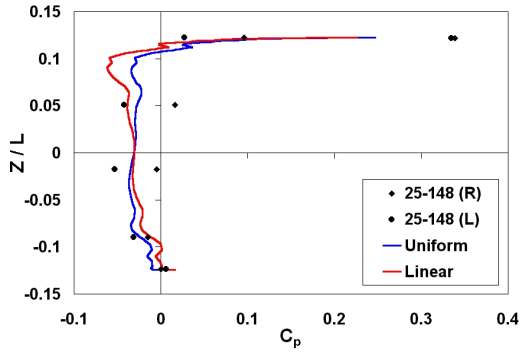

(g) X/L = 0.3498

Figure 41: ROBIN front cross-section C_p due to the uniform and linear actuator disk.

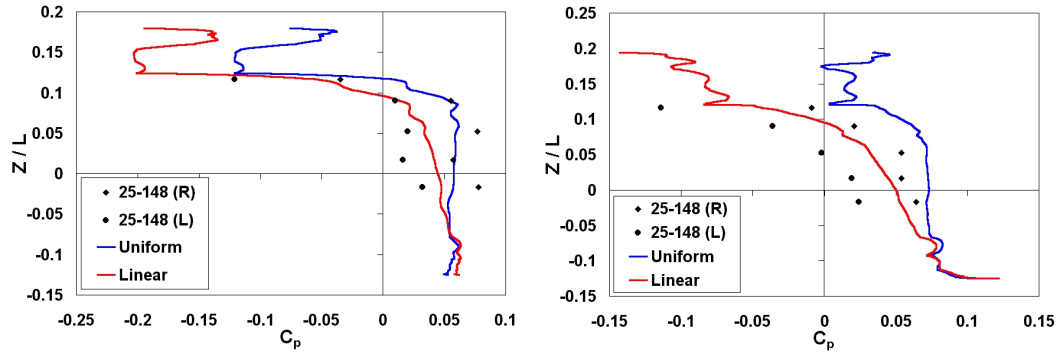

(a) X/L = 0.4669

(b) X/L = 0.6003

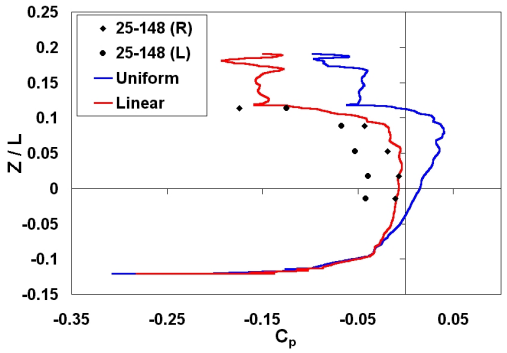

(c) X/L = 0.8809

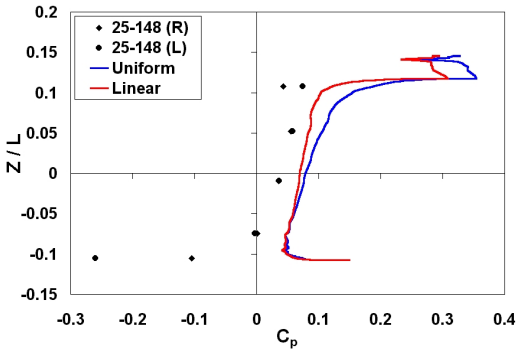

(d) X/L = 1.0008

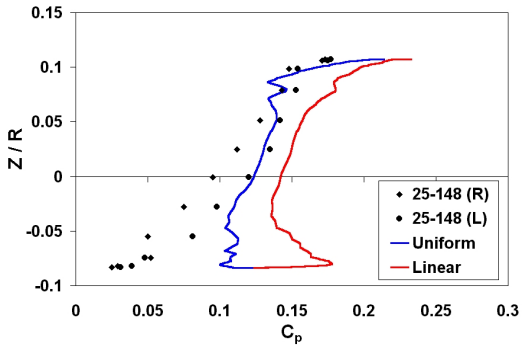

(e) X/L = 1.1619

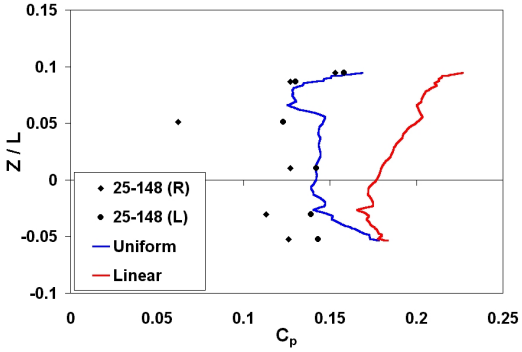

(f) X/L = 1.3455

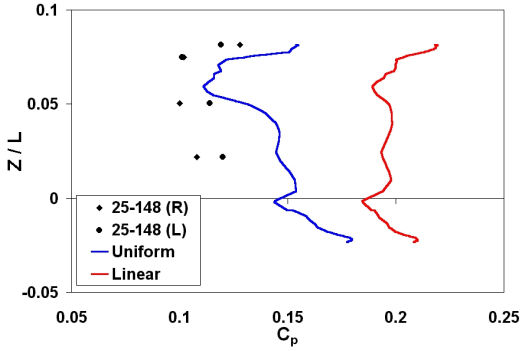

(g) X/L = 1.5305

Figure 42: ROBIN rear cross-section C_p due to the uniform and linear actuator disk.

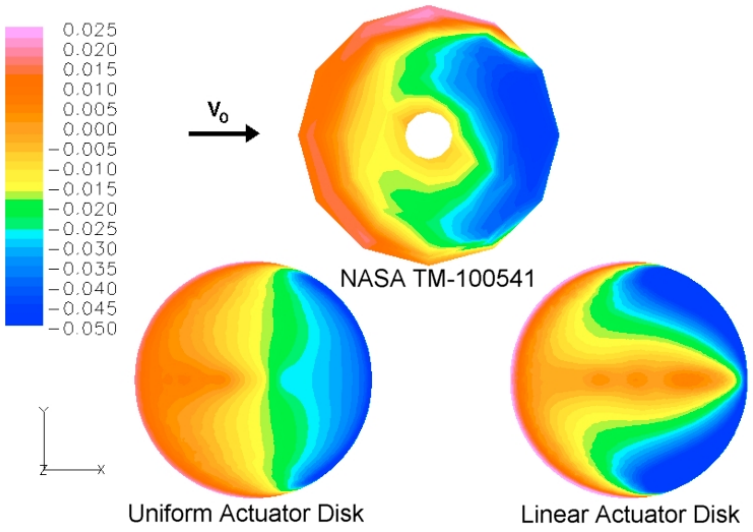

Figure 43: ROBIN downwash measurements through the rotor disk

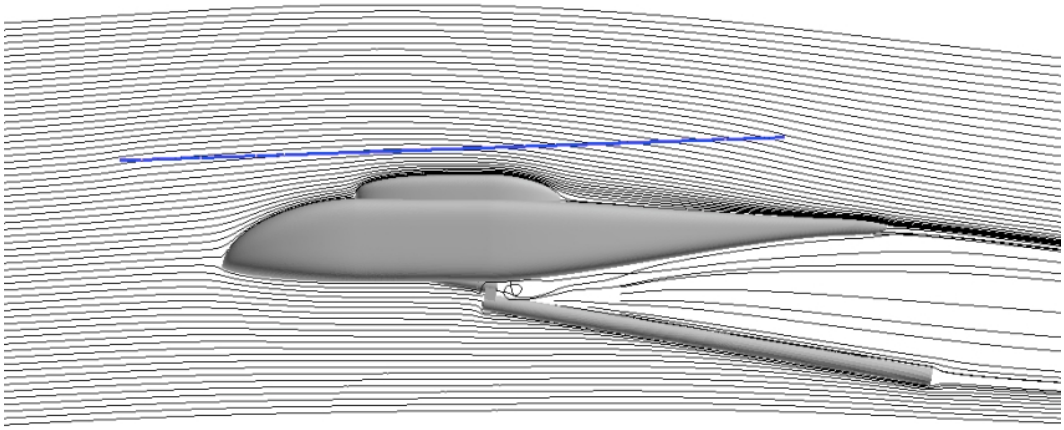

Uniform Actuator Disk

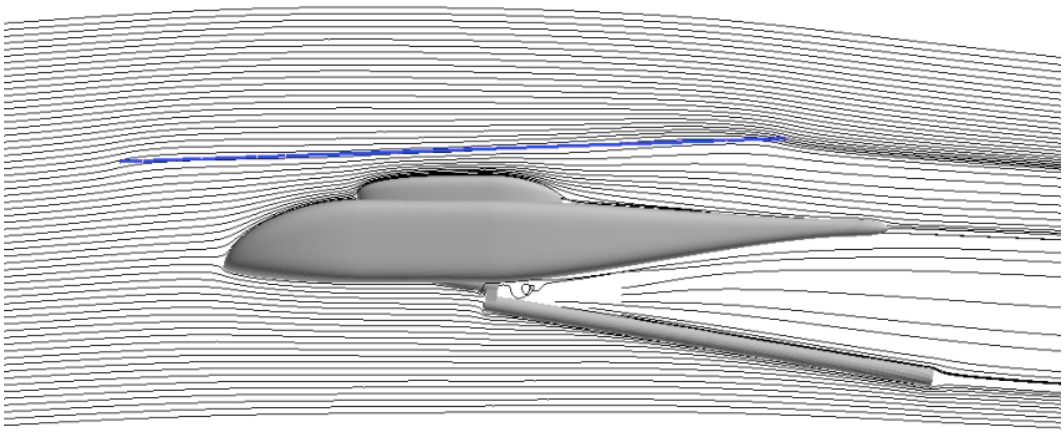

Linear Actuator Disk

Figure 44: Streamlines for the ROBIN configuration (μ=0.15).

blade element cases utilize the incompressible option in FUN3D. A 200 x 720 source grid was utilized for the blade element computations, since this distribution was found to generate a source independent solution. The advantage of this loading model is that it adjusts to the computed inflow, providing a more realistic disk loading. One of the biggest benefits of the blade element model is that flow asymmetry in forward flight develops naturally. Figure 45 shows the vorticity iso-surfaces generated by the blade element model. Unlike the linear model, the blade element model generates different tip vortex rollup behavior on the advancing side and retreating side. This is more clearly illustrated in Figure 46, showing the vorticity contours in the X=2.0 plane. The advancing blade (left side of figure) generates a stronger tip vortex rollup, which descends faster than the retreating blade rollup.

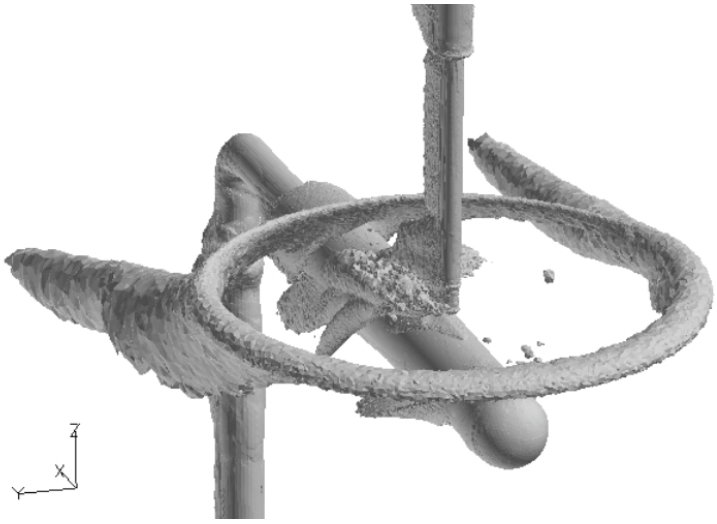

Figure 45: GIT vorticity iso-surfaces with the blade element model.

Another advantage of the blade element method is that details of the blade can be included in the model to provide higher levels of fidelity in the computation. Of course this also means that to take full advantage of the method more information has to be provided to the solver. Two particular features of the model were examined in detail, the blade flap and the rotor drag force effect.

Four cases were considered for the blade flap comparison by switching on and off two model inputs: flap displacement and flap velocity. The flap displacement represents

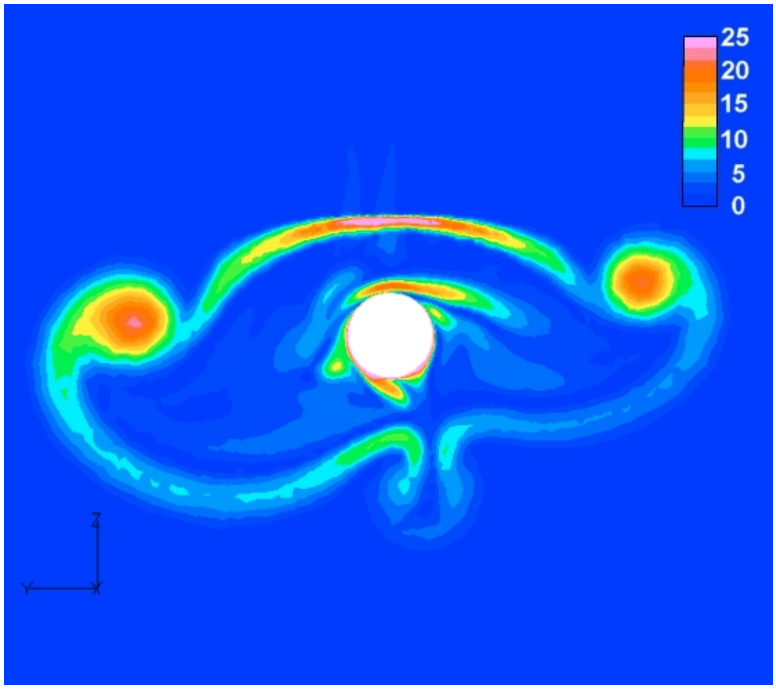

Figure 46: GIT vorticity contours at x=2.0 with the blade element model.

whether the sources are distributed in the plane normal to the rotor shaft or moved above ($\beta > 0$) or below ($\beta < 0$) the plane. Turning on the flap displacement has two effects:

1. The location where the sources act on the flow changes.

2. The orientation of the blade section changes, altering the computed inflow angle.

The first effect has the largest influence on the flow, since the location of the source is changed. However, the second effect could also become significant for large flap angles. Activating the flap velocity adds the contribution of the dynamic flap motion to the computation of the velocity normal to the blade section as shown in Equation 44.

The centerline pressure coefficient distributions computed for the four flap cases are shown in Figure 47. Disregarding both the displacement and velocity effect matches the trend of the experimental measurements, but the forward and aft peak predictions are off by $\Delta C_p = -0.33$ and $\Delta C_p = -0.65$, respectively. When the flap displacement is incorporated into the model the difference in the aft peak prediction improves to $\Delta C_p = -0.44$. Since the blade flaps down at $\psi = 0$ (aft peak), the sources move closer to the fuselage and an increase in the aft surface pressure is obtained. The flap velocity is observed to have a

much stronger effect on the result. Both cases that included the flap velocity in the model obtained a significantly reduced forward peak prediction ($\Delta C_p = -1.0$). However, better agreement in the range $0 < X/R < 0.3$ is obtained. When all of the flap effects are included the aft pressure peak is overpredicted ($\Delta C_p = 0.44$), but the correlation in the range of $1.0 < X/R < 1.75$ is better than the other models.

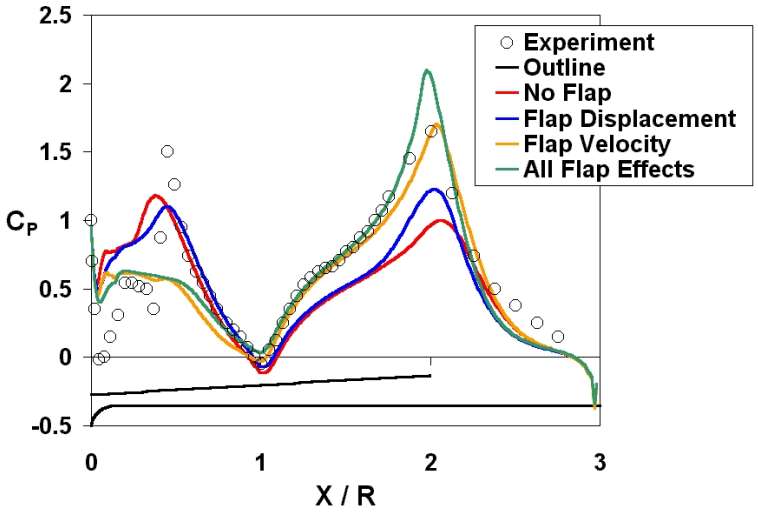

Figure 47: GIT flap contribution comparison for the blade element model.

Including both the flap displacement and flap velocity is considered to be most physically accurate representation, so this case served as the baseline for testing the effect of the blade section drag force. It is interesting to note that the drag force is frequently neglected in a boundary-condition-based method, since it can not be applied as consistently as it can in the source-based approach and can lead to nonphysical solutions [50]. Figure 48 shows the effect of adding the rotor drag effect. Including the drag force reduces the computed surface pressure coefficient by approximately 0.15 over the inner 80% of the rotor disk. Between $X/R = 1.0$ and $X/R = 1.8$ the computed pressure coefficient is within 0.05 of the experimental value. The primary influence of the blade section drag force is on the wake velocity as shown in Figure 49. The effect of the drag force is to induce a small reduction the angle of attack, which is the primary reason for the change in the centerline pressure coefficient distribution.

Two questions arise as a result of this study. The first is the over prediction of the aft

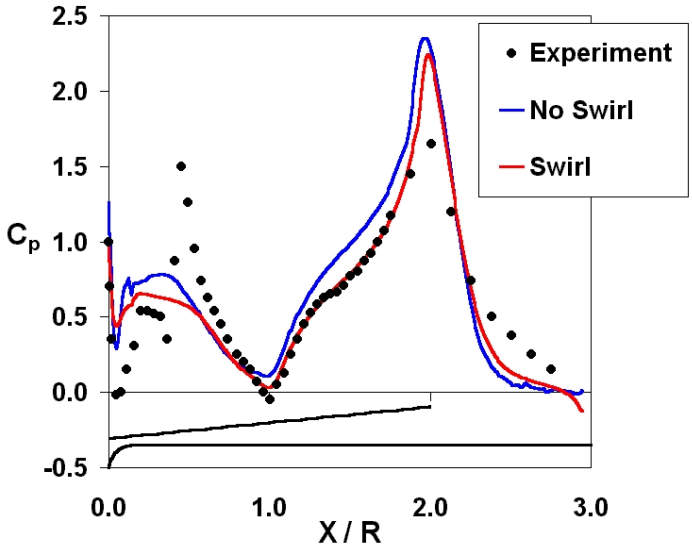

Figure 48: GIT effect of the drag force on the blade element model.

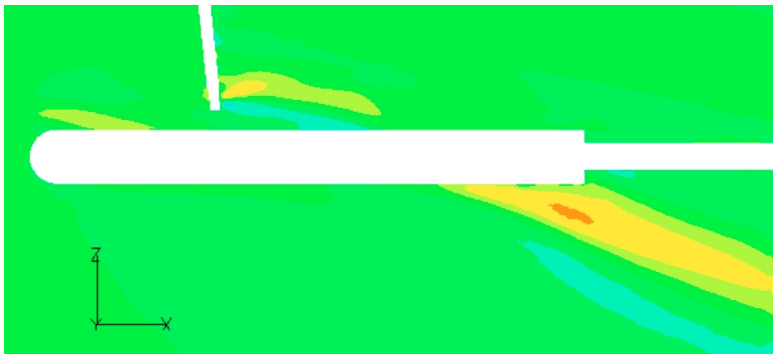

No Swirl

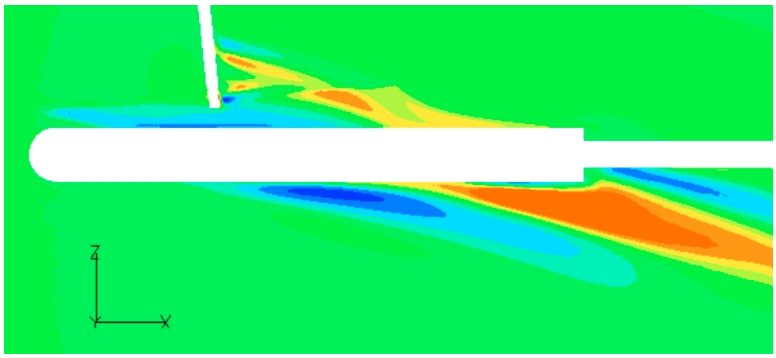

Swirl Included

Figure 49: GIT effect of the drag force on v velocity in the y=0 plane.

pressure peak. This may be explained by the fact that no tip corrections are applied to the blade element method to account for the decrease in lift at the tip. Rajagopalan and Lim [45] point out that three-dimensional flow effects occur for two different reasons:

1. Tip vortex induced velocity

2. Pressure equalization at the blade tip

The tip vortex effect is accounted for by the solver simply by the fact that the actuator disk generates a tip vortex sheet. However, pressure equalization can not occur naturally, since the blades are not physically modeled. Chaffin and Berry [49] also applied a tip correction by linearly decreasing the load over the outboard 5% of the blade.

The second question is why the more physically correct flapping model fails to predict the forward peak pressure. This appears to be a result of the steady state assumption used to derive the actuator disk. Examination of the unsteady experimental surface pressures in Brand's dissertation [11], shows that the tip vortex causes significant pressure excursions on the fuselage surface. This implies that the forward peak is primarily an unsteady effect, which invalidates the steady-state actuator disk assumption. A simple two-dimensional analysis helps to reinforce this point. Figure 50 shows the resulting blade downwash resulting from a line vortex and a point vortex shed from the blade tip. The line vortex generates a relatively smooth downwash across the disk similar to the result expected from a vortex sheet. If the vortex exists in discrete elements, as it would for a helical vortex wake, the downwash on the blade exhibits a strong pulse whenever it passes over the vortex. Therefore, in cases where there is a strong blade vortex interaction, the actuator disk model can not be expected to adequately resolve the flow. Zori, et. al. [46] also failed to capture the forward peak when including the blade flap effect. Park et. al. [76], as well as Lee and Kwon did not include the blade flap and obtained a result similar to the shaft-plane-aligned disk described above. Mavris did observe the forward peak in his dissertation [42], as he used an unsteady free-vortex-wake method.

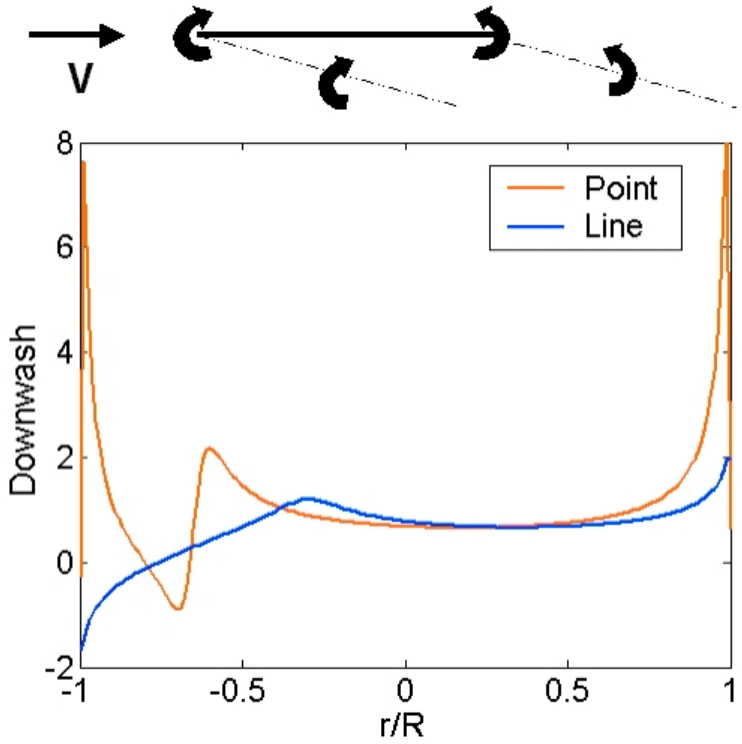

Figure 50: Two dimensional blade downwash resulting from a point and line vortex.

5.6 Actuator Blade Model

The actuator blade model was tested on the GIT configuration, using the same grid as the source-based actuator disk models. The primary focus of this investigation was to verify that the actuator blade model is capable of providing useful unsteady results. The actuator blade model was solved using compressible flow, since initial transients were found to drive the incompressible solution unstable. Increasing the number of subiterations during the solution start-up may potentially remedy this problem. The actuator blade sources distribution for this case was 2 blades by 200 radial by 20 chordwise.

The force and moment histories are shown as a function of blade azimuth in Figure 51 and Figure 52, respectively. The force history demonstrates the importance of accounting for unsteady effects. When the blade passes over the fuselage, a large fuselage down force is observed. The moment history shows that the fuselage experiences a significant yawing moment that switches from nose left to nose right during the blade passage. If this were a real configuration these strong blade passage effects would have a significant influence on

handling qualities and vibration.

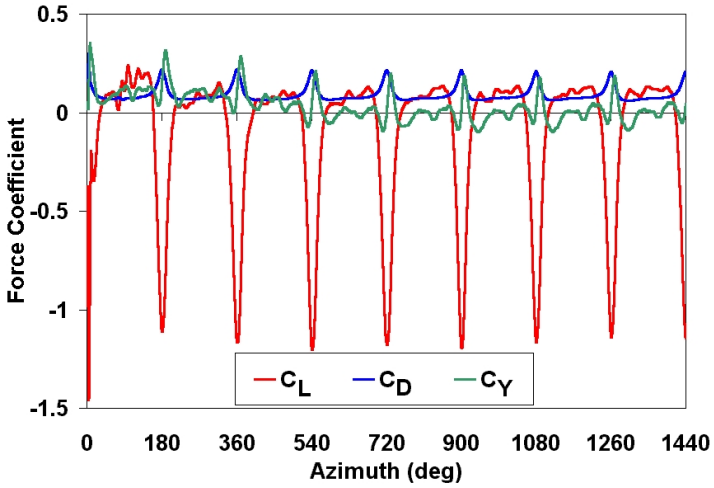

Figure 51: GIT fuselage force history with actuator blade model.

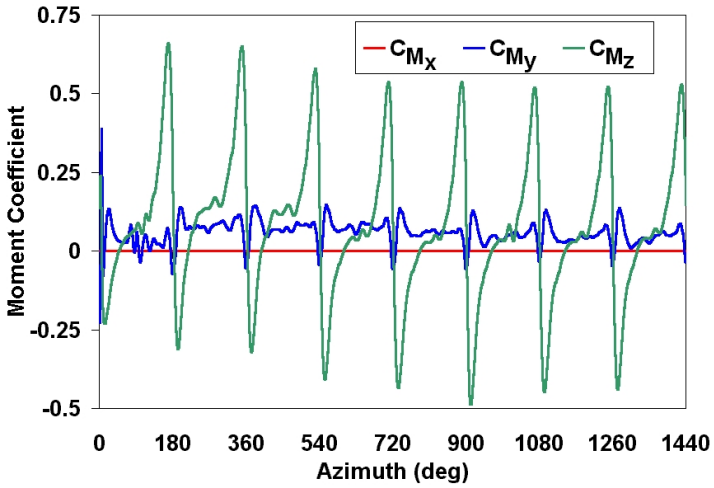

Figure 52: GIT fuselage moment history with actuator blade model.

Figure 53 shows the variation of the upper centerline pressure coefficient as a function of blade azimuth. The effect of the blade passage is clearly shown. One interesting feature of this result is that the forward peak is stronger and sharper than the rear peak. The increased magnitude is a result of the blade passing closer to the fuselage. The interaction between the fuselage and the tip vortex is also visible, especially over the rear of the configuration. The influence of the tip vortex shows up as a ripple in pressure that propagates downstream as the blade rotates. The rear vortex continues to propagate to the end of the fuselage, but

the forward vortex influence appears to dissipate during the blade passage. Vorticity isosurfaces are shown in Figure 54. The helical structure of the rotor wake with the actuator blade model is yet another indicator that a time varying behavior is being modeled.

5.7 Overset Verification

5.7.1 Static Overset

The static overset implementation was tested using a steady state supersonic ramp test case that was designed to be similar to the case used to verify the overset implementation in USM3D [112]. Here, a ramp angle of 14.51° is utilized, and the exact pressure ratio across the shock is known to be $\frac{p_2}{p_1} = 2.4027$ [113]. The shock angle for this case is computed to be $\theta_{shock} = 36.4133°$ [113]. The grid spacing used in the current study is denser than the USM3D study because node-based schemes (FUN3D) require more grid nodes than cell-centered schemes (USM3D) to obtain the same level of accuracy. In general, the number of nodes in a node-based scheme should be equal to the number of tetrahedra in a cell-based scheme for equivalent accuracy. The single grid contained 1,258,779 nodes and 7,190,812 tetrahedra. The overset version of the grid had a total of 1,535,289 nodes and 8,729,654 tetrahedra, where 691,040 nodes come from the bottom grid and 844,249 nodes belong to the top grid. The compressible flow option was required for this test case, since supersonic flow was being modeled.

The Mach contours for the single and overset grids are shown in Figure 55. The transfer of information across the overset grid boundaries is observed to cause negligible distortion to the shock, verifying that the overset implementation is working properly.

The pressure ratio is also plotted along the ramp surface in Figure 56a and along the line $z = 0.50$ in Figure 56b. In each case the pressure jump is found to match the exact value of 2.4027. Figure 56b also shows that the location of the shock ($X_{shock} = \frac{0.50}{\tan \theta_{shock}} = 0.6779$) is well predicted. The agreement with the known values provides an additional validation of the FUN3D flow solver.

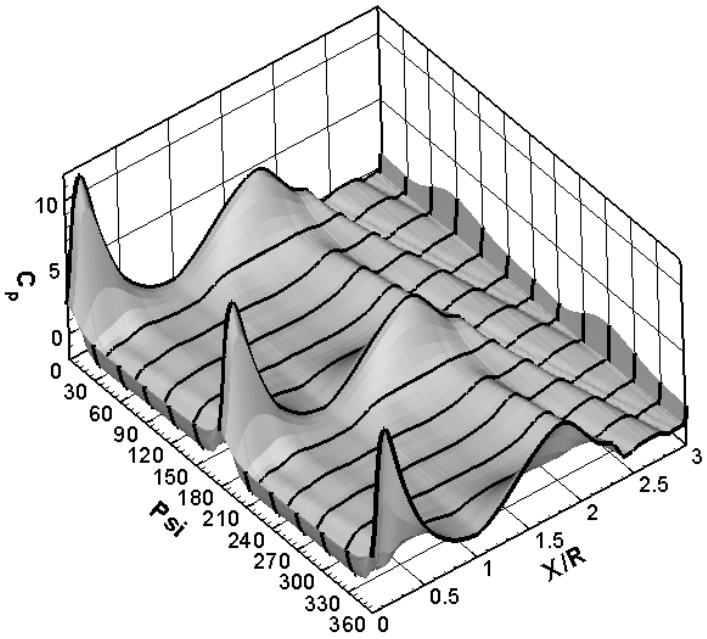

(a) Front View

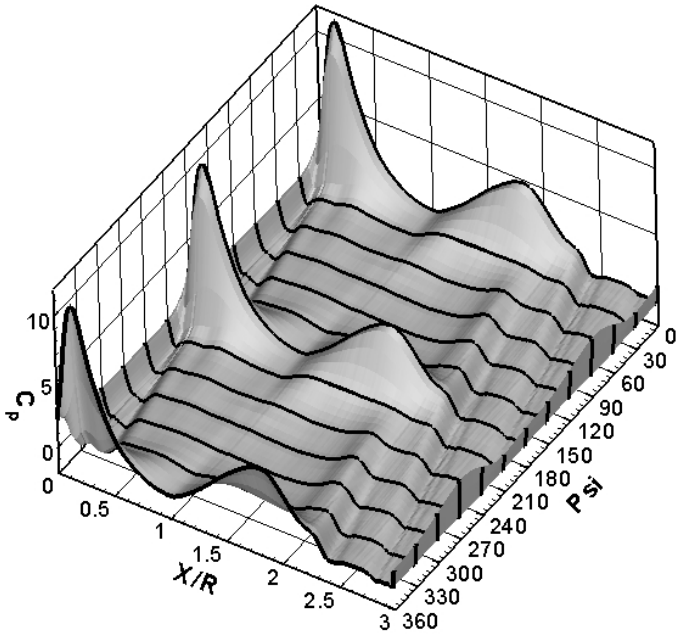

(b) Rear View

Figure 53: GIT upper centerline unsteady Cp variation with the actuator blade model.

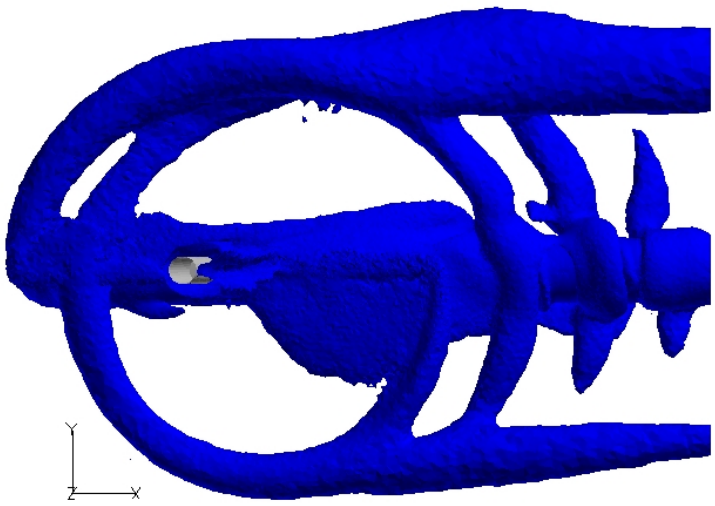

Figure 54: GIT vorticity iso-surfaces with actuator blade model.

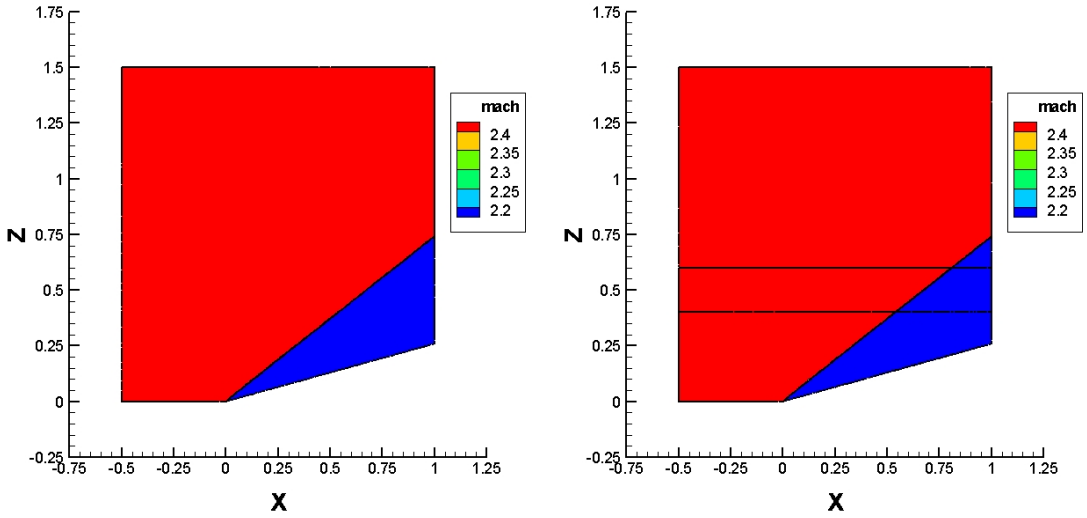

(a) Single Grid (b) Overset Grid

Figure 55: Mach contours for a supersonic ramp.

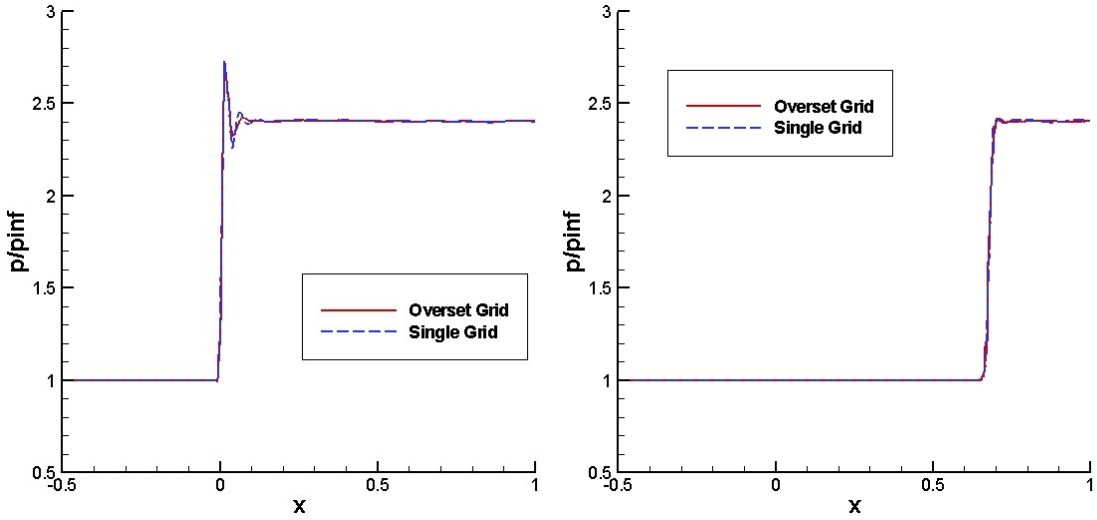

(a) Surface Distribution (b) Line through $z = 0.50$

Figure 56: Mach contours for a supersonic ramp.

5.7.2 Dynamic Overset

The dynamic overset implementation was also tested using the GIT configuration without the strut or hub modeled. These results were presented at the 31^{st} European Rotorcraft Forum [77]. The GIT configuration has a teetering hub that is not articulated to allow pitch input, enabling both blades to be modeled with one dynamic grid. Therefore, this investigation used one stationary fuselage grid and one dynamic rotor grid. The fuselage grid had 1,870,639 nodes with 36,119 nodes on the fuselage. The blade grid consisted of 420,709 nodes and had total 15,784 nodes on the blade surfaces. Therefore, the combined grid had 2,291,348 nodes and 51,903 surface nodes. The dynamic overset rotor implementation was verified with the compressible, inviscid equation set in FUN3D. The RANS equations were not utilized in an effort to reduce the number of grid points for this preliminary computation.

The most important aspect of a dynamic overset solution is that the flow is successfully transferred across the overset boundary at each timestep. This can be affirmed by examining contours of the flow variables in the overlap region to ensure that they are consistent. The pressure and u velocity contours are shown in the overlap region for the current case in Figure 57 and Figure 58, respectively. Minor differences exist between the two predictions,

but overall the contours are in good agreement with each other, indicating that the flow information is being transmitted across the boundaries correctly.

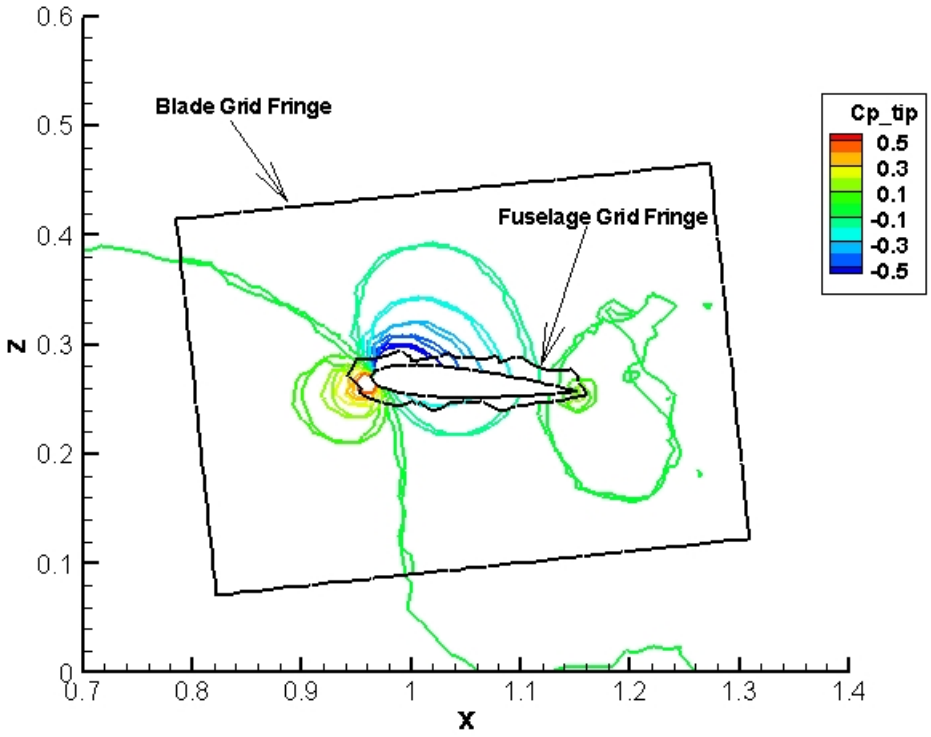

Figure 57: C_p in the overlap region for the GIT configuration.

Of course to verify that result is reasonable, it is also necessary to compare with experimental data. Time-averaged surface pressure coefficient distributions are shown for the top, right, and left centerlines in Figures 59, 60, and 61, respectively. The upper centerline shows a fairly good correlation with the data. The only exceptions are at the forward peak, where the pressure is under predicted, and at the aft peak where the pressure is over predicted. The forward peak appears to suffer due to the diffusion of the previous tip vortex. The diffusion also appears to cause the vortex to lag the experimentally observed vortex, which is indicated by the leftward shift of the computed forward peak compared to the experimental result. The aft vortex over prediction may be a result of the rotor shaft not being present, allowing the flow to go undisturbed and possibly increasing the rotor inflow at the tip.

The right side distribution also demonstrates a good correlation with the experiment.

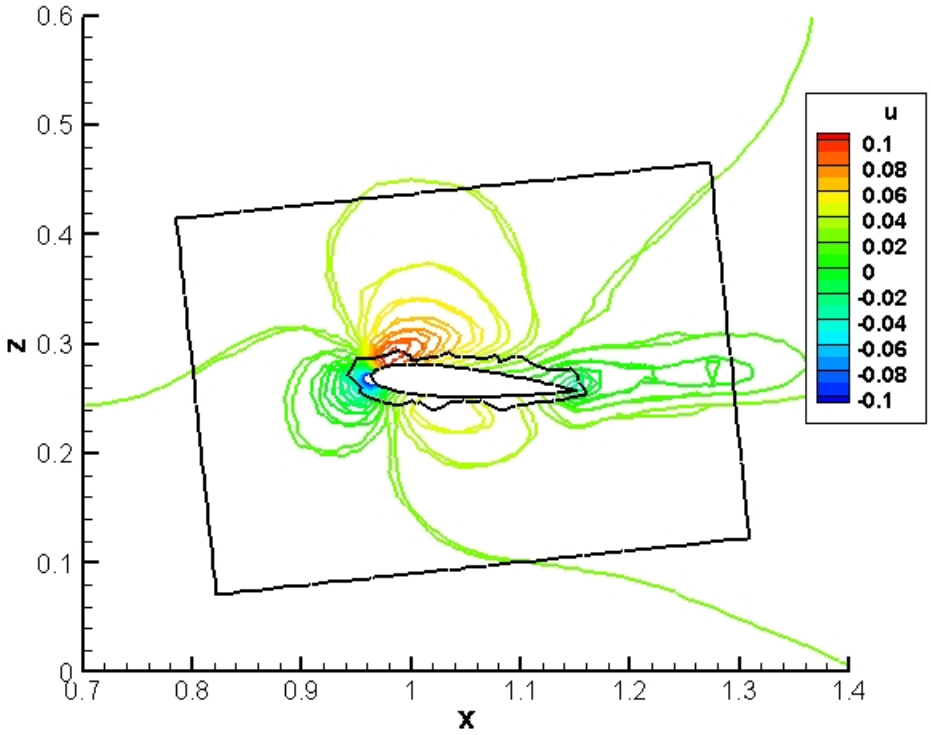

Figure 58: U velocity in the overlap region for the GIT configuration.

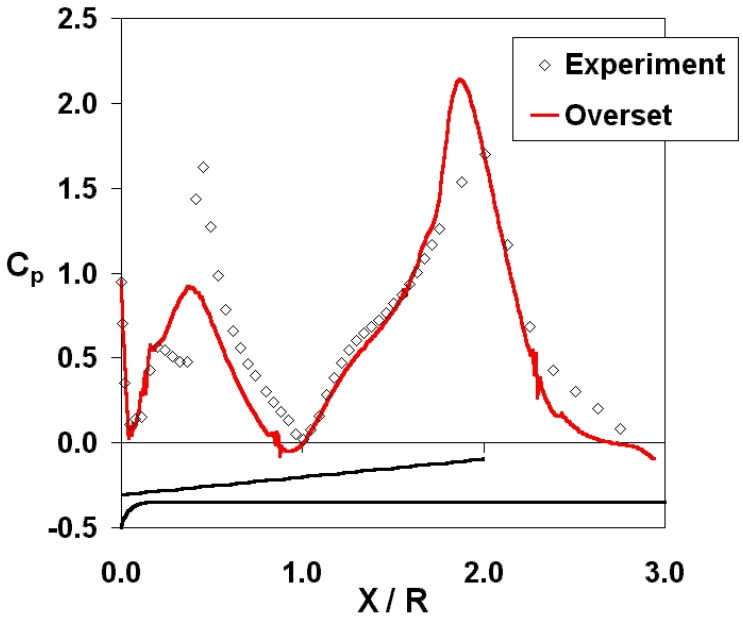

Figure 59: GIT overset time averaged upper centerline C_p distribution.

The previous vortex once again shows signs of diffusion. The aft vortex appears to cause a much stronger reduction in pressure than observed in the experiment ($\Delta C_p = -0.7$). There are potentially two mechanisms at work here. The first is the over prediction of pressure seen on the top centerline and the second is that this case was run inviscid. If any separation is present over the side of the fuselage, the inviscid assumption would not be valid.

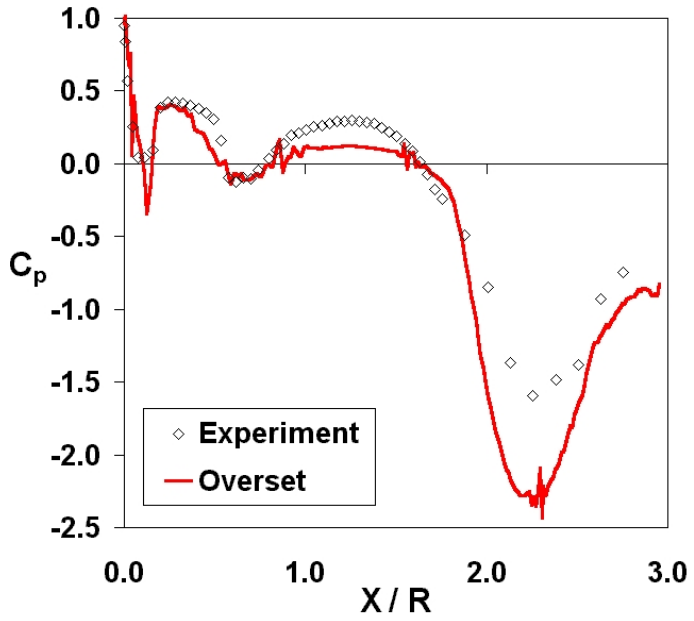

Figure 60: GIT overset time averaged right centerline C_p distribution.

The left distribution shows the general trend of the data, but overall has a much poorer correlation than the right centerline. On the left side a different mechanism may be at work than on the right. Here the vortex is sweeping over the fuselage unlike the right side where the vortex is colliding with the fuselage. This sweeping effect may also require modeling of the viscous flow over the fuselage to be correctly captured. The aft vortex influence also shows the same trend as the right, which again is likely due to the over prediction of the tip vortex strength and the inviscid flow assumption.

Examining the vorticity provides some insight into the pressure predictions. Figure 62 shows the vorticity iso-surface generated after three blade revolutions ($\psi = 1080°$). Over the forward half of the fuselage the current vortex and previous blade vortex are still present on both the left and right side of the fuselage. However, the vortex from 360° ago

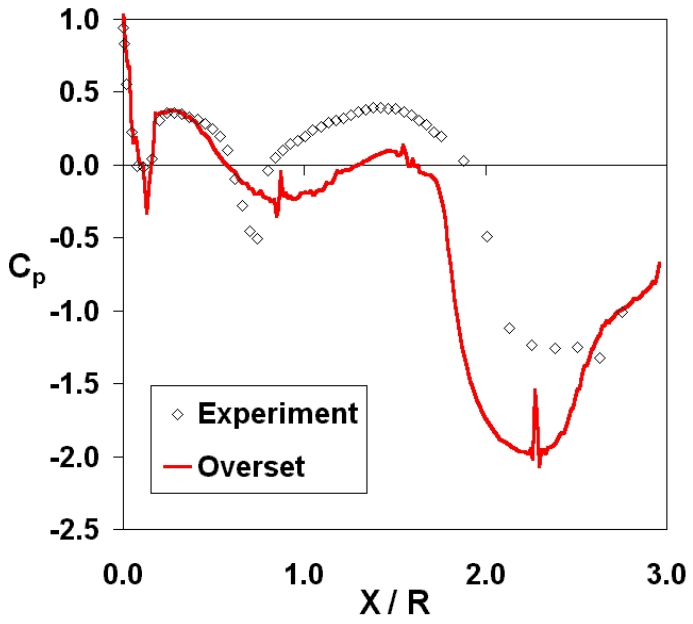

Figure 61: GIT overset time averaged left centerline C_p distribution.

is only visible on the left side. According to the wake visualization from Brand [11], this vortex dissipates due to its interaction with the fuselage. The fact that this vortex still exists on the left side is the likely reason the left side correlation is less accurate than the right side correlation. Over the aft portion of the fuselage, the tip vortex exists for a longer duration. Some vorticity is also seen to exist in the region near the aft vortex that is half a revolution old. This additional vorticity is derived from the root vortex of the blades and may be a source of the poor pressure correlation over the aft portion of the fuselage.

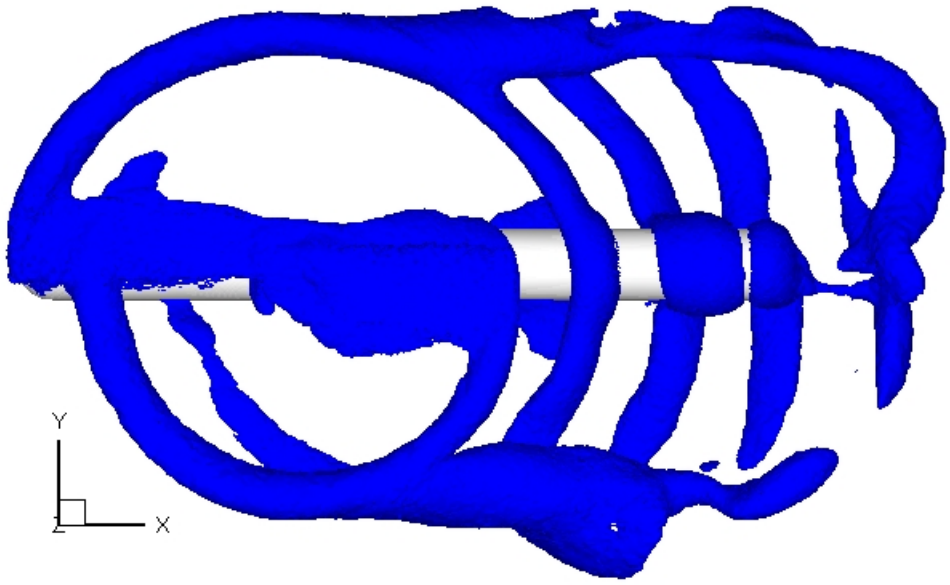

Figure 62: GIT overset vorticity iso-surface at $\psi = 1080°$ viewed from above.

CHAPTER VI

RESULTS

6.1 Dauphin Investigation

The Dauphin configuration was investigated as a subtask of the US-France MoA. Each of the three MoA participants on this task applied a different RANS-based CFD method to study the Dauphin aerodynamics. ONERA used a multi-block, structured solver (elsA), AFDD used an overset, structured solver (OVERFLOW), and GIT used an unstructured solver (FUN3D). Each of the partners attempted to utilize a grid size of approximately 7 million nodes, but computer memory limited the GIT grid to approximately 5 million nodes with 95 thousand surface nodes. The wall spacing for each of three methods was such that $y^+ < 1$. FUN3D was run using the incompressible flow option and elsA and OVERFLOW utilized a preconditioned compressible scheme. Details of the test conditions can be found in Chapter IV. Additional information related to the MoA investigation is presented in Renaud et al. [111].

The first stage of the investigation examined the flow over an isolated fuselage. The centerline pressure coefficient comparison of the three RANS methods is shown in Figure 63. The FUN3D result is consistent with its structured counterparts and there is generally good agreement between the CFD computations and the experimental data. Aft of the pylon the upper centerline computations differ by roughly $\Delta C_p = 0.1$ to 0.2 from the experiment. Since all three of the CFD methods consistently predict this shift, possible discrepancies between the computational geometry and the wind tunnel geometry are being investigated [111]. The lower centerline shows significant differences in the pressure coefficient near $X = 0.50$m, because the strut was not modeled in the initial comparison. Differences in the lower centerline experimental data are a result of taping the gap between the fuselage and strut in the F1 experiment.

To improve the consistency between the experimental geometry and the CFD model, the

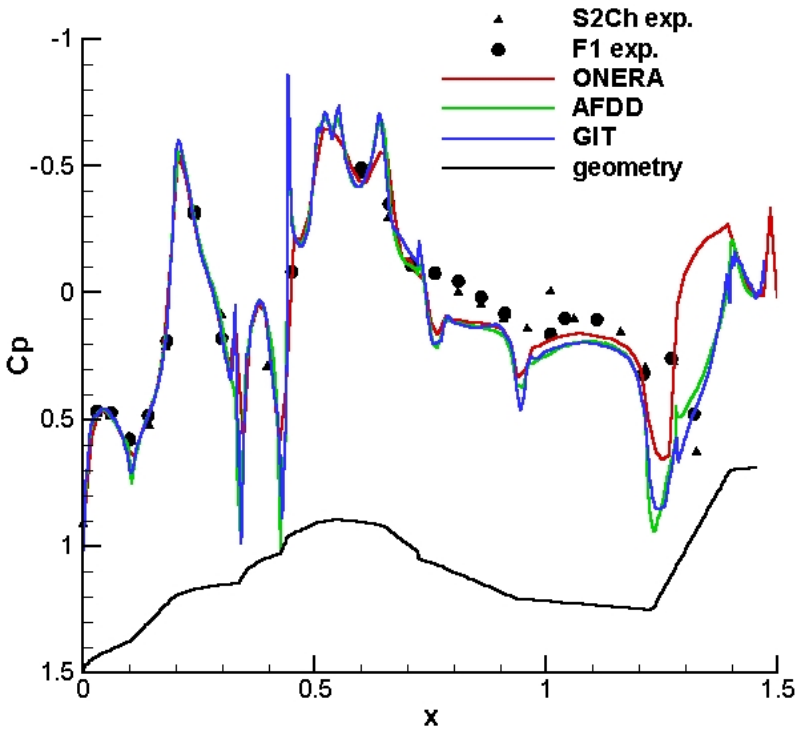

(a) Upper Centerline

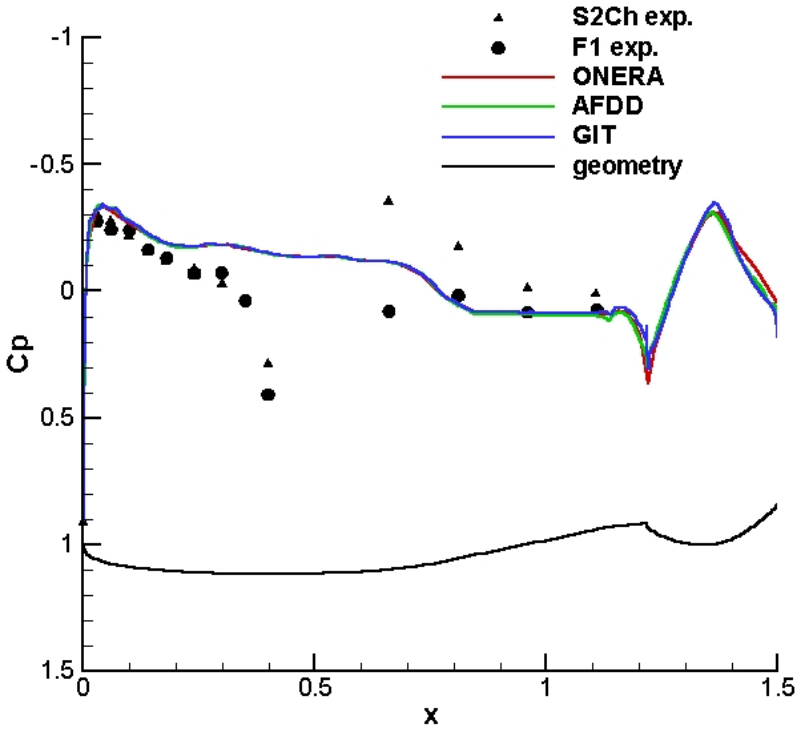

(b) Lower Centerline

Figure 63: Dauphin rotor off centerline C_p distribution. From Reference [111].

fuselage strut was added to the CFD model. Figure 64 shows the lower centerline pressure coefficient with and without the strut. Similar to the GIT and ROBIN configurations, the Dauphin shows a dramatically improved correlation with experiment when the strut is included. The Dauphin strut is a symmetric airfoil shape, so the downstream influence is not large. However, the stagnation point on the leading edge of the strut decelerates the flow, causing the pressure to increase as the flow approaches the strut.

The next phase of the study was to examine the influence of actuator disk rotor models on the configuration. Uniform and nonuniform disk loadings were applied to the Dauphin CFD model. The nonuniform loading was generated in a decoupled manner with the rotorcraft comprehensive code, HOST [118]. Figure 65 shows the upper centerline surface pressures computed with the uniform and nonuniform actuator disk. Both actuator disk models predict similar pressures over the forward portion of the fuselage, indicating a strong freestream influence. The uniform actuator disk is found to over predict the download along the tail boom, while the nonuniform actuator disk shows a good correlation with experiment over most of the centerline. Results in the region immediately downstream of the engines ($X > 0.7$) still indicate a difference with experimental, but the nonuniform results correlate better with the experiment in that region than the rotor-off or uniform rotor results. As indicated previously, an investigation into the model geometry in this region is underway.

Figure 66 shows the X component of vorticity resulting from the uniform actuator disk, nonuniform actuator disk, and experiment. As expected, the uniform actuator disk results in a symmetric distribution of vorticity about the centerline. Agreement between the uniform disk loading and the experiment is generally observed in the prediction of the tip vortex roll-up, but the asymmetry of the advancing and retreating sides is missed. The vorticity computed with a nonuniform disk loading is clearly asymmetrical, reflecting the nonuniform load distribution on the rotor. The nonuniform computation is more consistent with the experiment, showing many of the same features in the experimentally measured range.

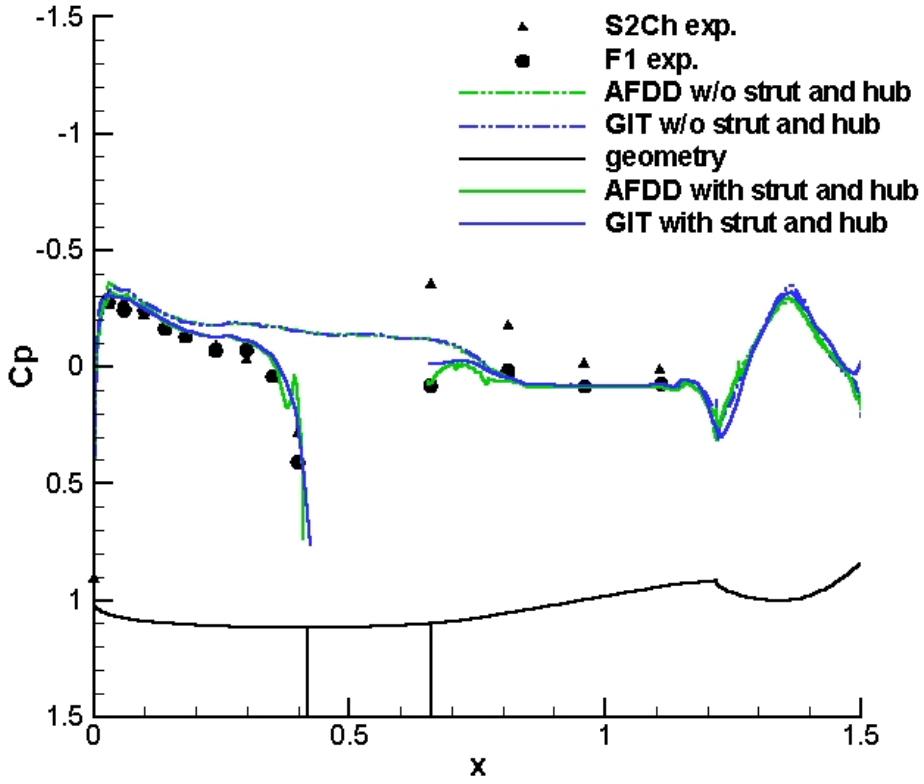

Figure 64: Dauphin rotor off lower centerline C_p distribution with strut. From Reference [111].

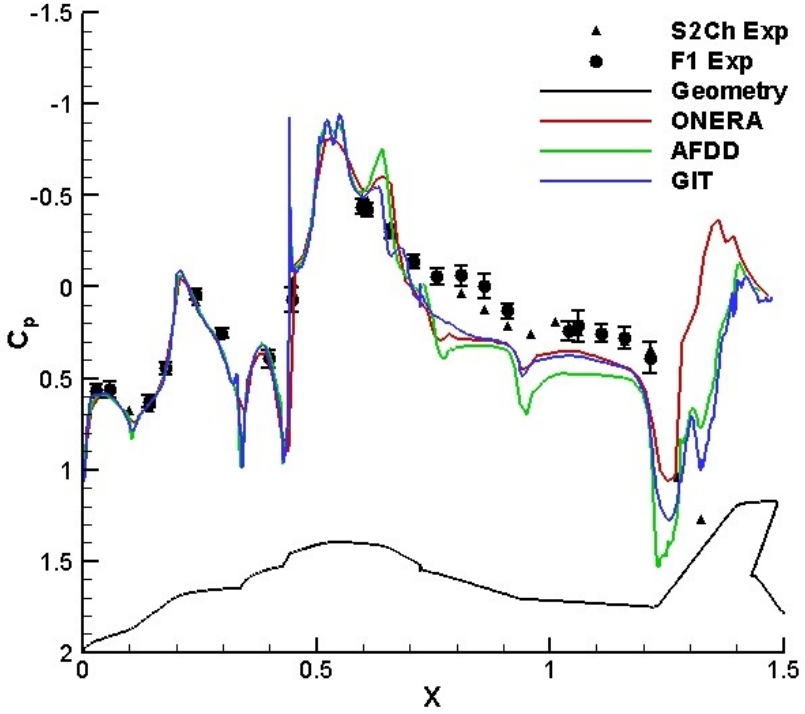

(a) Uniform Disk Loading

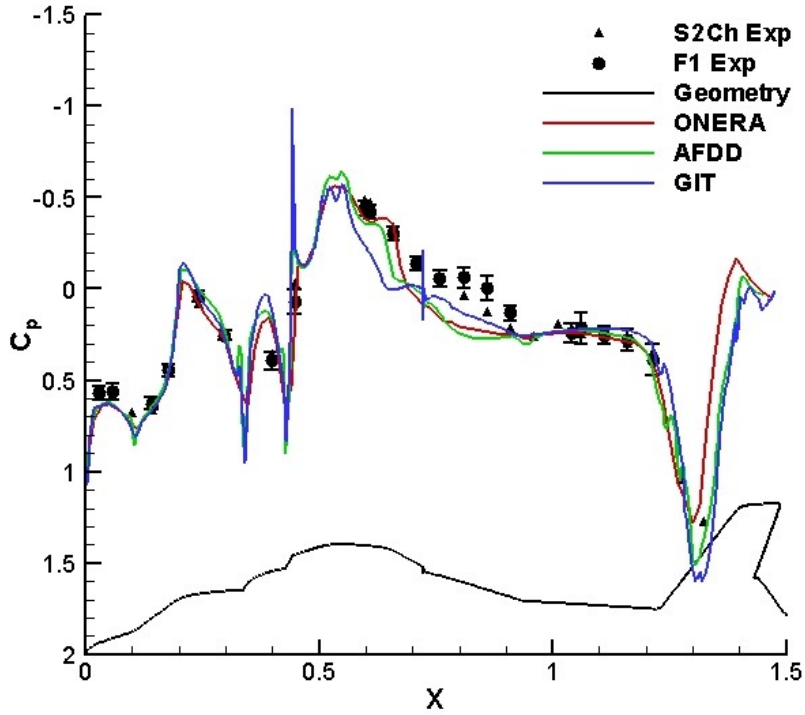

(b) Nonuniform Disk Loading

Figure 65: Dauphin upper centerline C_p distribution with an actuator disk. From Reference [111].

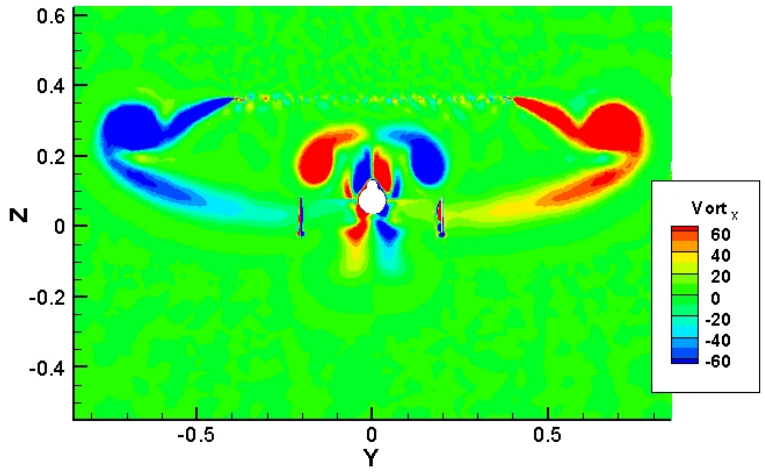

(a) Uniform Disk Loading

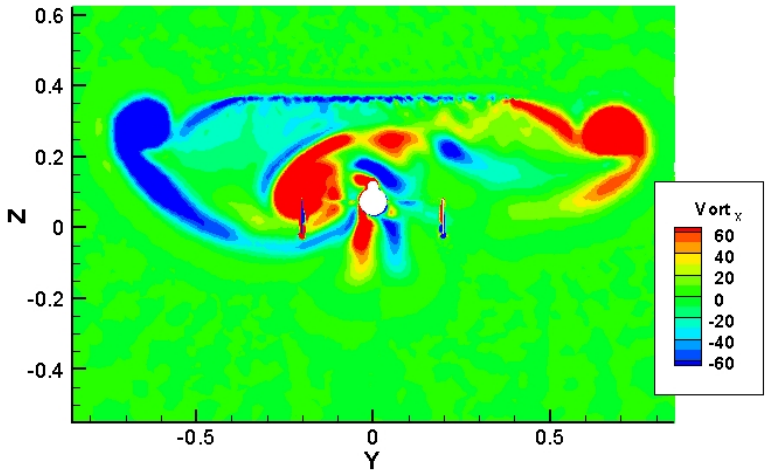

(b) Nonuniform Disk Loading

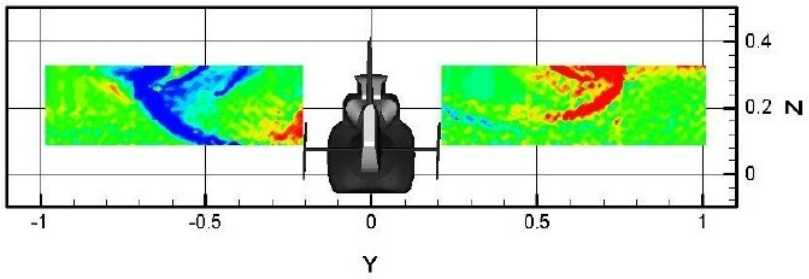

(c) Experimental PIV Measurement

Figure 66: Dauphin ω_x contours at $X = 1.1375m$. From Reference [111].

6.2 ROBIN Investigation

The ROBIN configuration was investigated in more detail to compare the capabilities of the various rotor models. The $\mu = 0.151$ and $C_T = 0.0064$ case from the Mineck and Althoff-Gorton experiment [31] was selected for this comparison. Each simulation in this section was run on the same fuselage grid to remove any bias due to differences in the computational mesh. The fuselage grid spacing was based on previous experience and the rotor wake spacing utilized the precise refinement strategy previously discussed. The details of the test geometry are presented in Chapter IV. In this section references to nondimensional fuselage stations X/L, Y/L, and Z/L will be written as X, Y, and Z respectively

The ROBIN fuselage grid consists of 1,671,270 nodes and 9,765,903 tetrahedral elements. The boundary layer mesh is approximately 11 layers thick and contains 493,521 nodes (approximately 30% of the mesh). The viscous spacing ensured that $y^+ < 1$ over the fuselage for this flow condition. The ROBIN fuselage has 34,724 surface nodes that connect to form 69,270 surface triangles. The rotor shaft and fuselage strut include 3,590 and 2,125 surface nodes, respectively. The fuselage is clearly the region of interest and therefore the majority of the grid points are concentrated there. The overset computation also uses four rotor blade grids, where a single blade grid consists of 266,886 nodes and 1,511,326 tetrahedra. The blade grid also has approximately 11 layers in the boundary layer mesh, for a total of 121,235 nodes in this region. Each rotor blade has 9,695 surface nodes and 19,386 surface triangles. Therefore, the overset grid has a total of 2,738,814 nodes, due to the addition of four blade grids to the fuselage grid.

All of the cases in this section were computed using the fully turbulent RANS equations loosely coupled with the Spalart-Allmaras turbulence model. The viscous spacing was specified in such a way that $y^+ < 1$ over the entire fuselage. The rotor-off and actuator disk computations utilized the incompressible flow option and the overset computation was run with compressible flow. An additional blade element actuator disk computation was performed with the compressible flow option for comparison. The source density for the

actuator disk computations was 200 radial by 720 azimuthal. This distribution was found to be sufficient to obtain source independence on this grid.

Since the blade element disk loading is theoretically the most accurate steady-state rotor model used in this evaluation, the blade element loading was evaluated on an initial grid to obtain the streamlines for the precise rotor wake refinement. However, it was discovered that the resulting disk loading exceeded the measured rotor thrust when the experimental pitch settings were utilized. The initial blade element computation resulted in a thrust coefficient of $C_T = 0.0102$, which is 60% larger than the experimental value. This implied that an important aspect of the experimental geometry is not being adequately modeled in the computational technique or that there is error in the experimental value.

Table 10 shows a comparison of the pitch controls obtained by other researchers for the same condition. (Note: The collective values are given at the zero blade station in this table, but are typically given in the references at the 75% station. This results in a 6° increase in collective.) The computational techniques consistently predict a lower collective pitch angle to achieve the same thrust, which indicates that better modeling could be achieved. However, the other experimental values are also lower, indicating that error in the experimental collective setting may also be to blame. Since a trim routine has not been implemented in the current study, the pitch settings from the unstrucutred method of Park et al. [76] were utilized. The actuator disk pitch setting at any radial station is given by the following equation:

$$\theta = 12.5 - 8\frac{r}{R} + 2.2\cos\psi - 2.0\sin\psi \tag{65}$$

The overset computations typically predict a lower thrust than the actuator disk, so the collective pitch was increased to 12.8° for the overset case. The blade element model was based on the following equations for the lift and drag coefficients.

$$\begin{aligned} C_\ell &= 6.0\alpha \\ C_d &= -0.02 + 2.0\alpha^2 \end{aligned} \tag{66}$$

The maximum and minimum lift values were set to 1.5 and -1.5, respectively. The drag was limited to a minimum value of 0.009 and capped at 1.5. With these limits, the lift and

drag coefficients are fully determined for all angles of attack as described in Chapter III.

Table 10: ROBIN Control Angles

Source	Method	Collective $\theta_{0.75R}$	Lateral θ_{1C}	Longitudinal θ_{1S}
Mineck & Gorton [31]	Experiment	16.3	2.7	-2.4
Elliott, Althoff, & Sailey [19]	Experiment	15.37	1.11	-3.23
Ghee & Elliott [30]	Experiment	12.55	1.39	-1.99
Ghee & Elliott [30]	Free Wake	13.87	3.33	-0.75
Chaffin & Berry [50]	Navier-Stokes Actuator Disk	13.18	2.21	-2.43
Tadghighi [55]	Navier-Stokes Actuator Disk	12.75	1.94	-2.00
Tadghighi [55]	Navier-Stokes Unsteady Actuator Disk	12.68	1.80	-1.89
Park, Nam, & Kwon [76]	Euler Deforming + Sliding Mesh	12.5	2.2	-2.0

6.2.1 Steady-State Computations

A series of steady-state computations were performed to examine the actuator disk loading models. All of the loading models were run using the incompressible flow option. Incompressible flow was found to be a permissible with the actuator disk rotor model, since the actuator disk indirectly accounts for tip velocities. The first computation did not utilize an actuator disk and represents the flow effect due to the freestream alone. The actuator disk computations were performed with the uniform, linear, and blade element loading models. An additional computation was also performed using the blade element loading and the compressible flow option for comparison.

Pressure coefficient contours in the $Y = 0$ plane are shown for all five cases in Figure 67. The stagnation region over the lower portion of the rotor shaft is not visible in this slice because the rotor shaft is offset to the right of the model centerline. The rotor-off solution in (a) is clearly different from the actuator disk computations and does not show the high pressure region under the rotor. However, the rotor-off computation does show a

clear influence of the rotor shaft and fuselage strut on the model surface pressure, which is reflected in the surface pressure distributions. In the vicinity of the fuselage upper extrusion ($0.5 < X < 1$), the flow accelerates and the pressure contour lines do not show the smooth transition over the extrusion that would be expected if the shaft was not modeled. A stagnation region is also generated under the fuselage due to the presence of the fuselage strut. The influence of the tunnel mounting has a clear influence on the fuselage surface pressures, which is particularly important when trying to correlate model forces with a full-scale geometry.

The rotor models in (b) - (e) all show the typical high pressure region under the rotor disk. The linear, (c), and compressible blade element, (e), results show a high degree of similarity in their contour levels over the forward portion of the geometry. Similarity also exists between the uniform, (b), and incompressible blade element (d) results over the nose region of the model. All of the models result in slightly features over the aft portion of the model. The uniform and both blade element models appear to show similar contours in the 0.2 to 0.3 level range, but the linear model shows the higher pressure region at the rear blade tip seen with the more-accurate blade element models. Compressibility seems to predominantly affect the smoothness of the contours, but overall the two blade element cases behave similarly.

Comparing the pressure coefficient contours in the fuselage symmetry plane shows many similar features, but the similarities are not as prevalent when comparing the models at a fuselage cross-section. Figure 68 shows the contours of the X component of vorticity at $X = 1.35$. The influence of the rotor shaft is seen above the fuselage by pairs of positive and negative vorticity that appear at $Z = 0.3$ and $Z = 0.75$ in Figure 68(a). These vortex pairs from the shaft are also present in the actuator disk simulations, but the higher pair is pulled downward toward the fuselage as a result of the rotor induced downwash. The fuselage strut is also observed to generate a pair of vortices beneath the fuselage, which are elongated downward when a rotor model is present. All of the rotor models show a strong tip vortex roll-up on the advancing ($Y > 0$) and retreating ($Y < 0$) sides of the fuselage, which is generated via the pseudo-lifting surface (pseudo-wing) effect of

the actuator disk. The blade element loading is very different from the simple loading models in that it has a high degree of asymmetry. The blade element prediction captures many of the similar characteristics of the nonuniform model simulation that was applied to the Dauphin configuration, but in the reverse sense, since the rotors rotate in opposite directions. When run with the compressible flow option turned on, the vorticity is found to diffuse quicker leading to reduced feature resolution. The increased diffusion effect can be primarily attributed to the disparity of the eigenvalues for low-Mach number compressible flows, as detailed by [95]. For low speed compressible flows the maximum eigenvalue tends toward the speed of sound and the minimum eigenvalue goes to zero. Since the stiffness of the system is proportional to the ratio of the eigenvalues, the stiffness tends toward infinity as the Mach number goes to zero and the solution scheme breaks down. Through the use of an artificial speed of sound, the incompressible formulation reduces the disparity of the eigenvalues and reduces the stiffness of the resulting system of equations.

Examining the rotor downwash provides further insight into the effects of each model. The w component of velocity at tail center plane ($Z = 0.04$) is shown in Figure 69 for the five steady-state cases. A small amount of asymmetry is present in the rotor-off case, since the model was yawed 1.2° with respect to the flow. The uniform loading creates a larger downwash near the centerline ($Y = 0$) of the fuselage than the linear model, since the uniform model has a larger disk loading over the center of the disk. The effect of the yawed flow is not as obvious when the rotor is on because the rotor induced velocity has a larger influence on the flow. The blade element model shows that neither of the simple models is doing a good job of modeling the downwash velocity away from the fuselage centerline. The blade element model shows a much larger downwash effect on the advancing blade side than the retreating blade side. An upwash is present for all of the models outside of the rotor wake as a result of the tip vortex roll-up. The two blade element models show noticeable differences in the downwash velocity due to the reduced diffusion of the wake vorticity observed when the incompressible flow option is on.

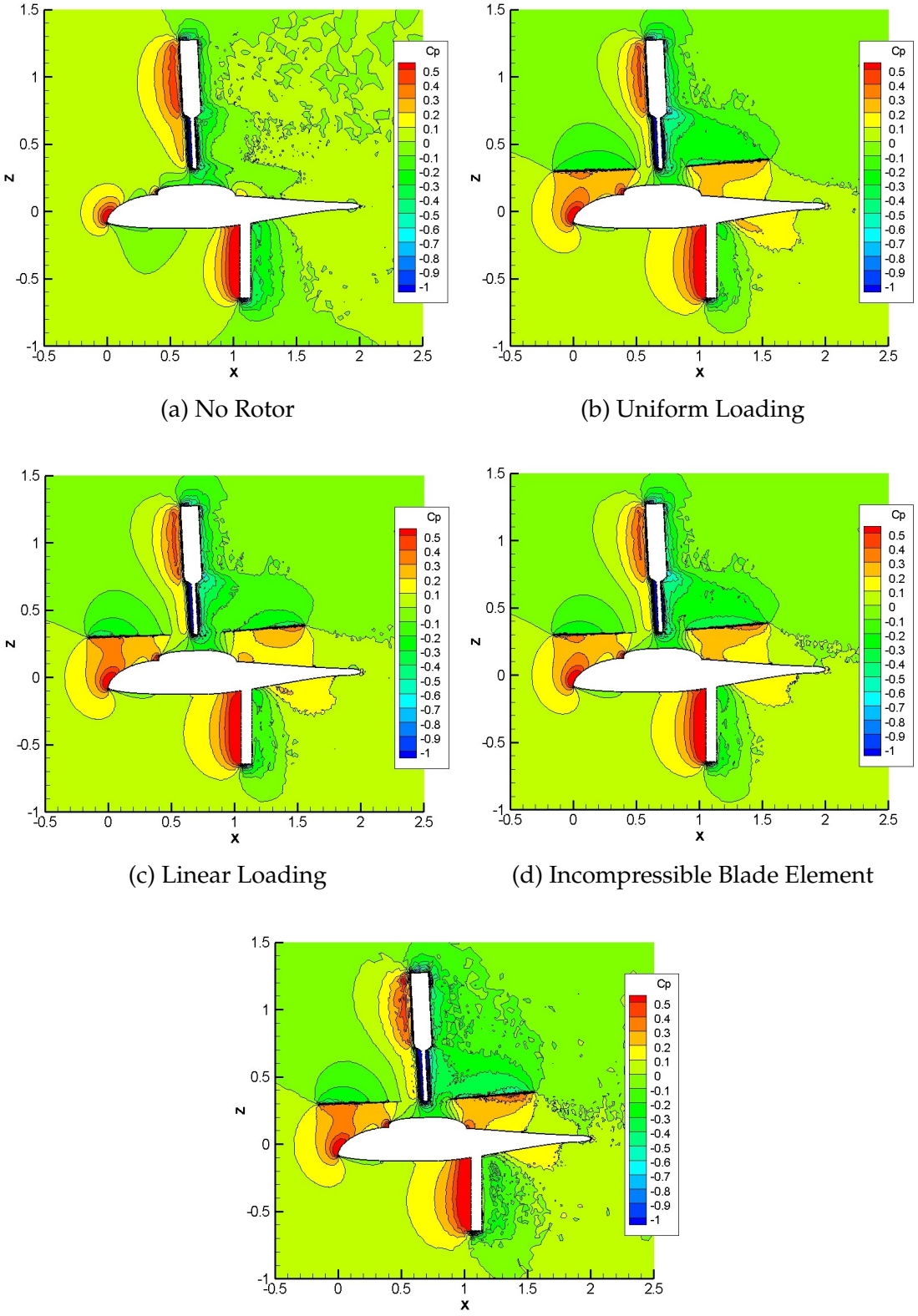

(a) No Rotor

(b) Uniform Loading

(c) Linear Loading

(d) Incompressible Blade Element

(e) Compressible Blade Element

Figure 67: ROBIN C_p contours at $Y = 0$ with various actuator disk loadings.

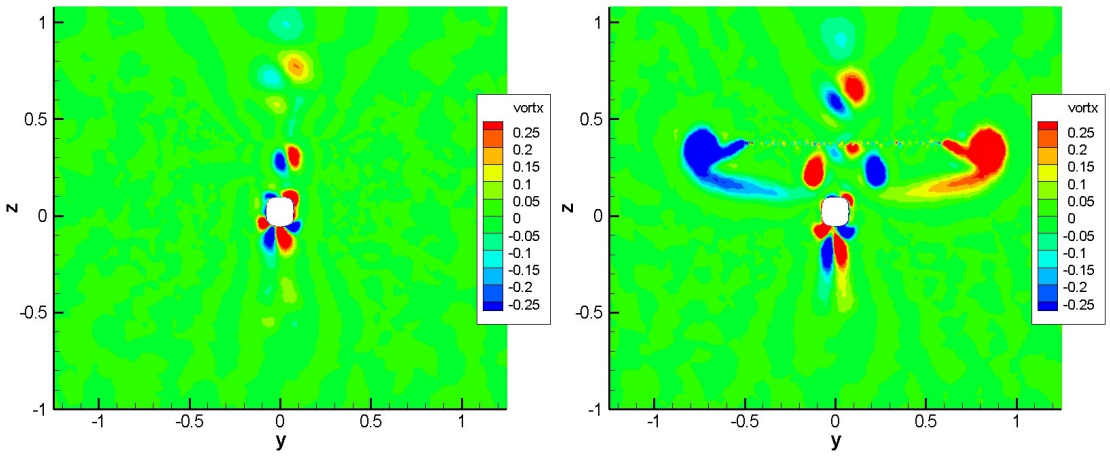

(a) No Rotor

(b) Uniform Loading

(c) Linear Loading

(d) Incompressible Blade Element

(e) Compressible Blade Element

Figure 68: ROBIN ω_x contours at $X = 1.35$ with various actuator disk loadings.

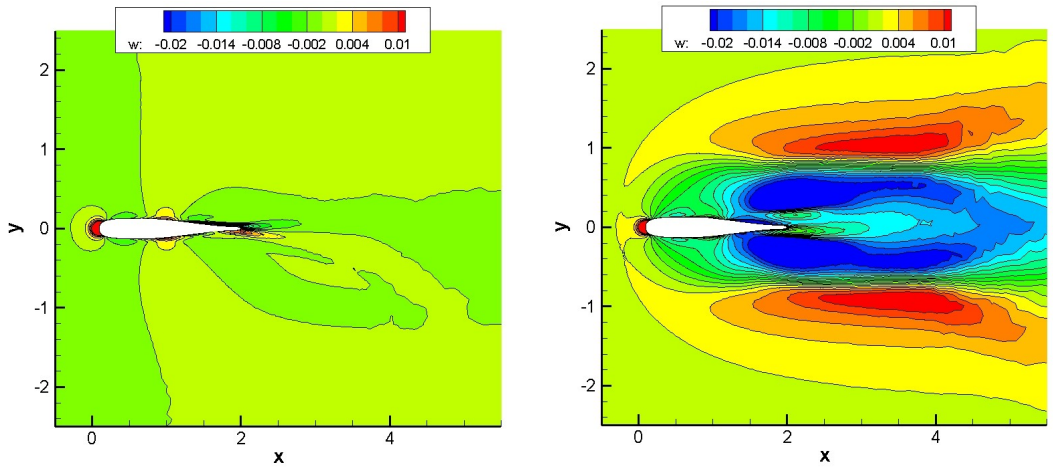

(a) No Rotor

(b) Uniform Loading

(c) Linear Loading

(d) Incompressible Blade Element

(e) Compressible Blade Element

Figure 69: ROBIN w velocity contours at the tail center plane ($Z = 0.04$) with various actuator disk loadings.

6.2.2 Unsteady Computations

Unsteady computations were computed for the ROBIN configuration using overset rotor blade grids. The actuator blade model was not utilized in this investigation, since it was observed to require larger computation times than the higher fidelity overset method [77]. The overset method was run with the compressible option of FUN3D, since the rotor tip velocity is directly modeled by this approach. The tip Mach number for the advancing blade was 0.6 in the ROBIN experiment, which is well into the compressible flow regime. The time step for this computation was equivalent to one degree of rotor revolution per iteration. During each time step 15 sub-iterations were performed to reduce the temporal error.

The most obvious advantage of an unsteady computation is that a realistic unsteady wake is obtained. Rotor wake visualizations are shown in Figure 70 and Figure 71 for the overset computation after four rotor revolutions. (Note: the rotor blades rotate counter-clockwise when viewed from above.) These figures are plotted using the Q criteria to remove the the influence of random vorticity associated with turbulent flow. A distinct tip vortex is observed trailing behind each of the rotor blades. The tip vortex trailing behind the blades at $\psi = 0°$ and $\psi = 90°$ rolls up into trailing vortices that propagate downstream from the advancing and retreating tips of the rotor disk. This tip vortex roll-up occurs in forward flight and is analogous to the tip vortices generated by fixed wing aircraft, since the rotor disk can be thought of as a circular wing, which generates trailing vortices at its tips. Three blade tip vortices are seen in the third quadrant ($\psi = 180°$ to $270°$) of Figure 71. The oldest of these is observed to interact with the root vortex of the blades at $\psi = 90°$ and $\psi = 180°$ to generate a root vortex roll-up on the right side of the fuselage. In Figure 70, the two older vortices in the third quadrant appear to have been split into two by the blade at $\psi = 270°$. Another root vortex can also be seen propagating over the tail of the configuration.

The unsteady nature of the rotor wake naturally leads to variations in the fuselage surface pressures. Surfaces pressures are shown on the advancing blade side of the fuselage

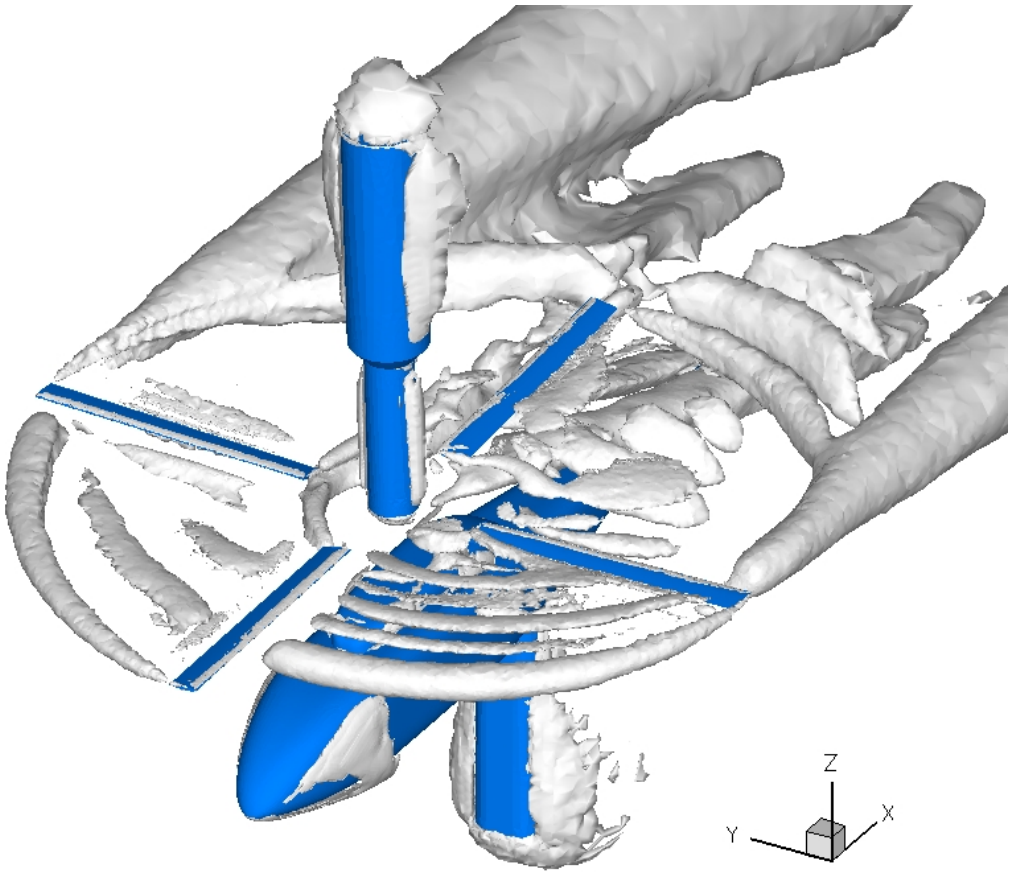

Figure 70: ROBIN rotor wake visualization with overset rotor blades ($Q = 0.001$).

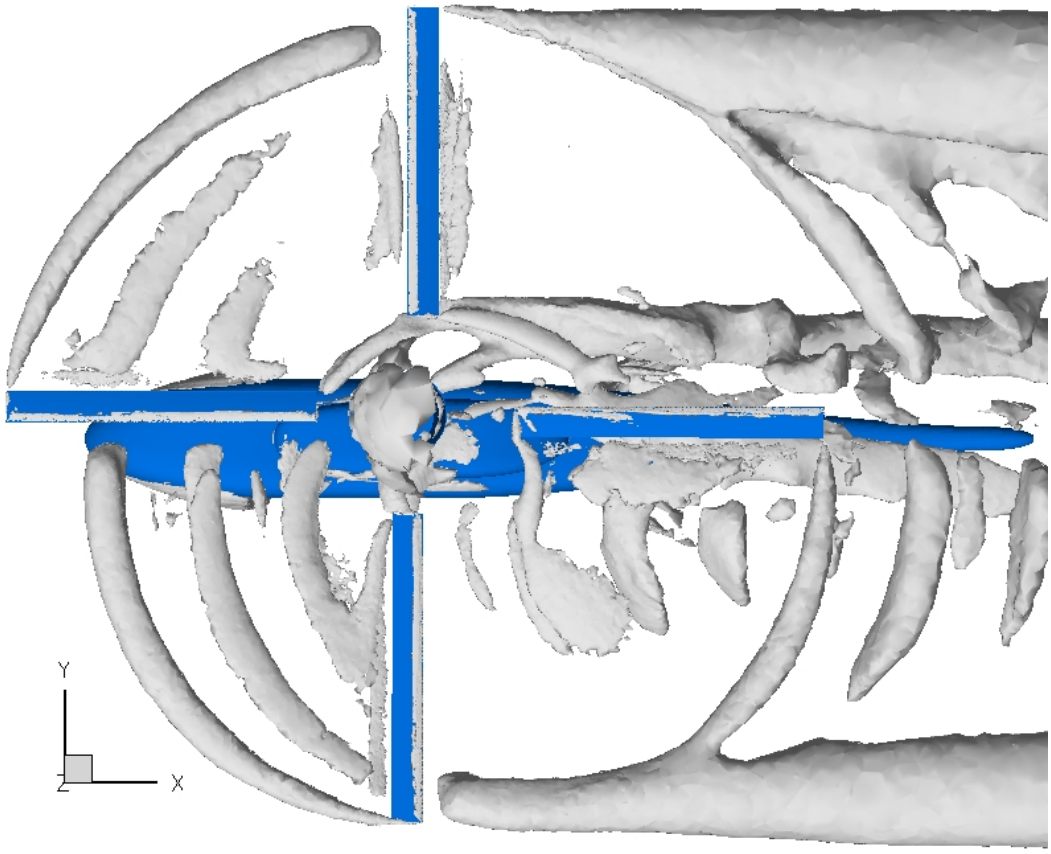

Figure 71: ROBIN rotor wake visualization with overset rotor blades, top view ($Q = 0.001$).

in 6° increments in Figures 72, 73, and 74. The blade passage effect is clearly demonstrated when the blade passes over the fuselage. As the blade moves away from the fuselage the high pressure regions on the top of the fuselage diminish. From $\psi = 30°$ to 54° the download on the fuselage is at its minimum, since the blades are not directly over the fuselage. At $\psi = 60°$ the blade root begins to pass over the fuselage causing the pressure over the nose and tail of the configuration to gradually increase until the maximum download at 90° is achieved.

The ROBIN configuration was instrumented with 11 pressure transducers to measure the unsteady static pressure along the upper centerline of the model. The time histories of the computed pressures at these 11 locations are shown in Figures 75 through 80. Conversations with Dr. Mineck (the first author of the test report) indicated that a 28 degree correction should be applied to the experimental data to account for a lag between the azimuthal measurement of the blade position and when the pressure was recorded. Application of this correction leads to an significantly improved correlation between the phase of the CFD computation and experimental data. Analytical theory also agrees with this correction; the pressure should be a maximum when the blade passes overhead, but the uncorrected experimental data indicates that the pressure is at a minimum at this point. Since the flow is periodic, a Fourier analysis of the unsteady pressures has also been performed.

The first two measurement locations, shown in Figure 75, were on the nose of the model at $X = 0.052$ and $X = 0.096$. The phase and amplitude of the computation and experiment are in good agreement, but the CFD overpredicts the steady component of the static pressure at both locations, indicating that the pitch of the blade at $\psi = 180°$ is too high. The probable cause of this overprediction is the uncertainty of the blade pitch setting described in the beginning of Section 6.2. The computation at $X = 0.201$ (Figure 76(a)) shows a similar behavior to the first two locations. At $X = 0.256$ (Figure 76(b)), the computation is in good agreement with the experiment in all aspects for the first peak, but the subsequent peaks have lower maximums, causing the computation to primarily over predict the 4/rev component in the Fourier analysis.

Computed surface pressures over the nacelle region are found to be in poor agreement with the experiment. The nacelle results are shown in Figure 77 for the region forward of the rotor hub and in Figure 78 for the region aft of the hub. The inability to model the experimental geometry between the blade root and the hub is the most likely reason for the disagreement in this region. The tail pressures show the best agreement between the computation and the experiment as seen in Figure 79 and Figure 80. The two stations closest to the blade tip, $X = 1.368$ and $X = 1.556$, show particularly good correlation. An interesting aspect of the CFD result is highlighted by the Fourier analysis; the computation has virtually no periodic content other than multiples of 4/rev. The multiples of 3/rev and 5/rev are typically associated with vibrations. The fact that the experiment has some of this additional content is an indication that the rigid body assumption has filtered out some of the physics of the system.

6.2.3 Model Comparison

The modified pressure coefficient is plotted along the upper centerline of the ROBIN in Figure 81. No steady pressure taps were available on the model centerline, so the steady experimental values immediately to the left and right of the centerline have been shown for comparison. There is not a large difference between the various rotor models, which is consistent with the C_p contours shown in Figure 67. All of the rotor cases predict an increase in pressure over the length of the fuselage when the rotor is present. There is generally good agreement between the the computations and the experiment, but the prediction at $X = 1.0$ is larger by approximately $\Delta C_p^* = 0.004$. This reenforces the earlier statement that better modeling is required in the rotor hub region. The overset computation predicts a lower pressure than the actuator disk models over the tail, which is in good agreement with the averaged experimental pressure measurements. Due to the small influence of the rotor at $\mu = 0.151$ on the fuselage side pressures, the pressure coefficients at the fuselage cross-sections have not been shown. The free stream effect is the dominant influence over the sides of the configuration and has already been shown to be well predicted by the CFD computations in Chapter V.

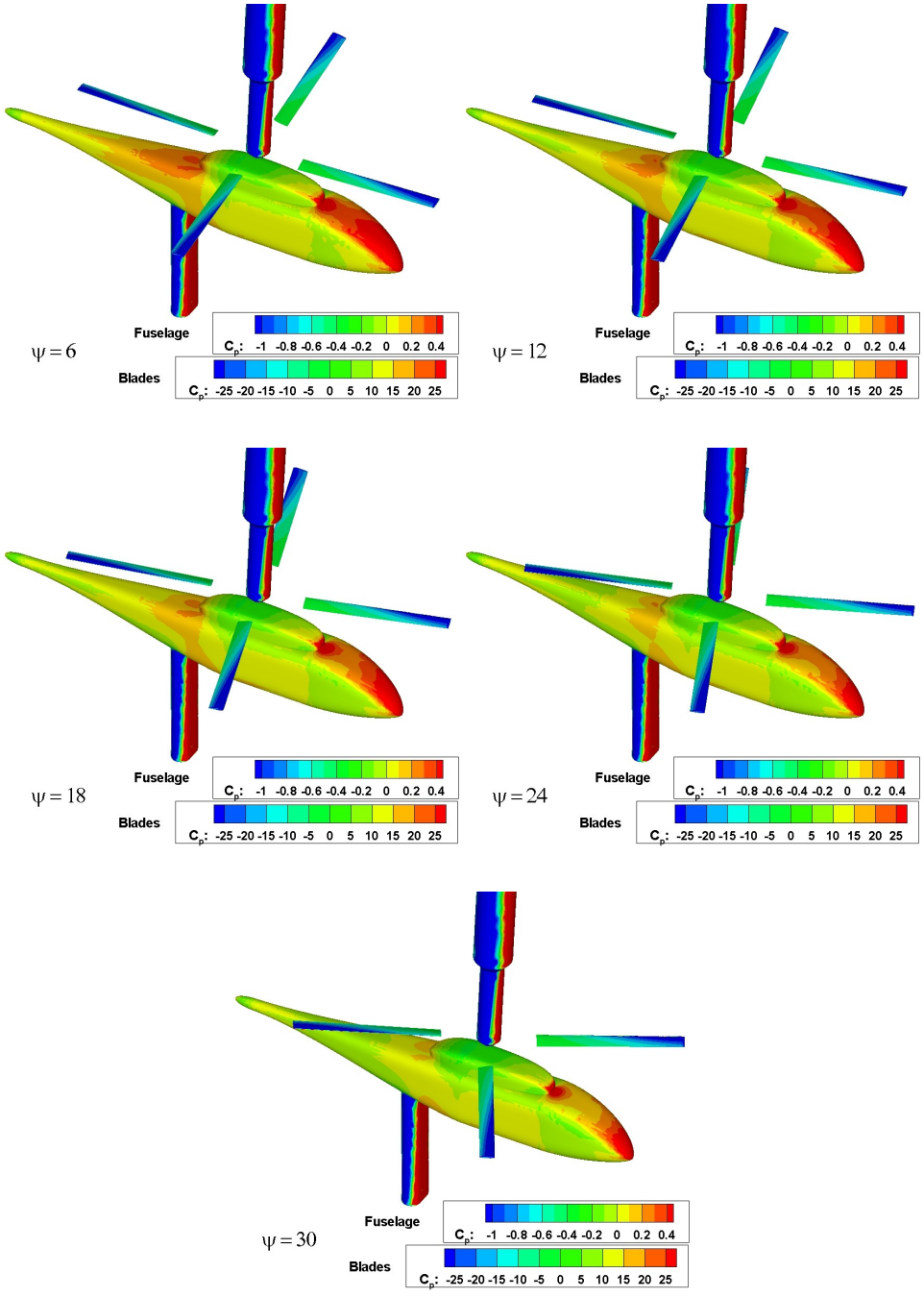

Figure 72: ROBIN unsteady surface C_p for $\psi = 6°$ to $30°$.

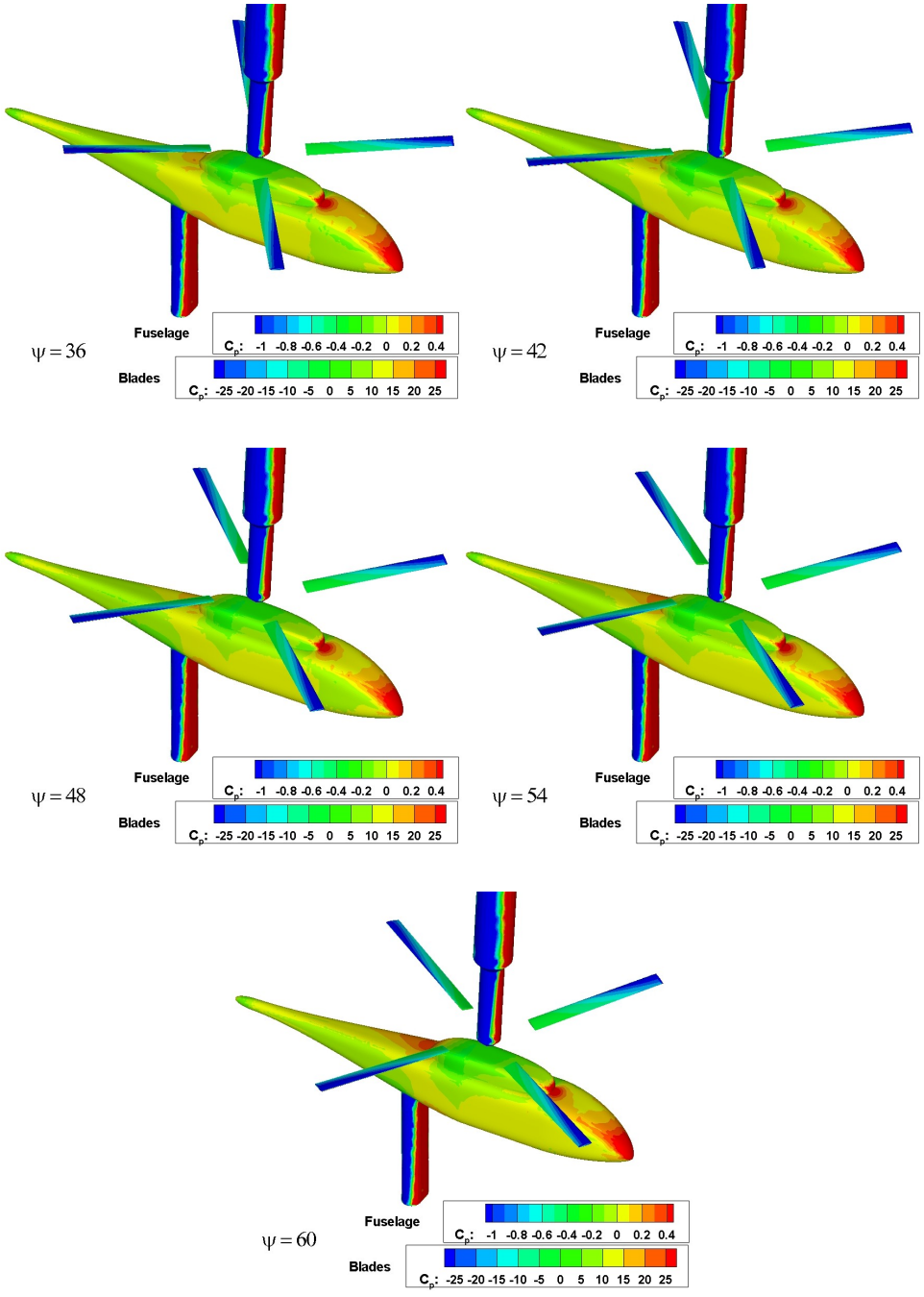

Figure 73: ROBIN unsteady surface C_p for $\psi = 36°$ to $60°$.

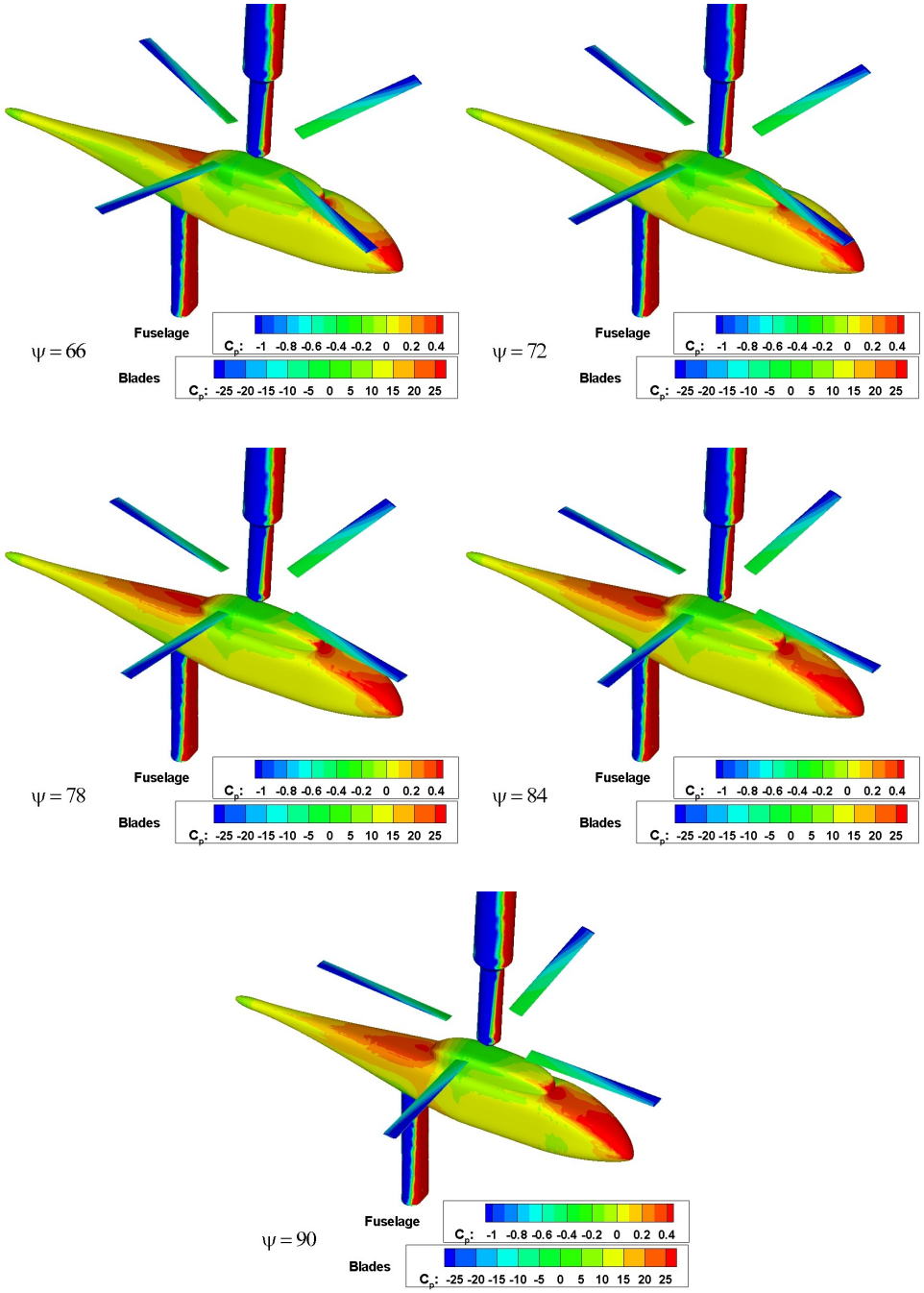

Figure 74: ROBIN unsteady surface C_p for $\psi = 66°$ to $90°$.

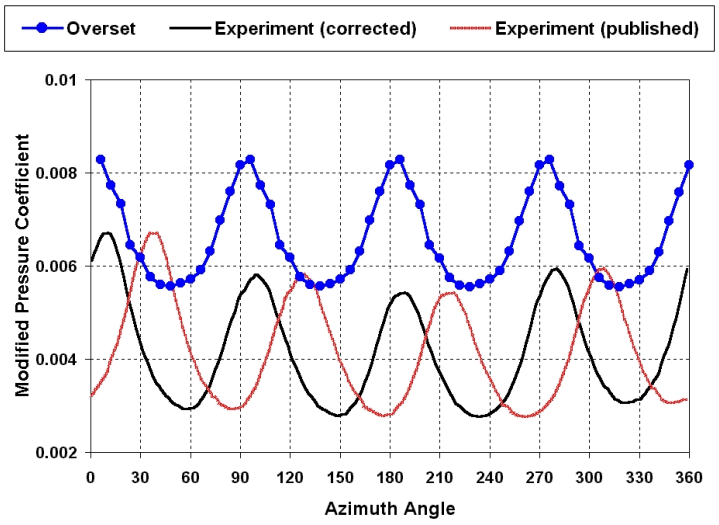

(a) $X = 0.052$

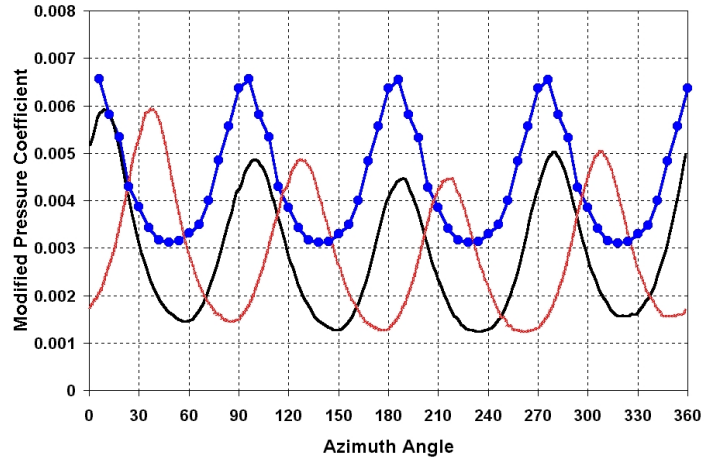

(b) $X = 0.096$

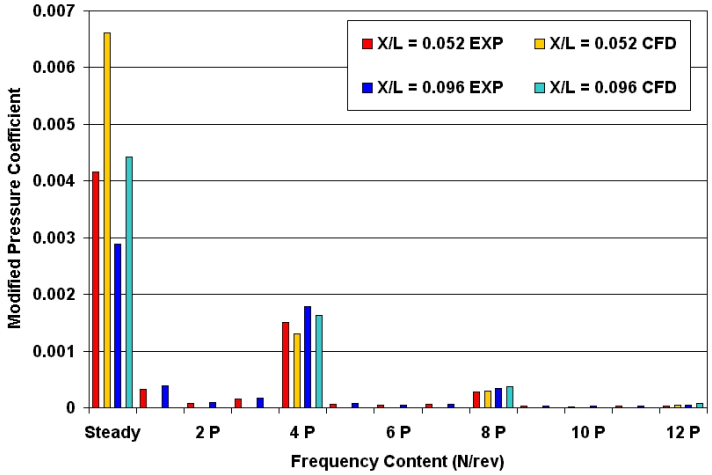

(c) Fourier Analysis

Figure 75: ROBIN unsteady surface C_p at $X = 0.052$ and $X = 0.096$.

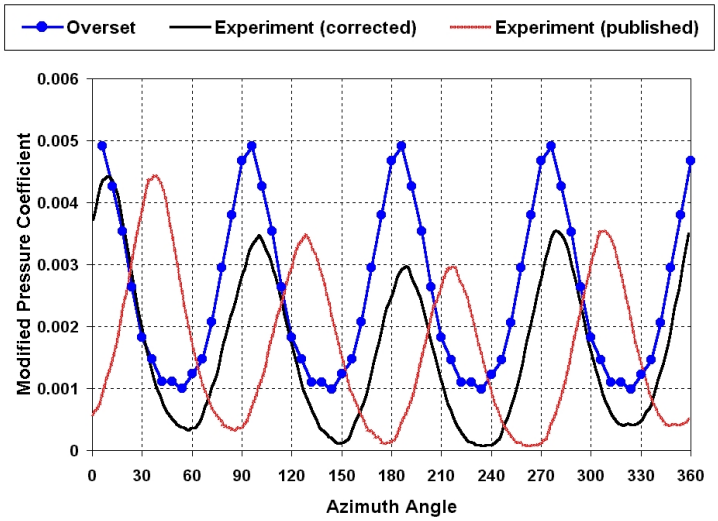

(a) $X = 0.201$

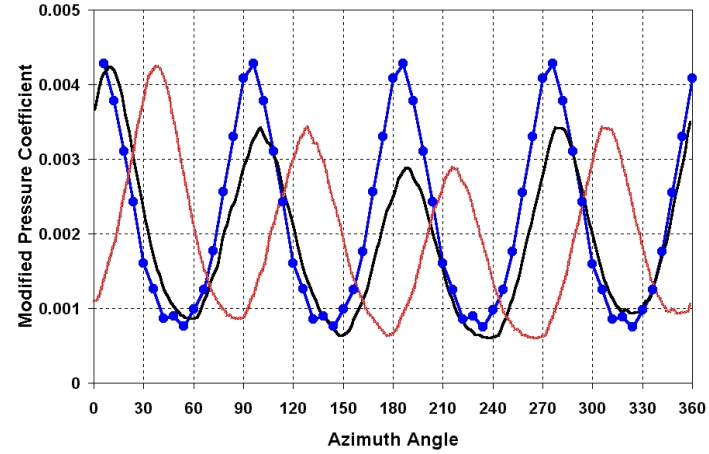

(b) $X = 0.256$

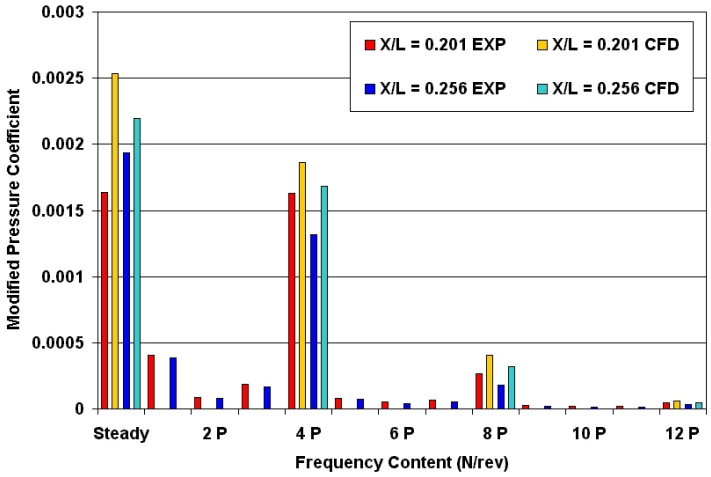

(c) Fourier Analysis

Figure 76: ROBIN unsteady surface C_p at $X = 0.201$ and $X = 0.256$.

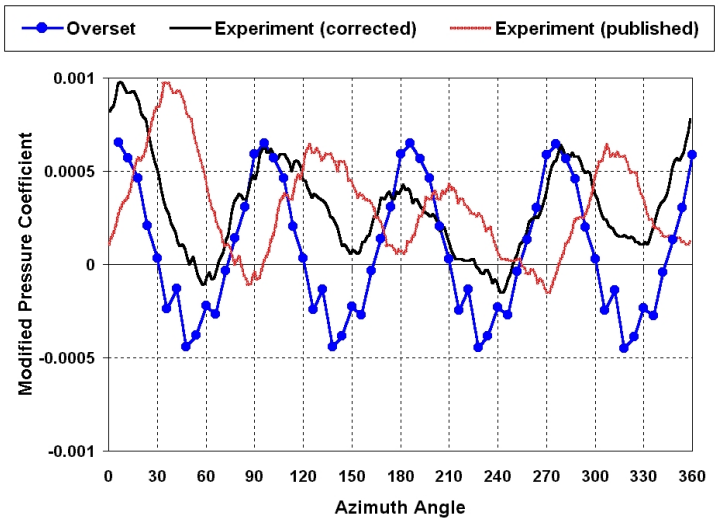

(a) $X = 0.467$

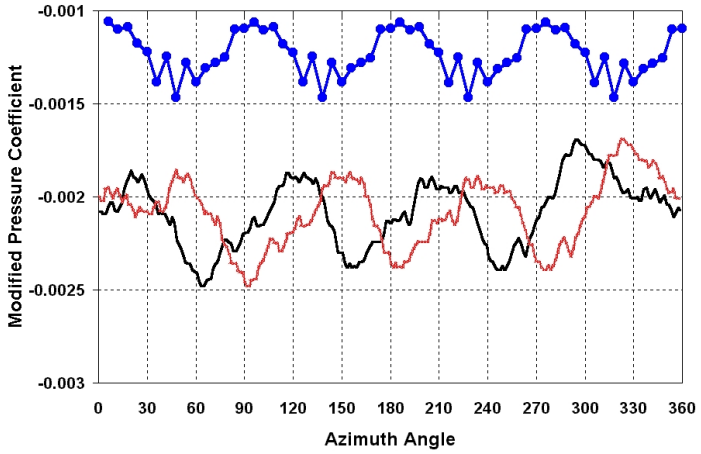

(b) $X = 0.600$

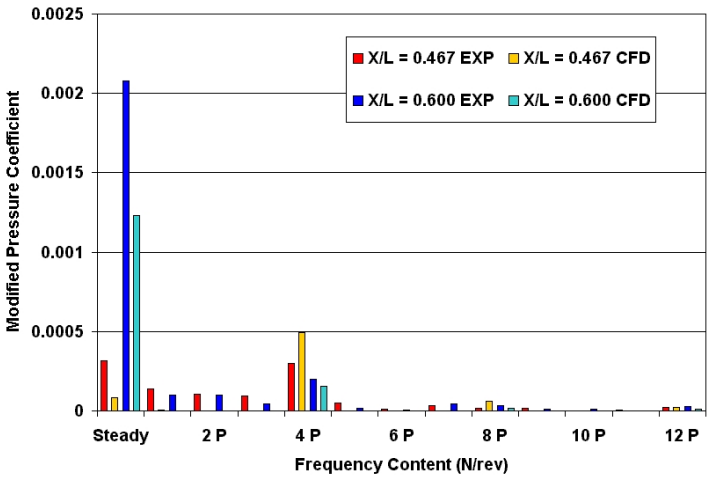

(c) Fourier Analysis

Figure 77: ROBIN unsteady surface C_p at $X = 0.467$ and $X = 0.600$.

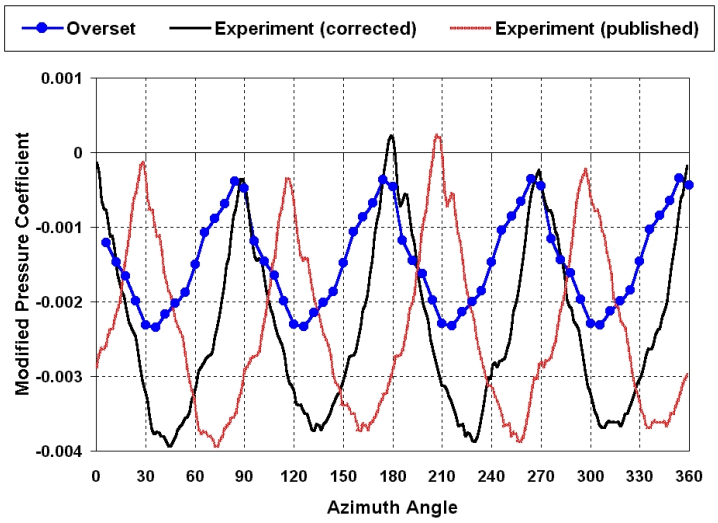

(a) $X = 0.896$

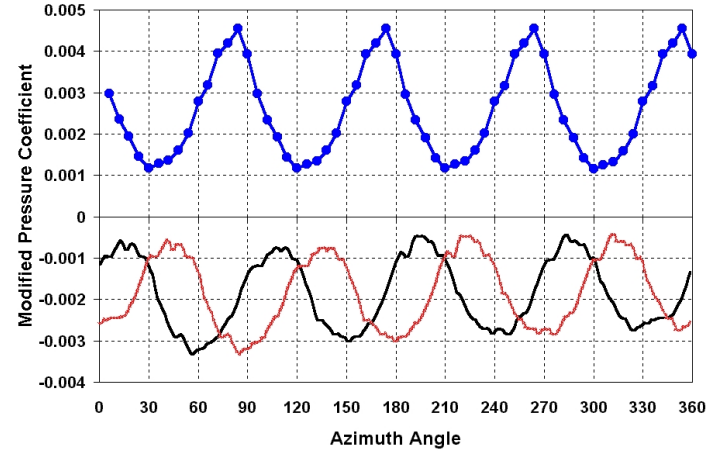

(b) $X = 1.001$

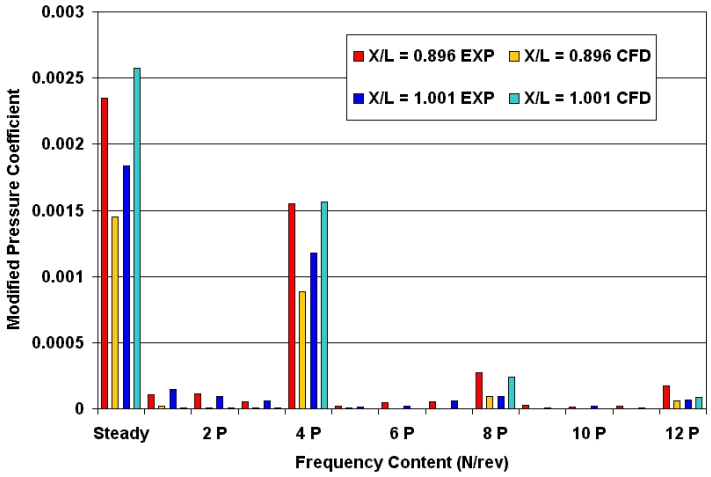

(c) Fourier Analysis

Figure 78: ROBIN unsteady surface C_p at $X = 0.896$ and $X = 1.001$.

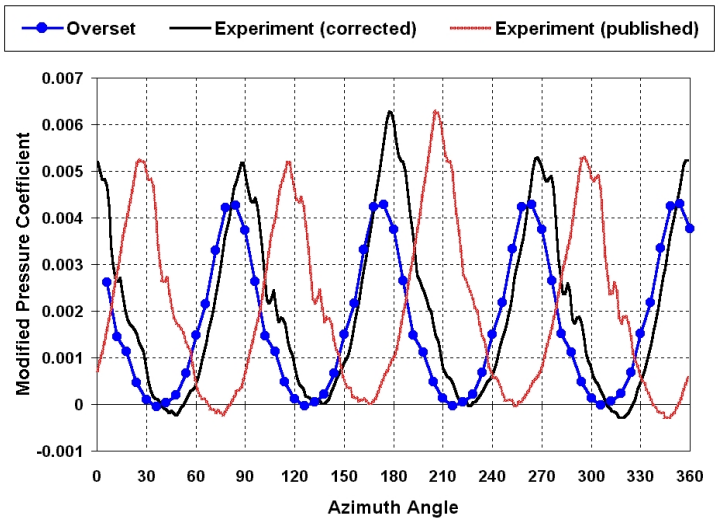

(a) $X = 1.180$

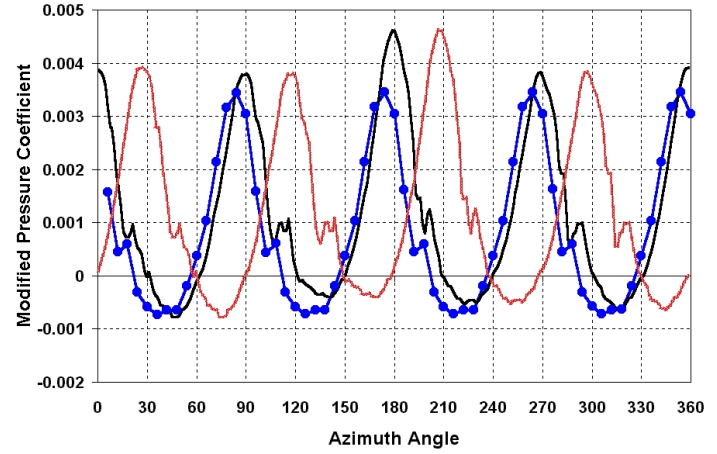

(b) $X = 1.368$

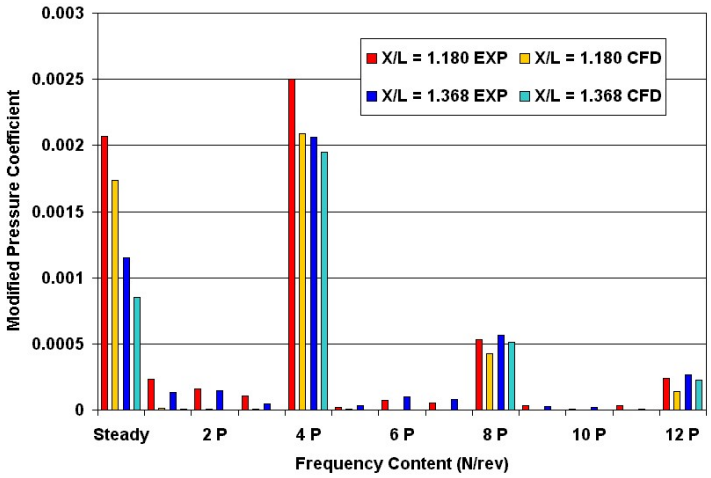

(c) Fourier Analysis

Figure 79: ROBIN unsteady surface C_p at $X = 1.180$ and $X = 1.368$.

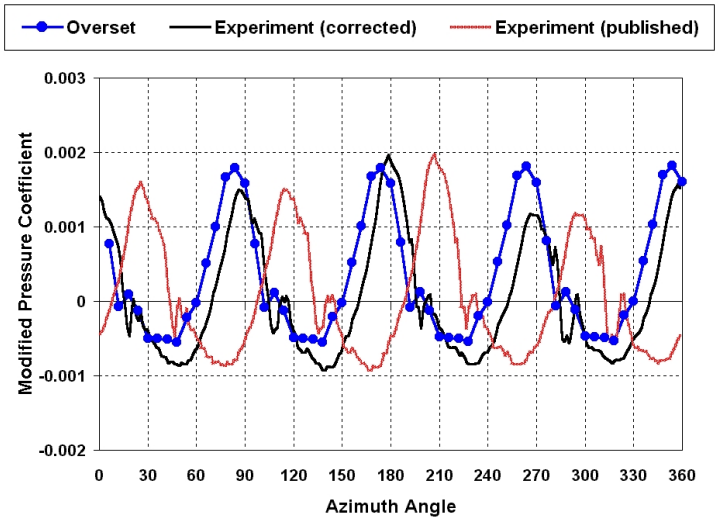

(a) $X = 1.556$

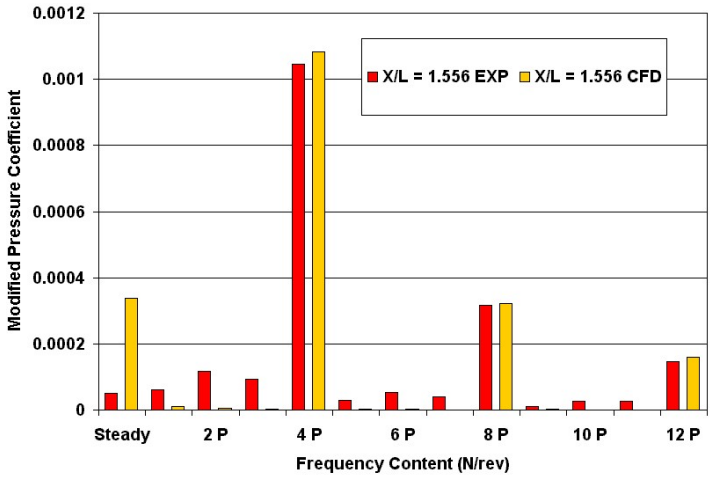

(b) Fourier Analysis

Figure 80: ROBIN unsteady surface C_p at $X = 1.556$.

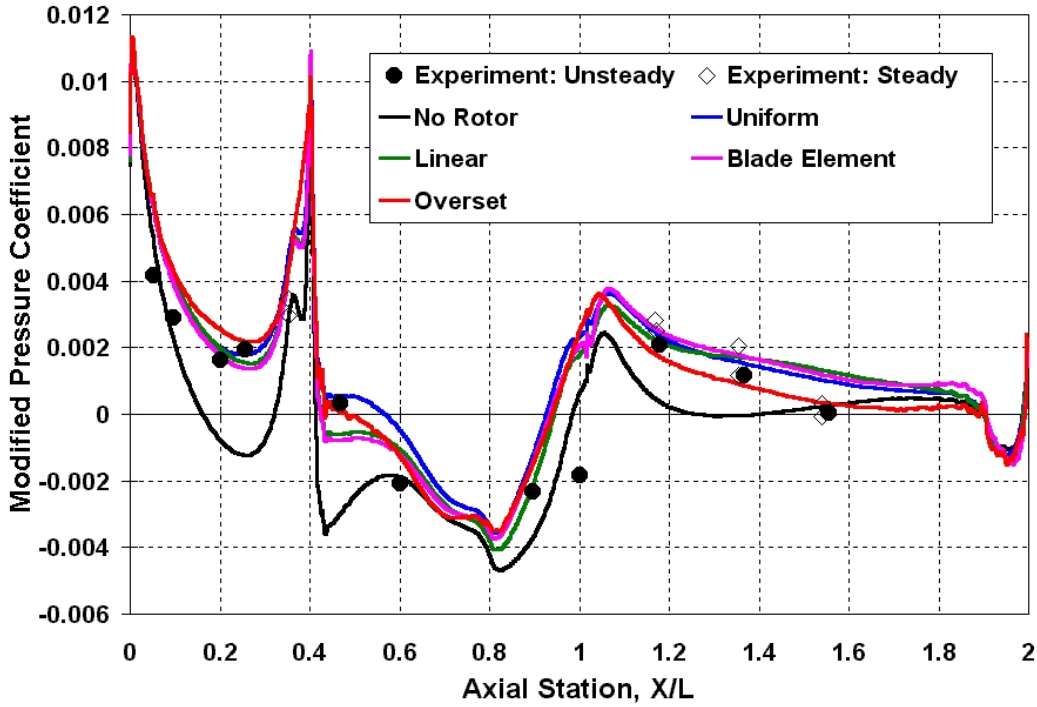

Figure 81: ROBIN centerline C_p comparison with various rotor models.

Comparisons of the rotor wake are shown using vorticity iso-surfaces for all of the cases in Figure 82 and the corresponding top views are shown in Figure 83. The Q criteria did not represent the vortex sheet of the actuator disk models satisfactorily, so the traditional vorticity-based visualization was utilized. The incompressible vorticity has been normalized by the speed of sound to plot all of the models on the same scale. The figures look very similar with the exception of the rotor-off case. The actuator disk based approaches all show a ring at the tip of the disk. If a smaller contour level had been utilized more of the vortex sheet structure would be visible. The uniform model has a strong root vortex that forms at the cutout, but this feature tends to be significantly weaker for the other models. Vorticity in the plane of the actuator disk is visible for the blade element models as a result of the nonuniform disk loading. As previously mentioned, the overset method differs in that an unsteady wake is formed rather than a steady-state one.

A comparison of the fuselage forces for each of the models is shown in Table 11. The rotor thrust is accurate to the first significant digit, but is found to be under predicted for the incompressible blade element and overset rotor models. The normal force (F_z) decreases as

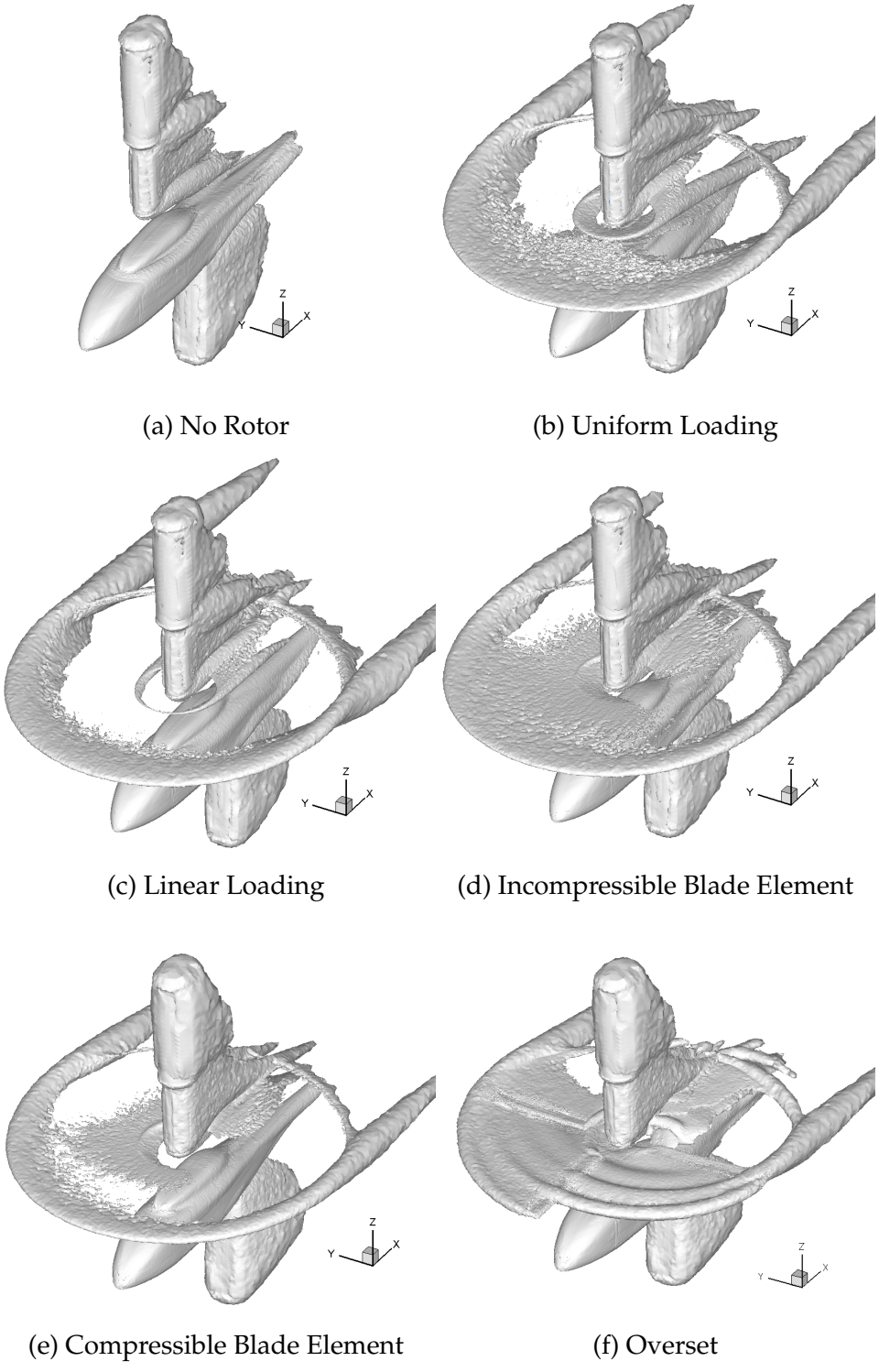

(a) No Rotor

(b) Uniform Loading

(c) Linear Loading

(d) Incompressible Blade Element

(e) Compressible Blade Element

(f) Overset

Figure 82: ROBIN rotor wake visualization with various rotor models ($|\omega| = 0.50$).

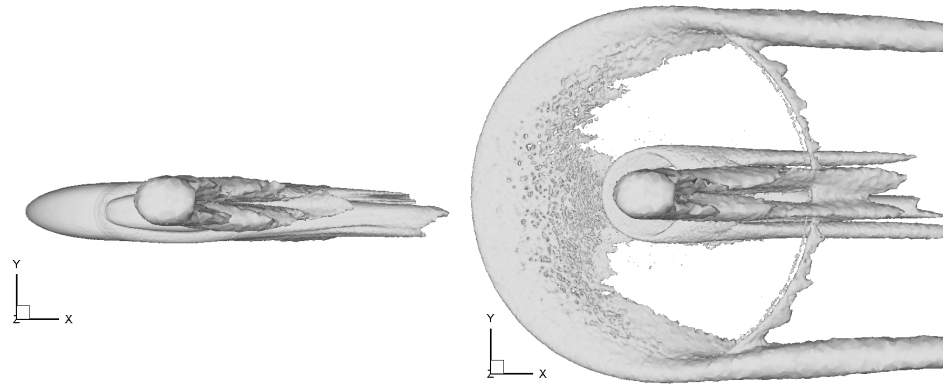

(a) No Rotor

(b) Uniform Loading

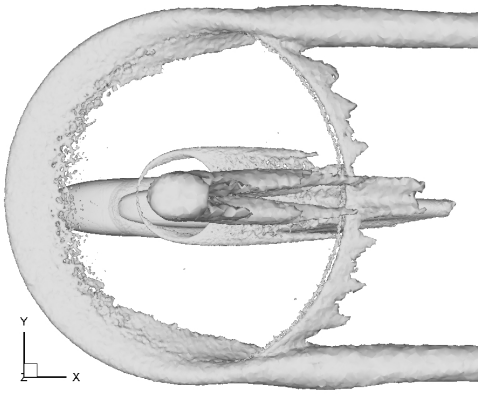

(c) Linear Loading

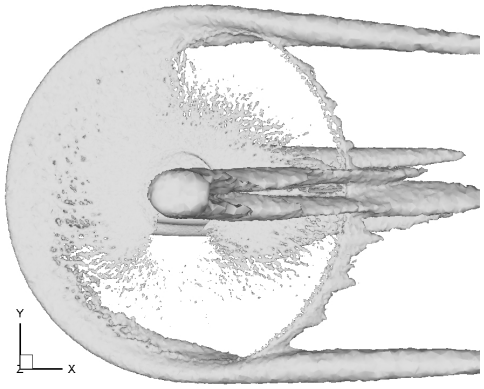

(d) Incompressible Blade Element

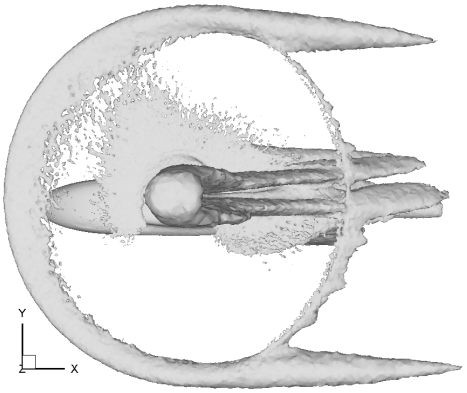

(e) Compressible Blade Element

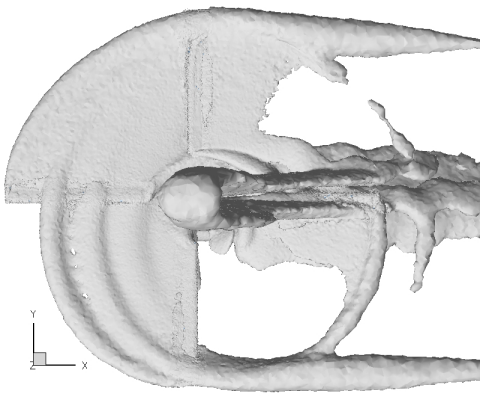

(f) Overset

Figure 83: ROBIN rotor wake visualization with various rotor models, top view ($|\omega| = 0.50$).

expected when the rotor is present. Due to the increased loading over the central region of the disk, the uniform actuator disk model predicts the largest down force on the fuselage. The drag numbers (F_x) are in good agreement for all of the models, which indicates that much of the drag is due the freestream flow. The force history was only recorded for the rotor blades during the overset computation, so the viscous fuselage forces are unknown. To compare with the other computations the fuselage surface pressures were integrated from the animation files for the overset case, but as a result the drag is significantly under predicted. A nose down pitching moment (M_y) is predicted for each of the cases. The presence of the rotor consistently increases the nose down moment. The two simple models appear to overpredict the nose down moment when compared to the other models, indicating that the fore and aft symmetry of the blade loads is a poor representation. The blade element models indicate that the nose left yawing moment (M_z) increases as a result of the rotor. However, the blade element method predicts that the nose left yawing moment decreases by roughly 50%.

A summary of the computational runtime for all of the cases is shown in Table 12. The scaled time provides a good indicator of the required work for each computation.

$$t_{scaled} = \frac{t_{run} N_{processors}}{N_{iterations} N_{nodes}} \tag{67}$$

The uniform and linear blade element actuator disk models were run with an executable that was compiled with some additional optimizations, so they required the shortest scaled time. If run with the same executable as the other cases, these two models would be expected to require a slightly increased cost over the rotor off case. The incompressible blade element method incurs a 7.6% increase in cost over the rotor-off baseline. The compressible blade element model requires roughly 46% more time than the incompressible version, but this increase in cost is primarily attributed to the additional cost of solving the energy equation. The overset case is obviously the most costly of the models, since higher fidelity simulations require greater costs. The scaled time for the overset case was found to be 25 times more than the scaled time for the compressible blade element. This cost is due to a combination of the overset interpolations and the time-accurate algorithm. It should be

noted that the DCI files were precomputed for this case, since prescribed motions were being utilized. If the DCI file was dynamically recomputed after each iteration, the cost of the overset computation would have been even higher, since the flow solver would pause after each iteration to wait for a new DCI file to be generated. SUGGAR required approximately three minutes to compute a DCI file and can only be run on a single processor (i.e. the code is not parallelized). Therefore, if the DCI files had not been precomputed, the overset computation would have taken approximately 72 hours longer (3 minutes x 1440 iterations). The importance of parallel computing is also observed for these cases. The overset computation required 155.7 hours on 72 processors, but would have required approximately 467 days if run on a single CPU.

Table 11: ROBIN Force & Moment Comparison

Computational Technique	**Rotor**	**Fuselage**			
	C_Tx100	C_{Fz}x100	C_{Fx}x100	C_{My}x100	C_{Mz}x100
No Rotor	N/A	1.219	1.028	-0.375	0.521
Uniform Actuator Disk	0.643	-0.164	1.083	-0.780	0.405
Linear Actuator Disk	0.643	0.418	1.117	-0.688	0.445
Incompressible Blade Element	0.571	0.139	1.003	-0.561	0.809
Compressible Blade Element	0.625	0.271	1.140	-0.557	0.555
Overset (Average)	0.601	0.579^{+}	0.009^{+}	-0.556^{+}	0.289^{+}

+ Fuselage forces based on integrated surface pressure

Table 12: ROBIN Timing Comparison

Rotor Model	**Run Time** (hours)	**Number of Processors**	**Number of Iterations**	**Scaled Time** (milliseconds)
No Rotor	1.925	64	1000	0.2653
Uniform Actuator Disk	1.787	64	1000	0.2463^{+}
Linear Actuator Disk	1.768	64	1000	0.2438^{+}
Incompressible Blade Element Actuator Disk	2.071	64	1000	0.2855
Compressible Blade Element Actuator Disk	3.013	64	1000	0.4155
Overset One Revolution	38.91	72	360	$10.23^{\diamond}$
Overset Full Computation	155.7	72	1440	$10.23^{\diamond}$

+ FUN3D compiled with additional optimizations

$\diamond$ Overset computations used precomputed DCI files

CHAPTER VII

CONCLUSIONS & RECOMMENDATIONS

7.1 Conclusions

Three rotor models offering varying degrees of fidelity have been implemented into an unstructured RANS flow solver. A steady-state actuator disk model enables the solver to perform rapid rotor computations, which are useful for quasi-steady performance estimates. An unsteady actuator blade model maintains the simplicity of the actuator disk, but enables time-varying flow effects to be investigated. A variety of blade loading models have also been incorporated for both the actuator disk and actuator blade methods to evaluate the influence of rotor loading on the resulting rotor-fuselage aerodynamics. An overset rotor blade model enables a first-principles-based computation of the rotor aerodynamics, as well as a basis for evaluation of the simplified models. These three models enable rotorcraft designers to select the most appropriate model for the level of physical accuracy desired.

The following conclusions can be drawn from the present study:

- An actuator disk, actuator blade, and overset blade technique has been incorporated into an unstructured solver. Results have been shown to compare well with structured methods and the grid generation times have been substantially reduced.

- An improved source-based actuator disk method has been developed and tested. This improvement permits the same fuselage grid to be utilized for a suite of flight conditions without the need to regenerate the grid. The grid generation process is also simplified by the current method, since the actuator disk does not need to be incorporated into the computational grid.

- Within the source-based actuator disk model it is important to account for the effects of blade flap and drag. A source-based actuator disk model can account for the drag

force in a robust manner, which is not true for the pressure jump approach.

- An unsteady actuator blade model has been developed, which permits the computation of unsteady rotor aerodynamics without the need to model the actual rotor blades. The actuator blade model has an advantage over actual blade modeling, since compressibility can be accounted for indirectly, allowing the incompressible equations to be solved in low-speed conditions. When compared to unsteady actuator disk methods, the actuator blade model holds promise of more accurate results for compound rotor and high solidity rotor problems, as it models the entire blade chord, rather than relying on a lifting-line approach.

- The incompressible flow equations reduce the tip vortex diffusion, enabling the preservation of the rotor wake better than compressible methods. The disparity of the eigenvalues for low Mach number flows is the primary reason for this behavior.

- The incompressible scheme is found to require 2/3 the effort of the compressible scheme per iteration. Unsteady computations increase the required computational effort by an order of magnitude and were observed to take 25 times longer than the steady compressible scheme for a single iteration.

- The uniform and linear actuator disk loading do not provide satisfactory results in forward flight due to the lack of asymmetry in the disk loading. The linear model model can produce reasonable hover predictions, since it accounts for the increased blade tip loads.

- The blade element model obtains good predictions of the time-averaged rotor behavior in regions where the tip vortex propagates away from the disk. Poor correlations may be obtained over the forward portion of the disk in forward flight if there is interaction between the rotor wake and the blades.

7.2 Recommendations

The following recommendations are offered to extend the present work:

- Development of a trim routine is the logical next step in this work. Although prescribed motions worked well for the GIT configuration, they were unsatisfactory in the ROBIN investigation.

- There is a level of detail between the linear disk loading and blade element method that can be further explored. A method that accounts for the asymmetry of forward flight could potentially increase accuracy while retaining the benefit of being a simple model.

- Addition of multiple degree-of-freedom capability would allow for more complex blade motions. This capability would also allow the overset implementation to be used with a wider array of applications such as store separation, which is also important to the rotorcraft community.

- To examine vibratory loads and unsteady aeroelastic phenomena for complete rotorcraft, the present method can be coupled with a comprehensive analysis code to provide elastic rotor evaluations. The UH-60 Airloads Workshop has shown significant improvement in airloads predictions when coupling CFD with a comprehensive code [83].

- Unstructured grid adaptation was not explored in this work, but is certainly an important prospect to improve wake simulations while minimizing computational grid increases. The adjoint-based adaptation in FUN3D could be especially beneficial in capturing the vortex wake structure of the rotor. Feature-based adaptation techniques have also shown improved wake capturing ability, but can substantially increase the grid size after a few levels of adaptation.

- The actuator blade model should be further explored. Since the blades are not directly modeled, the actuator blade method can utilize the incompressible equations, which provides a substantial savings over solving the compressible equations. An improved search algorithm for associating the sources with grid nodes may help to reduce the cost of the computation. The chord-wise loading algorithm, as well as

the introduction of tip corrections, should be further developed to see if improved correlation with experiments can be obtained.

- Improvements to the computation of the grid connectivity for dynamic overset computations is another area for improvement. In particular parallelization of the grid assembly would enable quicker updates and avoid the bottleneck generated when the parallel flow solver waits on the sequential grid assembly program.

REFERENCES

[1] Kunz, D. L., "Comprehensive Rotorcraft Analysis: Past, Present, and Future," in *46th Structures, Structural Dynamics, & Materials Conference*, (Austin, TX), American Institute of Aeronautics and Astronautics, April 2005.

[2] Strawn, R. C., Caradonna, F. X., and Duque, E. P. N., "30 Years of Rotorcraft Computational Fluid Dynamics Research and Development," *Journal of the American Helicopter Society*, vol. 51, no. 1, 2006.

[3] Johnson, W., *Helicopter Theory*. New York: Dover Publications, Inc., 1994.

[4] Prouty, R. W., *Helicopter Performance, Stability, and Control*. Melbourne, FL: Krieger Pub. Co, 2002.

[5] Leishman, J. G., *Principles of Helicopter Aerodynamics*. New York: Cambridge University Press, 2006.

[6] Stepniewski, W. Z. and Keys, C. N., *Rotary-Wing Aerodynamics*. New York: Dover Publications, Inc., 1984.

[7] Wilson, J. C. and Mineck, R. E., "Wind-Tunnel Investigation of Helicopter-Rotor Wake Effects on Three Helicopter Fuselage Models," Tech. Rep. TM X-3185, NASA, 1975.

[8] Wilson, J. C. and Mineck, R. E., "Wind-Tunnel Investigation of Helicopter-Rotor Wake Effects on Three Helicopter Fuselage Models," Tech. Rep. TM X-3185 Supplemental, NASA, 1975.

[9] Freeman, C. E. and Mineck, R. E., "Fuselage Surface Pressure Measurements of a Helicopter Wind-Tunnel Model with a 3.15-Meter Diameter Single Rotor," Tech. Rep. TM-80051, NASA, 1979.

[10] Sheridan, P. F. and Smith, R. P., "Interactional Aerodynamics - A New Challenge to Helicopter Technology," in *Proceedings of the 35th Annual Forum*, (Washington, DC), American Helicopter Society, May 1979.

[11] Brand, A. G., *An Experimental Investigation of the Interaction Between a Model Rotor and Airframe in Forward Flight*. PhD thesis, Georgia Institute of Technology, 1989.

[12] Brand, A. G., Komerath, N. M., and McMahon, H. M., "Wind Tunnel Data from a Rotor Wake/Airframe Interaction Study," Tech. Rep. CERWAT Report No. DAAG29-82-k-0094, School of Aerospace Engineering, Georgia Institute of Technology, July 1986.

[13] Brand, A. G., McMahon, H. M., and Komerath, N. M., "Surface Pressure Measurements on a Body Subject to Vortex Wake Interaction," *American Institute of Aeronautics and Astronautics Journal*, vol. 27, no. 5, 1989.

[14] Brand, A. G., McMahon, H. M., and Komerath, N. M., "Correlations of Rotor Wake / Airframe Interaction Measurements with Flow Visualization Data," *Journal of the American Helicopter Society*, vol. 35, no. 4, 1990.

[15] Brand, A. G., Komerath, N. M., and McMahon, H. M., "Results From Laser Sheer Visualization of a Periodic Rotor Wake," *Journal of Aircraft*, vol. 26, no. 5, 1989.

[16] Liou, S. G., *Velocity Measurements on a Lifting Rotor/Airframe Configuration in Low Speed Forward Flight*. PhD thesis, Georgia Institute of Technology, 1988.

[17] Liou, S. G., Komerath, N. M., and McMahon, H. M., "Velocity Measurements of Airframe Effects on a Rotor in Low Speed Forward Flight," *Journal of Aircraft*, vol. 26, no. 4, 1989.

[18] Liou, S. G., Komerath, N. M., and McMahon, H. M., "Measurement of the Interaction Between a Rotor Tip Vortex and a Cylinder," *American Institute of Aeronautics and Astronautics Journal*, vol. 28, no. 6, 1990.

[19] Elliott, J. W., Althoff, S. L., and Sailey, R. H., "Inflow Measurement Made with a Laser Velocimeter on a Helicopter Model in Forward Flight. Volume I: Rectangular Planform Blades at an Advance Ratio of 0.15," Tech. Rep. TM-100541, NASA, 1988.

[20] Elliott, J. W., Althoff, S. L., and Sailey, R. H., "Inflow Measurement Made with a Laser Velocimeter on a Helicopter Model in Forward Flight. Volume II: Rectangular Planform Blades at an Advance Ratio of 0.23," Tech. Rep. TM-100542, NASA, 1988.

[21] Elliott, J. W., Althoff, S. L., and Sailey, R. H., "Inflow Measurement Made with a Laser Velocimeter on a Helicopter Model in Forward Flight. Volume III: Rectangular Planform Blades at an Advance Ratio of 0.30," Tech. Rep. TM-100543, NASA, 1988.

[22] Hoad, D. R., Althoff, S. L., Elliott, J. W., and Sailey, R. H., "Inflow Measurement Made with a Laser Velocimeter on a Helicopter Model in Forward Flight. Volume 6: Rectangular Planform Blades at an Advance Ratio of 0.35," Tech. Rep. TM-101598, NASA, 1989.

[23] Hoad, D. R., Althoff, S. L., Elliott, J. W., and Sailey, R. H., "Inflow Measurement Made with a Laser Velocimeter on a Helicopter Model in Forward Flight. Volume 7: Rectangular Planform Blades at an Advance Ratio of 0.40," Tech. Rep. TM-101599, NASA, 1989.

[24] Althoff, S. L., Elliott, J. W., Hoad, D. R., and Sailey, R. H., "Inflow Measurement Made with a Laser Velocimeter on a Helicopter Model in Forward Flight. Volume 8: Rectangular Planform Blades at an Advance Ratio of 0.23, 0.50 Chord Above the Tip Path Plane," Tech. Rep. TM-102642, NASA, 1990.

[25] Althoff, S. L., Elliott, J. W., Hoad, D. R., and Sailey, R. H., "Inflow Measurement Made with a Laser Velocimeter on a Helicopter Model in Forward Flight. Volume 9: Rectangular Planform Blades at an Advance Ratio of 0.23, 0.75 Chord Above the Tip Path Plane," Tech. Rep. TM-102643, NASA, 1990.

[26] Althoff, S. L., Elliott, J. W., Hoad, D. R., and Sailey, R. H., "Inflow Measurement Made with a Laser Velocimeter on a Helicopter Model in Forward Flight. Volume 10:

Rectangular Planform Blades at an Advance Ratio of 0.30, 0.50 Chord Above the Tip Path Plane," Tech. Rep. TM-102644, NASA, 1990.

[27] Althoff, S. L., Elliott, J. W., Hoad, D. R., and Sailey, R. H., "Inflow Measurement Made with a Laser Velocimeter on a Helicopter Model in Forward Flight. Volume 11: Rectangular Planform Blades at an Advance Ratio of 0.30, 0.75 Chord Above the Tip Path Plane," Tech. Rep. TM-102645, NASA, 1990.

[28] Althoff, S. L., Elliott, J. W., and Sailey, R. H., "Inflow Measurement Made with a Laser Velocimeter on a Helicopter Model in Forward Flight. Volume IV: Tapered Planform Blades at an Advance Ratio of 0.15," Tech. Rep. TM-100544, NASA, 1988.

[29] Althoff, S. L., Elliott, J. W., and Sailey, R. H., "Inflow Measurement Made with a Laser Velocimeter on a Helicopter Model in Forward Flight. Volume V: Tapered Planform Blades at an Advance Ratio of 0.23," Tech. Rep. TM-100545, NASA, 1988.

[30] Ghee, T. A. and Elliott, J. W., "The Wake of a Small-Scale Rotor in Forward Flight Using Flow Visualization," *Journal of the American Helicopter Society*, vol. 40, no. 3, 1995.

[31] Mineck, R. E. and Althoff-Gorton, S. L., "Steady and Periodic Pressure Measurements on a Generic Helicopter Fuselage Model in the Presence of a Rotor," Tech. Rep. TM-210286, NASA, 2000.

[32] Bi, N. P. and Leishman, J. G., "Experimental Study of Rotor/Body Aerodynamic Interactions," *Journal of Aircraft*, vol. 27, no. 9, 1990.

[33] Bi, N. P. and Leishman, J. G., "Analysis of Unsteady Pressures Induced on a Body by a Rotor," *Journal of Aircraft*, vol. 28, no. 11, 1991.

[34] Bi, N. P., Leishman, J. G., and Crouse, G. L., "Investigation of Rotor Tip Vortex Interactions with a Body," *Journal of Aircraft*, vol. 30, no. 6, 1993.

[35] Bettschart, N. and Gasser, D., "Analysis of Helicopter Rotor-Fuselage Interaction," in *20th European Rotorcraft Forum*, (Amsterdam, Netherlands), October 1997.

[36] Berry, J. and Bettschart, N., "Rotor-Fuselage Interaction: Analysis and Validation with Experiment," in *53rd American Helicopter Society Forum*, (Virginia Bech, VA), April-May 1997.

[37] LePape, A., Gatard, J., and Monnier, J., "Experimental Investigations of Rotor-Fuselage Aerodynamic Interactions Using a Helicopter Powered Model," in *30th European Rotorcraft Forum*, (Marseilles, France), September 2004.

[38] Landgrebe, A. J., Moffitt, R. C., and Clark, D. R., "Aerodynamic Technology for Advanced Rotorcraft: Parts I and II," *Journal of the American Helicopter Society*, vol. 22, no. 2-3, 1977.

[39] Clark, D. R. and Maskew, B., "Study for Prediction of Rotor/Wake/Fuselage Interference Part I: Technical Report," Tech. Rep. CR-177340, NASA, 1985.

[40] Clark, D. R. and Maskew, B., "Study for Prediction of Rotor/Wake/Fuselage Interference Part II: Program User's Guide," Tech. Rep. CR-177340, NASA, 1985.

[41] Lorber, P. F. and Egolf, T. A., "An Unsteady Helicopter Rotor-Fuselage Aerodynamic Interaction Analysis," *Journal of the American Helicopter Society*, vol. 35, no. 3, pp. 32–42, 1990.

[42] Mavris, D. N., *An Analytical Method for the Prediction of Unsteady Rotor / Airframe Interactions in Forward Flight*. Revised edition, Georgia Institute of Technology, 1991.

[43] Mavris, D. N., Komerath, N. M., and McMahon, H. M., "Prediction of Aerodynamic Rotor-Airframe Interactions in Forward Flight," *Journal of the American Helicopter Society*, vol. 34, no. 4, pp. 37–46, 1989.

[44] Rajagopalan, R. G. and Fanucci, J. B., "Finite Difference Model for Vertical Axis Wind Turbines," *Journal of Propulsion and Power*, vol. 1, no. 6, pp. 432–436, 1985.

[45] Rajagopalan, R. G. and Lim, C. K., "Laminar Flow Analysis of a Rotor in Hover," *Journal of the American Helicopter Society*, vol. 36, no. 1, pp. 12–23, 1991.

[46] Zori, L. A. J., Mathur, S. R., and Rajagopalan, R. G., "Three-Dimensional Calculations of Rotor-Airframe Interaction in Forward Flight," in *Proceedings of the 48th Annual Forum*, (Washington, DC), American Helicopter Society, June 1992.

[47] Rajagopalan, R. G., "A Procedure for Rotor Performance, Flowfield and Interference: A Perspective," in *38th Aerospace Sciences Meeting*, (Reno, NV), American Institute of Aeronautics and Astronautics, January 2000.

[48] Fejtek, I. and Roberts, L., "Navier-Stokes Computation of a Wing/Rotor Interaction for a Tilt Rotor in Hover," *American Institute of Aeronautics and Astronautics Journal*, vol. 30, no. 11, pp. 2595–2603, 1992.

[49] Chaffin, M. S. and Berry, J. D., "Navier-Stokes Simulation of a Rotor Using a Distributed Pressure Disk Method," in *Proceedings of the 51st Annual Forum*, (Forth Worth, TX), American Helicopter Society, May 1995.

[50] Chaffin, M. S. and Berry, J. D., "Helicopter Fuselage Aerodynamics Under a Rotor by Navier-Stokes Simulation," *Journal of American Helicopter Society*, vol. 42, no. 3, pp. 235–242, 1997.

[51] Bettschart, N., "Rotor Fuselage Interaction: Euler and Navier-Stokes Computations with an Actuator Disk," in *Proceedings of the 55th Annual Forum*, (Montreal, Canada), American Helicopter Society, May 1999.

[52] Le Chuiton, F., "Quasi-Steady Simulation Of A Complete EC-145 Helicopter: Fuselage + Main / Tail Actuator Discs + Engines," in *31st European Rotorcraft Forum*, (Florence, Italy), September 2005.

[53] Boyd, D. D., *Rotor/Fuselage Unsteady Interactional Aerodynamics: A New Computational Model*. PhD thesis, Virginia Polytechnic Institute and State University, 1999.

[54] Boyd, D. D., Barnwell, R. W., and Althoff-Gorton, S. L., "A Computational Model for Rotor-Fuselage Interactional Aerodynamics," in *38th Aerospace Sciences Meeting*, (Reno, NV), American Institute of Aeronautics and Astronautics, January 2000.

[55] Tadghighi, H., "Simulation of Rotor-Body Interactional Aerodynamics: An Unsteady Rotor Source Distributed Disk Model," in *Proceedings of the 57th Annual Forum*, (Washington, DC), American Helicopter Society, May 2001.

[56] Hariharan, N. S., *High Order Simulation of Unsteady Compressible Flows over Interacting Bodies with Overset Grids*. PhD thesis, Georgia Institute of Technology, 1995.

[57] Noack, R., "DiRTlib: A Library to Add Overset Capability to Flow Solvers," in *6th Symposium on Overset Grids and Solution Technology*, (Fort Walton Beach, FL), October 2002.

[58] Noack, R., "Resolution Appropriate Overset Grid Assembly for Structured and Unstructured Grids," in *6th Symposium on Overset Grids and Solution Technology*, (Fort Walton Beach, FL), October 2002.

[59] Benoit, C., Jeanfaivre, G., and Canonne, E., "Synthesis Of ONERA Chimera Method Development In The Frame Of CHANCE Program," in *31st European Rotorcraft Forum*, (Florence, Italy), September 2005.

[60] Renaud, T., Le Pape, A., and Benoit, C., "Unsteady Euler And Navier-Stokes Computations Of A Complete Helicopter," in *31st European Rotorcraft Forum*, (Florence, Italy), September 2005.

[61] Schwarz, T., "The Overlapping Grid Technique For Time Accurate Simulation Of Rotorcraft Flows," in *31st European Rotorcraft Forum*, (Florence, Italy), September 2005.

[62] Khier, W., Schwarz, T., and Raddatz, J., "Time-Accurate Simulation Of The Flow Around The Complete BO105 Wind Tunnel Model," in *31st European Rotorcraft Forum*, (Florence, Italy), September 2005.

[63] Strawn, R. C. and Djomehri, M. J., "Computational Modeling of Hovering Rotor Wake Aerodynamics," in *Proceedings of the 57th Annual Forum*, (Washington, DC), American Helicopter Society, May 2001.

[64] Potsdam, M. A. and Strawn, R. C., "CFD Simulations of Tiltrotor Configurations in Hover," in *Proceedings of the 58th Annual Forum*, (Montreal, Canada), American Helicopter Society, June 2002.

[65] Potsdam, M., "Dynamic Rotorcraft Applications Using Overset Grids," in *31st European Rotorcraft Forum*, (Florence, Italy), September 2005.

[66] Strawn, R. C. and Barth, T. J., "A Finite-Volume Euler Solver for Computing Rotary-Wing Aerodynamics on Unstructured Grids," in *Proceedings of the 48th Annual Forum*, (Washington, DC), American Helicopter Society, June 1992.

[67] Kang, H. J. and Kwon, O. J., "Effect of Wake Adaptation on Rotor Hover Simulations Using Unstructured Meshes," in *38th Aerospace Sciences Meeting*, (Reno, NV), American Institute of Aeronautics and Astronautics, January 2000.

[68] Bottasso, C. L. and Shephard, M. S., "Parallel Adaptive Finite Element Euler Flow Solver for Rotary Wing Aerodynamics," *American Institute of Aeronautics and Astronautics Journal*, vol. 35, no. 6, pp. 937–944, 1997.

[69] Pan, D., Chao, M. J., and Chien, S. K., "Euler Computations of Rotor Flows on Unstructured Rotating Meshes," *Journal of Aircraft*, vol. 38, no. 4, pp. 672–679, 2001.

[70] Kang, H. J. and Kwon, O. J., "Viscous Flow Simulation of a Lifting Rotor in Hover Using Unstructured Adaptive Meshes," in *Proceedings of the 57th Annual Forum*, (Washington, DC), American Helicopter Society, May 2001.

[71] Lee, J. K. and Kwon, O. J., "Predicting Aerodynamic Rotor-Fuselage Interactions by Using Unstructured Meshes," *Transactions of the Japan Society for Aeronautical and Space Sciences*, vol. 44, no. 146, pp. 208–216, 2002.

[72] O'Brien, Jr, D. M. and Smith, M. J., "Improvements in the Computational Modeling of Rotor / Fuselage Interactions Using Unstructured Grids," in *Proceedings of the 61st Annual Forum*, (Grapevine, TX), American Helicopter Society, June 2005.

[73] Schweikhard, R. and Le Chuiton, F., "Actuator Disc For Helicopter Rotors In The Unstructured Flow Solver TAU," in *31st European Rotorcraft Forum*, (Florence, Italy), September 2005.

[74] Heise, R., Meyer, C. J., and von Backstrom, T. W., "Development Of A Method For CFD Evaluation Of Helicopter Fuselages," in *31st European Rotorcraft Forum*, (Florence, Italy), September 2005.

[75] M., P. Y. and Kwon, O. J., "Simulation of Unsteady Rotor Flow Fields Using Unstructured Sliding Meshes," in *Proceedings of the 58th Annual Forum*, (Montreal, Canada), American Helicopter Society, June 2002.

[76] Park, Y. M., Nam, H. J., and Kwon, O. J., "Simulation of Unsteady Rotor-Fuselage Interactions Using Unstructured Adaptive Meshes," in *Proceedings of the 59th Annual Forum*, (Phoenix, AZ), American Helicopter Society, May 2003.

[77] O'Brien, Jr, D. M. and Smith, M. J., "Understanding the Physical Implications of Approximate Rotor Methods Using an Unstructured CFD Method," in *31st European Rotorcraft Forum*, (Florence, Italy), September 2005.

[78] Ruffin, S. M., O'Brien, Jr, D. M., Smith, M. J., Hariharan, N. S., Lee, J. D., and Sankar, L., "Comparison of Rotor-Airframe Interaction Utilizing Overset and Unstructured Grid Techniques," in *42nd Aerospace Sciences Meeting*, (Reno, NV), American Institute of Aeronautics and Astronautics, January 2004.

[79] Moulton, M. A., Wenren, Y., and Caradonna, F. X., "Free-Wake Hover Flow Prediction with a Hybrid Potential / Navier-Stokes Solver," in *Proceedings of the 55th Annual Forum*, (Montreal, Canada), American Helicopter Society, May 1999.

[80] Wenren, Y., Steinhoff, J., and Caradonna, F. X., "Application of Vorticity Confinement to Rotorcraft Flows," in *31st European Rotorcraft Forum*, (Florence, Italy), September 2005.

[81] Brown, R. E., "Rotor Wake Modeling for Flight Dynamic Simulation of Helicopters," *AIAA Journal*, vol. 38, no. 1, 2000.

[82] Brown, R. E. and Line, A. J., "Efficient High-Resolution Wake Modeling Using the Vorticity Transport Equation," *AIAA Journal*, vol. 43, no. 7, 2005.

[83] Datta, A., Nixon, M., and Chopra, I., "Review of Rotor Loads Prediction With the Emergence of Rotorcraft CFD," in *31st European Rotorcraft Forum*, (Florence, Italy), September 2005.

[84] Potsdam, M., Yeo, H., and Johnson, W., "Rotor Airloads Prediction Using Loose Aerodynamic/Structural Coupling," in *Proceedings of the 60th Annual Forum*, (Baltimore, MD), American Helicopter Society, June 2004.

[85] Sitaraman, J., Datta, A., Baeder, J., and Chopra, I., "Coupled CFD/CSD Prediction Of Rotor Aerodynamic And Structural Dynamic Loads For Three Critical Flight Conditions," in *31st European Rotorcraft Forum*, (Florence, Italy), September 2005.

[86] Pahlke, K., Costes, M., D'Alascio, A., Castellin, C., and Altmikus, A., "Overview Of Results Obtained During The 6-Year French-German CHANCE Project," in *31st European Rotorcraft Forum*, (Florence, Italy), September 2005.

[87] Beaumier, P., Costes, M., Rodriguez, B., Poinot, M., and Cantaloube, B., "Weak And Strong Coupling Between The elsA CFD Solver And The HOST Helicopter Comprehensive Analysis," in *31st European Rotorcraft Forum*, (Florence, Italy), September 2005.

[88] Tannehill, J., Anderson, D., and Pletcher, R., *Computational Fluid Mechanics and Heat Transfer*. Philadelphia, PA: Taylor & Francis, 2nd ed., 1997.

[89] Bonhaus, D. L., "An Upwind Multigrid Method for Solving Viscous Flows on Unstructured Triangular Meshes," Master's thesis, Georgia Washington University, 1993.

[90] Anderson, W. K. and Bonhaus, D. L., "An Implicit Upwind Algorithm for Computing Turbulent Flows on Unstructured Grids," *Computers & Fluids*, vol. 23, no. 1, pp. 1–21, 1994.

[91] Anderson, W. K., Rausch, R. D., and Bonhaus, D. L., "Implicit/Multigrid Algorithms for Incompressible Turbulent Flows on Unstructured Grids," *Journal of Computational Physics*, vol. 128, no. 2, pp. 391–408, 1996.

[92] "http://fun3d.larc.nasa.gov." Website, Last Accessed, December 2005.

[93] Kleb, W. L., Nielsen, E. J., Gnoffo, P. A., Park, M. A., and Wood, W. A., "Collaborative Software Development in Support of Fast Adaptive AeroSpace Tools (FAAST)," in *16th Computational Fluid Dynamics Conference*, (Orlando, FL), American Institute of Aeronautics and Astronautics, June 2003.

[94] Chorin, A. J., "A Numerical Method for Solving Incompressible Viscous Flow Problems," *Journal of Computational Physics*, vol. 2, no. 1, pp. 12–26, 1967.

[95] Rossow, C. C., "A Flux Splitting Scheme for Compressible and Incompressible Flows," in *14th Computational Fluid Dynamics Meeting*, (Norfolk, VA), American Institute of Aeronautics and Astronautics, June 1999.

[96] Choi, Y. H. and Merkle, C. L., "The Application of Preconditioning to Viscous Flows," *Journal of Computational Physics*, vol. 105, pp. 207–233, 1993.

[97] Spalart, P. R. and Allmaras, S. R., "A One-Equation Turbulence Model for Aerodynamic Flows," *AIAA Paper*, no. 92-0439, 1991.

[98] Menter, F. R., "Two-Equation Eddy-Viscosity Turbulence Models for Engineering Applications," *American Institute of Aeronautics and Astronautics Journal*, vol. 32, no. 8, pp. 1598–1605, 1994.

[99] Roe, P. L., "Approximate Riemann Solvers, Parameter Vectors, and Difference Schemes," *Journal of Computational Physics*, vol. 43, pp. 357–371, 1981.

[100] Biedron, R., Vatsa, V., and Atkins, H., "Simulation of Unsteady Flows Using an Unstructured Navier-Stokes Solver on Moving and Stationary Grids," in *23th Applied Aerodynamics Conference*, (Toronto, Ontario, Canada), American Institute of Aeronautics and Astronautics, June 2005.

[101] Nielsen, E., Lu, J., Park, M., and Darmofal, D., "An Implicit, Exact Dual Adjoint Solution Method for Turbulent Flows on Unstructured Grids," *Computers and Fluids*, vol. 33, no. 9, pp. 1131–1155, 2004.

[102] Pirzadeh, S., "Unstructured Viscous Grid Generation by Advancing-Layers Method," *American Institute of Aeronautics and Astronautics Journal*, vol. 32, no. 8, pp. 1735–1737, 1994.

[103] Pirzadeh, S., "Three-Dimensional Unstructured Viscous Grids by the Advancing Front Method," *American Institute of Aeronautics and Astronautics Journal*, vol. 34, no. 1, pp. 43–49, 1996.

[104] "http://geolab.larc.nasa.gov/GridTool/." Website, Last Accessed, December 2005.

[105] Uknown, *Fieldview Users Manual, Version 10.0*. Intelligent Light, 2005.

[106] "http://www.ilight.com." Website, Last Accessed, December 2005.

[107] Uknown, *Tecplot Users Manual, Version 10.0*. Tecplot, Inc., 2005.

[108] "http://www.tecplot.com." Website, Last Accessed, December 2005.

[109] Jeong, J. and Hussain, F., "On the Identification of a Vortex," *Journal of Fluid Mechanics*, vol. 285, pp. 69–94, 1985.

[110] Le Chuiton, F., "Actuator Disc Modeling for Helicopter Rotors," *Aerospace Science and Technology*, vol. 8, no. 4, pp. 285–297, 2004.

[111] Renaud, T., Potsdam, M., O'Brien, Jr, D. M., and Smith, M. J., "Evaluation of Isolated Fuselage and Rotor-Fuselage Interaction Using CFD," in *Proceedings of the 60th Annual Forum*, (Baltimore, MD), American Helicopter Society, June 2004.

[112] Pandya, M. J., Frink, N. T., and Noack, R. W., "Progress Toward Overset-Grid Moving Body Capability for USM3D Unstructured Flow Solver," in *17th Computational Fluid Dynamics Conference*, (Toronto, Ontario), American Institute of Aeronautics and Astronautics, June 2005.

[113] "Equations, Tables, and Charts for Compressible Flow." NACA Report 1135, Reproduced by AMTEC Engineering Inc., Bellevue, WA.

[114] "http://www.ae.gatech.edu/labs/windtunl/expaero/jjht.html." Website, Last Accessed, February 2006.

[115] "http://windtunnels.larc.nasa.gov/facilities/aerodynamics/14x22.htm." Website, Last Accessed, February 2006.

[116] Phelps, III, A. E. and Berry, J. D., "Description of the U.S. Army Small-Scale 2-Meter Rotor Test System," Tech. Rep. TM-87762, NASA, 1987.

[117] "http://www.onera.fr/gmt-en/wind-tunnels/f1.html." Website, Last Accessed, February 2006.

[118] Benoit, B., Dequin, A. M., Kampa, K., Grunhagen, W., Basset, P. M., and Gimonet, B., "HOST: A General Helicopter Simulation Tool For Germany and France," in *Proceedings of the 56th Annual Forum*, (Virginia Beach, VA), American Helicopter Society, May 2000.

VITA

David M. O'Brien, Jr. was born in Voorhees, New Jersey on March 30, 1979. He is the son of David and Ellyn O'Brien and has a younger brother, Charles. His father later remarried, giving him a stepmother, Louise, an older brother, Bob, and younger sister, Shauna. He is currently engaged to be married to the lovely Jill Brew on May 27, 2006.

As a student at Cherry Hill East High School he developed an interest in mathematics and physics, which led him to pursue a career in engineering at Virginia Polytechnic Institute and State University. Pursuing an interest in the aircraft, he joined the Aerospace Engineering department. During the summer of his junior year he received the National Undergraduate Fusion Fellowship, which allowed him to work on a summer research project at General Atomics in San Diego, CA. This experience encouraged him to go to graduate school to obtain an advanced degree.

In May of 2001 he graduated Magna Cum Laude with a Bachelor's Degree in Aerospace Engineering. The following fall he began his graduate work at Georgia Institute of Technology, where he was awarded a Georgia Tech Institute Fellowship to pursue a Ph.D. degree in the School of Aerospace Engineering. As a graduate student, he worked in the Georgia Tech Center of Excellence for Rotorcraft Technology under the guidance of Dr. Marilyn Smith. His research into rotor / airframe interactions gave him the opportunity to be a part of an international collaboration with ONERA and the US Army Aeroflightdynamics Directorate. He earned his Master's of Science in Aerospace Engineering in December 2003 and was awarded a Ph.D. degree in Aerospace Engineering in May 2006.

He is a member of the American Institute of Aeronautics and Astronautics and the American Helicopter Society. As a student he was also inducted into the Golden Key National Honor Society and the National Aerospace Engineering Honor Society, Sigma Gamma Tau.